

MOBILE MAPPING BENEATH FOREST CANOPY: SYSTEM DEVELOPMENT AND
APPLICATION

By

ADAM R. BENJAMIN

A THESIS PRESENTED TO THE GRADUATE SCHOOL
OF THE UNIVERSITY OF FLORIDA IN PARTIAL FULFILLMENT
OF THE REQUIREMENTS FOR THE DEGREE OF
MASTER OF SCIENCE

UNIVERSITY OF FLORIDA

2011

© 2011 Adam R. Benjamin

To Mom, Dad, Erica, & Kai

ACKNOWLEDGMENTS

I cannot thank Dr. Ahmed Mohamed enough for extending me the opportunity to study with him at the University of Florida. His passion for geomatics and navigation is evident in the amount of time and effort he has put in helping me throughout this project and my course of study. Thanks to Dr. Bon Dewitt for introducing me to the field of photogrammetry, a focal topic of this thesis, and being a mentor throughout my graduate education. I thank Dr. Valeriy Yarmola for his support of my thesis project and collaboration on the G3 research projects.

Recognition is necessary for all of the NaGeM research team members that have helped me with this thesis project. I thank Ben Wilkinson for his help in programming complex algorithms and being a sounding board for all my ideas that are "never going to work." Thanks to Kuei-tsung (Philips) Shih for his tireless effort in making sure my NaGeM research project was successful through software development and electronics fabrication. Thanks to Apostolos (Tolee) Mamatras for collaborating with me on this vision-aiding concept including hardware fabrication and also partaking in many enlightening navigation-related discussions. Thanks to Nicholas DiGruttolo, Zoltan Szantoi, and Sowmya Selvarajan for your guidance and support throughout our graduate experience.

Thank you to Dan Schultz and Gary St. John at Austin Cary Memorial Forest. Between providing access to the ATV and assistance in mounting the GatorMMS components to the ATV, your help is very much appreciated. Also, thanks to Dr. Amr Abd-Elrahman for providing access to the PhotoModeler® camera calibration software.

Additionally, I thank the UF College of Agriculture and Life Sciences (CALs), the UF School of Forest Resources and Conservation (SFRC), and RIEGL USA

<http://www.rieglusa.com/> for funding for my graduate assistantship.

All of what I have done would not have been possible without my family. I thank my parents, Muriel and Bobby, and my brother, Zack, for their constant encouragement and support. Lastly, I thank my "dp", Erica, for keeping our home in order and providing Kai with so much care that I could accomplish as much as I have over the past two years.

TABLE OF CONTENTS

	<u>page</u>
ACKNOWLEDGMENTS.....	4
LIST OF TABLES.....	9
LIST OF FIGURES.....	10
LIST OF ABBREVIATIONS.....	14
ABSTRACT	18
CHAPTER	
1 INTRODUCTION	20
1.1 Problem Background	20
1.2 Motivation	22
1.3 Objectives	22
1.4 Research Questions	22
1.5 Hypothesis.....	22
1.6 Report Structure	23
2 LITERATURE REVIEW	24
2.1 Mobile Mapping Systems.....	24
2.2 Vision-Aiding.....	27
2.3 Forest Mapping.....	30
2.3.1 GPS Positioning in the Forest	31
2.3.2 Forest Canopy Density Affecting GPS Positioning	32
2.3.3 Mobile Mapping Systems Under Forest Canopy	35
3 GATORMMS COMPONENTS	39
3.1 GatorMMS – The Mobile Mapping System for the Forest.....	39
3.2 Georeferencing System	40
3.2.1 GPS.....	40
3.2.2 GPS-Aided Inertial Navigation Systems	41
3.3 Imaging System	43
3.3.1 Camera.....	44
3.3.2 Lenses.....	45
3.4 MMS Coordinate Systems	46
4 GEOFERENCING SYSTEM TESTING.....	53
4.1 Study Site – Austin Cary Memorial Forest	53

4.2	Data Acquisition	53
4.3	GPS/GNSS Processing in the Forest.....	55
4.4	INS-Free Navigation	56
4.5	GPS-Aided INS-Navigation.....	58
4.5.1	Loosely Coupled GPS/INS Integration	59
4.5.2	Loosely Coupled Integration and Tightly Coupled Integration Comparison.....	60
4.5.3	GPS-Aided Inertial Navigation Trajectory – Absolute Accuracy Analysis.....	61
4.6	Georeferencing System Testing Lessons Learned	63
5	IMAGING SYSTEM TESTING	79
5.1	Self-Calibrating Bundle Adjustment	79
5.2	Camera Calibration – Interior Orientation	80
5.2.1	Methods.....	81
5.2.2	Results	82
5.3	Boresight-Lever Arm Calibration.....	83
5.3.1	Reed Lab Roof BSLA Calibration Field	84
5.3.2	BSLA Calibration Methods	85
5.3.3	BSLA Calibration Results	86
5.4	Imaging System Testing Lessons Learned	88
6	GATORMMS: VERTICAL ORIENTATION FOR CANOPY DENISTY ANALYSIS ..	98
6.1	GatorMMSv2.0 Applications – Canopy Density Analysis	98
6.2	Methods	98
6.3	Preliminary Image Processing Results	100
6.4	GatorMMS Testing Results.....	101
6.5	GatorMMS Canopy Density Analysis Lessons Learned.....	104
7	GATORMMS: HORIZONTAL ORIENTATION FOR VISION-AIDING	114
7.1	GatorMMSv2.0 Application: Vision-Aiding	114
7.2	ACMF VA Methods	115
7.2.1	Orientation.....	115
7.2.2	ACMF VA Test Site	115
7.2.3	ACMF VA Procedure.....	117
7.3	GatorMMS VA Results.....	117
7.3.1	ACMF VA Non-ZUPT Trials.....	118
7.3.2	ACMF VA ZUPT Trial	120
7.3.3	ACMF VA Trials: Low-Accuracy H3 IMU	121
7.4	GatorMMS VA Lessons Learned	122
8	SEQUENTIAL VISION-AIDING	135
8.1	Theoretical Framework	135
8.1.1	Kalman Filtering	135

8.1.2 Coplanarity Condition	136
8.2 Methods	138
8.2.1 Dynamics Model	138
8.2.2 Observation Model	139
8.2.3 Optimal Smoothing	139
8.3 Experimental Results	141
8.3.1 Simulation Model	141
8.3.2 UAV Flight Data – Archer Field	145
8.4 Summary & Conclusion	147
9 CONCLUSION	155
9.1 Summary & Conclusions	155
9.2 Recommendations	157
APPENDIX	
A OTSU'S IMAGE THRESHOLDING METHOD	159
B KALMAN FILTER DETAILS	161
C COPLANARITY CONDITION DETAILS	166
C.1 Non-linear Coplanarity Condition	166
C.2 Linearization of the Coplanarity Condition	168
LIST OF REFERENCES	174
BIOGRAPHICAL SKETCH	180

LIST OF TABLES

<u>Table</u>	<u>page</u>
3-1 GPS receiver classification.....	48
3-2 Inertial navigation gyroscope classification.....	48
4-1 Zero velocity updates and coordinate updates for inertial navigation processing.....	64
4-2 Tightly coupled & loosely coupled GPS-aided inertial navigation solution comparison.....	64
4-3 Absolute accuracy investigation of loosely coupled integration.....	65
4-4 Absolute accuracy investigation of tightly coupled integration.....	65
5-1 Differences in camera calibration software programs.....	89
5-2 IOP camera calibration results from PhotoModeler® 6.....	89
5-3 IOP camera calibration results from PhotoModeler® 6 converted to pixels from mm.	90
5-4 IOP camera calibration verification results.....	91
5-5 RLA BSLA calibration field coordinates.....	92
5-6 GatorMMSv2.0 lever arm calibration results.	93
5-7 GatorMMSv2.0 boresight angle calibration results.	93
5-8 GatorMMSv2.0 final BSLA calibration results.....	94
6-1 Hypothesis testing of CDI correlation for statistical significance of relationships.....	106
7-1 VA test area ground control point coordinates in UTM 17N WGS84.....	125
7-2 VA test area target coordinates in UTM 17N WGS84.....	125
7-3 Hypothesis testing of population variances for VA trial 1.....	126
7-4 Hypothesis testing of population variances for VA trial 2.....	126
7-5 Hypothesis testing of population variances for VA trial 3.....	126

LIST OF FIGURES

<u>Figure</u>	<u>page</u>
2-1	Characterization of forest canopy: canopy density versus canopy cover 38
3-1	GatorMMS platform configurations 48
3-2	Indirect georeferencing - Collinearity condition for an aerial stereo model 49
3-3	Loosely coupled GPS/INS integration flow chart 49
3-4	Tightly coupled GPS/INS integration flow chart 50
3-5	Georeferencing system components for GatorMMSv2.0 50
3-6	Imaging system lenses for GatorMMSv2.0 51
3-7	Lens geometry comparison: wide angle vs. fisheye 51
3-8	Physical relationship between GatorMMS sensors including the IMU, the GPS ARP, and the D200 camera 52
4-1	Vicinity map of Austin Cary Memorial Forest 66
4-2	Static GPS observation of ACMF ground control points 66
4-3	GatorMMSv1.0 georeferencing system test tracks in Austin Cary Memorial Forest 67
4-4	GPS satellite status 67
4-5	GPS baseline status – KAR processing 68
4-6	GPS solution plot – KAR processing 68
4-7	GPS solution - ARTK processing 69
4-8	GPS baseline status - ARTK processing 69
4-9	IMU-only navigation trajectory 70
4-10	INS-free navigation - velocity accuracy plot 70
4-11	INS-free navigation - position accuracy plot 71
4-12	INS-free navigation – ZUPTs and CUPTS trajectory 71
4-13	INS-free navigation – ZUPTs and CUPTS – velocity accuracy 72

4-14	INS-free navigation – ZUPTs and CUPTS –positional accuracy	72
4-15	GPS-aided INS navigation – forward-only solution.....	73
4-16	GPS-aided INS navigation – combined filtered solution	73
4-17	GPS-aided INS navigation – forward solution – positional accuracy	74
4-18	GPS-aided INS navigation – combined filtered solution – positional accuracy ...	74
4-19	GPS-aided INS navigation – forward solution – velocity accuracy	75
4-20	GPS-aided INS navigation – combined filtered solution – velocity accuracy	75
4-21	GPS-aided INS navigation – loosely coupled combined and smoothed navigation trajectory	76
4-22	GPS-aided INS navigation – tightly coupled combined and smoothed navigation trajectory	76
4-23	GPS-aided INS navigation – loosely coupled combined and smoothed positional accuracy	77
4-24	GPS-aided INS navigation – tightly coupled combined and smoothed positional accuracy	77
4-25	Tightly coupled & loosely coupled horizontal GPS-aided inertial navigation trajectory comparison	78
5-1	PhotoModeler® camera calibration grid	95
5-2	Radial lens distortion curve.....	95
5-3	Vicinity map of Reed Lab BSLA calibration field.....	96
5-4	Roof view of RLA BSLA calibration field GCPs	96
5-5	GatorMMSv2.0 camera & IMU coordinate frames	97
5-6	Estimated angular orientation precision from BSLA calibration	97
6-1	Fisheye field of view comparison.....	106
6-2	Image thresholding implementation example for grayscale images	107
6-3	Image thresholding implementation example for blue channel only grayscale images.....	107
6-4	Map of ACMF CDI analysis test tracks	108

6-5	Typical image from ACMF CDI analysis on January 27, 2011.....	108
6-6	Plot of CDI results from ACMF test track 2.....	109
6-7	Typical image from ACMF CDI analysis on March 3, 2011	109
6-8	Plot of CDI results from ACMF test track 1	110
6-9	Plot of CDI results relative to tightly coupled position solution from ACMF test track 1.....	111
6-10	Plot of CDI results relative to GNSS-only position solution from ACMF test track 1.....	112
6-11	Plot of CDI results with tightly coupled positional solution precision from ACMF test track 1	113
6-12	Plot of relationship between horizontal precision and time elapsed from static observation.....	113
7-1	ACMF VA test track.....	127
7-2	ACMF VA field setup.....	127
7-3	ACMF VA test area.....	128
7-4	Typical image of ACMF VA test area.....	128
7-5	Estimated orientation angle precision for trial 1	129
7-6	Comparison of pre-SCBA & post-SCBA orientation angle precision for trial 1 .	129
7-7	Estimated position precision for ACMF VA trial 1.	130
7-8	Comparison of pre-SCBA & post-SCBA position precision for ACMF VA trial 1	130
7-9	Comparison of pre-SCBA & post-SCBA orientation angle precision for trial 2 .	131
7-10	Comparison of pre-SCBA & post-SCBA position precision for ACMF VA trial 2	131
7-11	Estimated orientation angle precision for ACMF VA trial 3.....	132
7-12	Estimated position precision for ACMF VA trial 3.	132
7-13	Comparison of pre-SCBA & post-SCBA orientation precision for ACMF VA trial 3.....	133

7-14	Comparison of pre-SCBA & post-SCBA position precision for ACMF VA trial 3.	133
7-15	Low-accuracy H3 IMU inertial trajectory from ACMF VA trial 1	134
7-16	Low-accuracy H3 IMU inertial trajectory from ACMF VA trial 3	134
8-1	Geometry for the coplanarity condition	149
8-2	Improved orientation precision due to improved position precision with forward Kalman filtering	149
8-3	Improved orientation precision due to improved position precision with backward optimal smoothing	150
8-4	Orientation accuracy of backward optimal smoothing over entire image sequence	151
8-5	RMSE for different position precisions with forward Kalman filtering and backward optimal smoothing	151
8-6	The effect of the number of tie points on average angular orientation precision with forward Kalman filtering and backward optimal smoothing.	152
8-7	The effect of the number of tie points on average angular orientation accuracy with forward Kalman filtering and backward optimal smoothing.	152
8-8	UAV aerial image collected over Archer Field	153
8-9	Detail of improved orientation precision due to forward Kalman filtering and backward optimal smoothing	153
8-10	Orientation accuracy of backward optimal smoothing over entire image sequence	154
8-11	RMSE for different position precisions with forward Kalman filtering and backward optimal smoothing	154
B-1	Kalman filter operation block diagram	165

LIST OF ABBREVIATIONS

σ	Standard Deviation
2D	Two Dimensional
ACMF	Austin Cary Memorial Forest
ALSM	Airborne Laser Swath Mapping
ANOVA	Analysis of Variance
AR	Ambiguity Resolution
ARP	Antenna Reference Point
ARTK	Advance Real-Time Kinematic
AT	Aerotriangulation
ATV	All Terrain Vehicle
BA	Bundle Adjustment
BS	Backsight
BSLA	Boresight Lever Arm
CCD	Charge-Coupled Device
CF	Coordinate Frame
cm	Centimeter
CDI	Canopy Density Index
CORS	Continuously Operating Reference Station
COTS	Consumer Off-The-Shelf
CUPT	Coordinate Update
D	Delta (difference) (i.e. DE – Delta East)
DBH	Diameter at Breast Height
DG	Direct Georeferencing
DOP	Dilution of Precision

DSLR	Digital Single Lens Reflex
E	East
EKF	Extended Kalman Filter
EOP	Exterior Orientation Parameters
FE	Fisheye (lens)
FLM	Focal Length Multiplier
FOV	Field of View
GAIN	GPS-Aided Inertial Navigation
GCP	Ground Control Point
GIS	Geographic Information System
GNSS	Global Navigation Satellite System
GNVL	Gainesville Airport CORS
GPS	Global Positioning System
h	Ellipsoid Height/Geodetic Height - Height Above Ellipsoid
H	Orthometric Height - Height Above Geoid
Hor	Horizontal
hr	Hour
Hz	Hertz
in	Inch
IMU	Inertial Measurement Unit
INS	Inertial Navigation System
IOP	Interior Orientation Parameters
KAR	Kinematic Ambiguity Resolution
KF	Kalman Filter
km	Kilometer

LC	Loosely Coupled (GPS/INS Integration)
LiDAR	Light Detection and Ranging
LSM	Least Squares Matching
m	Meter
mm	Millimeter
m/s	Meters per Second
MEMS	Micro Electro-Mechanical Systems
MP	Megapixel
MMS	Mobile Mapping System
N	North
NGS	National Geodetic Survey
OPK	Omega Phi Kappa
PDOP	Positional Dilution of Precision
POS™	Positioning and Orientation Systems
PM	PhotoModeler®
QA	Quality Assurance
QC	Quality Control
RGB	Red-Green-Blue
RLA	Reed Lab – Home of University of Florida Geomatics Department (Gainesville, FL)
RLAB	Reed Lab CORS Operated by Florida Department of Transportation
RLG	Ring Laser Gyroscopes
RMSE	Root Mean Squared Error
RPY	Roll Pitch Yaw
RTS	Rauch-Tung-Striebel
RTK	Real-Time Kinematic

s	Second
SA	Selective Availability
SCBA	Self-Calibrating Bundle Adjustment
SD	Standard Deviation
SIFT	Scale-Invariant Feature Transform
SLAM	Simultaneous Localization and Mapping
SNR	Signal to Noise Ratio
SPAN™	Synchronized Position Attitude Navigation
SV	Satellite Vehicle
TC	Tightly Coupled (GPS/INS Integration)
TS	Total Station
TT	Topcon Tools™ 7.2
U	Up (Vertical Component)
UAV	Unmanned Aerial Vehicle
UTM	Universal Transverse Mercator
Ver	Vertical
VA	Vision-Aiding
VS	Versus
WA	Wide Angle (lens)
WGS84	World Geodetic System 1984
WIE	Waypoint® Inertial Explorer™
ZUPT	Zero Velocity Update

Abstract of Thesis Presented to the Graduate School
of the University of Florida in Partial Fulfillment of the
Requirements for the Degree of Master of Science

MOBILE MAPPING BENEATH FOREST CANOPY: SYSTEM DEVELOPMENT AND
APPLICATION

By

Adam R. Benjamin

August 2011

Chair: Ahmed Mohamed
Major: Forest Resources and Conservation

Terrestrial Mobile Mapping Systems (MMS) can provide under canopy geospatial information to forest managers that is inaccessible from aerial vehicles and too time consuming for traditional land-based surveying methods. Methodology for designing, testing, and calibrating the georeferencing (positioning/orientation) and imaging MMS subsystems of the GatorMMS, a terrestrial forest MMS mounted on an All-Terrain Vehicle (ATV), is discussed. The principal components of these subsystems are the GPS-aided inertial navigation system and the digital single lens reflex (DSLR) camera. Due to lack of reliable GPS positioning under forest canopy, both GatorMMS applications explored herein focus on navigation trajectory precision. Using image thresholding to determine canopy density along a forested test track, canopy density is significantly correlated with the number of available satellites, PDOP, and navigation trajectory precision. Interestingly, time elapsed from static observation had the most significant correlation with navigation trajectory precision. Through vision-aiding (VA) using photogrammetric bundle adjustments, the navigation trajectory precision improves significantly including a one order of magnitude improvement by the heading orientation

parameter precision. This major breakthrough for the heading orientation parameter is essential because angular error propagates over the distance the object is from the sensor. A methodology to improve near real-time direct georeferencing is proposed via implementation of a sequential VA algorithm. Through simulation and field collected data sets, the sequential VA algorithm showed substantial gains in angular precision and angular accuracy.

CHAPTER 1 INTRODUCTION

1.1 Problem Background

From the family planning its next trip using Google Earth™ to the transportation engineer using LIDAR point cloud processing to perform preliminary highway overpass inspections, geospatial data sets are a common denominator that makes these inquiries all possible. The desire for geospatial information from government agencies, corporations, academic institutions, and consumers continues with no prospect of relenting. Mobile Mapping Systems (MMS) technology has enabled Geographic Information System (GIS) and geomatics professionals the ability to acquire more geospatial data in less time than traditional surveying methods and often at reduced costs (Li 1997). Unmanned Aerial Vehicles (UAV) and land-based MMS platforms are two data acquisition tools that have emerged to meet the demand for geospatial data.

Mobile Mapping Systems (MMS) have great potential to meet the needs of those who desire vast amounts of geospatial data without the constraint of a fixed location. However, there is inherent difficulty that comes with georeferencing from a mobile platform instead of a static one. Georeferencing is the process of determining the time, position/location, and attitude/orientation of an event in space (Skaloud 1999). Direct georeferencing (DG) incorporates the use of onboard inertial navigation system (INS) sensors to determine these parameters. When direct georeferencing from a mobile platform, kinematic positioning and dynamic orientation are additional unknown parameters that need to be resolved relative to static direct georeferencing. These mobile navigation trajectory computations are further compounded by gaps in the GPS position trajectory.

GPS-outage prone areas such as forests and urban environments pose a significant problem for geomatics professionals using MMS. Due to the value of natural resources and infrastructure in these environments, development of solutions to the direct georeferencing problem is necessary. Different sensors and techniques have been utilized to supplement the inertial navigation trajectory including vision-aiding (VA) methods. Due to the enormous file sizes and complex calculations, using the most efficient VA method is essential. Simultaneous batch post-processing of the imagery and navigation data is the most common VA method due to minimization of error (Wolf and Dewitt 2000). However, simultaneous VA does not afford the user the ability to perform real-time or near real-time mapping operations because all data must be collected prior to performing the batch operation. A couple examples of near real-time applications include machine control for forestry applications or disaster response in GPS signal obscured environments. Sequential VA has the potential for being a more efficient method for real-time applications; however, this method suffers from error propagation. Thus, the development of a sequential VA technique that limits error propagation would be beneficial to the geospatial community for near real-time applications.

Furthermore, many geodetic-grade GPS receivers and tactical-grade inertial navigation systems cost tens of thousands of dollars. Low cost, low accuracy GPS/INS cost hundreds of dollars. If the low cost systems can be supplemented by vision-aiding to provide a similar navigation trajectory to geodetic/tactical-grade systems, more people would have access to this technology. Greater access could lead to more MMS improvements and broader applications.

1.2 Motivation

Contemporary forest managers are challenged to make efficient decisions in a short amount of time and based on as much information as possible. Aerial geospatial platforms provide rapid acquisition of forest data but they often lack information on under-canopy structure, diameter at breast height (DBH) of trees, and ladder fuel data for forest fire risk assessment. Terrestrial MMS beneath forest canopy can fill the data gap at reasonable cost and fast turn-around time.

1.3 Objectives

The objectives of this thesis research are to (1) develop a terrestrial remote sensing mobile mapping system for use in forested areas – GatorMMS; (2) investigate GPS/INS processing techniques and operational methods for improving the navigation solution beneath forest canopy; (3) examine the relationship between forest canopy and navigation solution accuracy for MMS platforms in forests; and (4) investigate vision-aiding as a technique to improve direct georeferencing for near real-time applications.

1.4 Research Questions

The following three research questions will be addressed through the course of this thesis. What quantitative impact does the tree canopy density (CDI) have on the navigation solution accuracy of terrestrial MMS? Can VA improve the georeferencing solution in high CDI areas where signal outages are most prevalent? Can a sequential VA technique be developed to improve the direct georeferencing solution of aerial MMS for future application to terrestrial MMS?

1.5 Hypothesis

Due to the importance of GPS derived positions in the GPS-aided inertial navigation solution, expectations are that canopy density will be highly correlated with

navigation trajectory accuracy. As a result, it is hypothesized that terrestrial MMS direct georeferencing will benefit significantly from VA in highly signal degraded environments (high CDI areas). During this study, a proof of concept will be developed. The eventual real-time application will be a future development. The goal is that MMS developers will have a method for quantifying the forest canopy for use as an input in inertial navigation processing. This input will trigger the use of sequential VA for real-time applications.

1.6 Report Structure

This thesis project covers information on technology related to mobile mapping systems including INS, GPS, photogrammetry, and remote sensing. Chapter 2 is a review of previous literature regarding these technologies in both forested and non-forested environments. Chapter 3 covers the components of the GatorMMS including a discussion of the georeferencing system, imaging system, and coordinate systems. The georeferencing system testing for GatorMMS v1.0 is covered in Chapter 4. In Chapter 5, camera calibration and boresight/lever arm calibration is discussed as part of the imaging system testing. Chapter 6 is a discussion of the vertically-oriented camera system for analysis of the relationship between canopy density and navigation trajectory accuracy. In Chapter 7, the concept of VA from a terrestrial platform beneath forest canopy is explored. Chapter 8 discusses the implementation of a sequential vision-aiding algorithm from an aerial platform with the goal of improving the angular orientation of the platform. Conclusions and recommendations for future studies are covered in Chapter 9.

CHAPTER 2 LITERATURE REVIEW

2.1 Mobile Mapping Systems

Mobile Mapping Systems (MMS) are remote sensing platforms used to capture data for mapping of its surrounding environment. MMS has been defined as the "product that integrates concepts of kinematic geodesy, aerospace engineering, automatic control, remote sensing, and digital photogrammetry to acquire, store, and process measurable quantities that sufficiently describe spatial and/or physical characteristics of a part of the Earth's surface" (Hassan et al. 2006). Original developments in the MMS field were restricted to applications where the exterior orientation of the platform was derived from existing control points; however, drastic technological improvement in satellite and inertial navigation made geomatics and engineering professionals reevaluate the development of MMS (Schwarz and El-Sheimy 2004). Both land-based and aerial MMS have undergone drastic changes in the last two decades.

Airplanes were the original modern MMS platform for aerial photogrammetry. As defined in (Wolf and Dewitt 2000), photogrammetry is the "art, science, and technology of obtaining reliable information about physical objects and the environment through processes of recording, measuring, and interpreting photographic images and patterns of recorded radiant electromagnetic energy and other phenomena." This broad definition includes two clear areas of photogrammetry: interpretative and metric. Interpretative photogrammetry involves object recognition, identification, and judgment of object significance through systematic analysis (ibid). Metric photogrammetry involves precise measurement of photographs to determine relative location of points in

the images for the purpose of distance, area, elevation, angle, and elevation calculations (ibid). Aerial and land-based MMS have been used extensively in both of those photogrammetric areas.

For mapping the precise location of objects, metric photogrammetry is the only method. To obtain the desired object locations, the orientation and position of the camera/sensor is a necessity. For years, the only practical solution for camera position and orientation determination was knowledge of the absolute position of objects on the ground. The relationship between the absolute object coordinates, the corresponding image coordinates, and the camera calibration parameters would reveal the exterior orientation parameters of the camera through rigorous computations. Establishing extensive networks of photo identifiable ground control points is both costly and time-consuming. Thus, development of positioning and orientation sensors onboard MMS to supplement ground control points was celebrated throughout the photogrammetric community (Schwarz and El-Sheimy 2004). Typically consisting of a Global Positioning System (GPS) antenna/receiver and an Inertial Measurement Unit (IMU), these positioning and orientation sensors are collectively referred to as a GPS-aided Inertial Navigation System (INS).

Unmanned Autonomous Vehicle (UAV) and land-based MMS platform development have grown exponentially with the technological advances in INS. The small size and versatility of UAVs provides users a cost-friendly and efficient approach to small aerial mapping projects. The diverse research areas investigated with UAVs include wildlife and ecological monitoring (Perry 2009; Wilkinson et al. 2009), tidal zone mapping (DiGruttolo 2010), and automatic detection of forest fires (Merino et al. 2006).

Meanwhile, various research groups and corporations saw the niche that terrestrial MMS provided people looking to monitor infrastructure from street view. Many examples of recent developments in MMS include the use of vans and trucks as the mobile platform (Talaya et al. 2004; Schwarz and El-Sheimy 2004; Alshawa et al. 2007; Grafe 2007; Barber et al. 2008; Haala et al. 2008; Glennie 2009). Predominantly, these vehicles were operating with LiDAR (Light Detection and Ranging/laser scanners) and cameras as remote sensors for monitoring infrastructure in the built environment. Furthermore, boat-based LiDAR has recently become viable as a supplement to the underwater usage of side-scan sonar employed by hydrographic surveying vessels (Mohamed 2007; Alho et al. 2009). Unmanned Autonomous Vehicles and land-based MMS would not be viable for mapping without the underlying navigation trajectory solution: the position and orientation of the sensor. Further information regarding the inertial navigation and global positioning sensors will be discussed in Chapter 3.

While GPS and IMU data are the dominant navigation trajectory updates, other sensors can also provide valuable update information. Distance measurement instruments (DMI) can provide wheel revolution updates for the GPS-aided inertial navigation trajectory (NovAtel 2006). These velocity-aiding odometer measurements have been successfully integrated to improve positional accuracy (Hassan et al. 2006). Furthermore, image-matching algorithms can be used to detect targets and provide positional updates (Tao et al. 2001; Hassan et al. 2006).

Image matching for navigation updates and mapping features from a mobile platform requires sensors able to capture data regarding the physical characteristics it passes. Digital cameras, digital video cameras, and two-dimensional laser scanners are

the most frequently used data acquisition devices (Petrie 2010). Typical specifications for MMS digital frame cameras include small format sizes (1 to 2 megapixels), high framing rates (7 to 15 Hz), and very short exposure times to eliminate blurring (ibid). Laser scanners capture data by measuring angles and distance to objects the MMS passes. Typically, these scanners are operated in 2D mode which means the scan angle does not change; thus, the scanner continuously scans in a vertical plane (ibid). As the MMS moves, the third dimension of the output point cloud is created.

2.2 Vision-Aiding

Vision-aiding of the navigation solution using imagery has become an integral component of low-cost IMU/GPS sub-systems providing direct georeferencing to remote sensing systems. The data workflow to recover the orientation parameters rigorously requires the simultaneous handling of large amounts of imagery and navigation data. In some situations, with small UAVs for example, a flight block of thousands of images is the norm. The normal matrix of the blended imagery and navigation data can be very large in size for regular computers to handle efficiently. A Kalman filtering approach to sequentially process the blended navigation and imagery data can be used. Georeferencing parameters are then computed for every exposure station.

To properly direct georeference imagery, the position and orientation of the sensor at exposure times must be known. These elements are commonly referred to as exterior orientation parameters (EOP). In indirect georeferencing, aerial triangulation is used to obtain the exterior orientation parameters of an individual exposure station using known ground control point coordinates and its counterparts in the images. The other interest of aerial triangulation (AT) is obtaining the object space coordinates of other points imaged in the aerial images.

Bundle Adjustment (BA) is a technique used in analytical AT to obtain EOPs. BA uses a least squares approach to minimize the errors of a bundle of rays connecting the photo coordinate measurements with the control coordinates on the ground. This is usually done by incorporating either the collinearity equations to determine the EOPs through determination of the object space coordinates of the imaged points or directly through the coplanarity condition (Kersten and Baltsavias 1994; Tommaselli and Tozzi 1996; Haala et al. 1998; Wolf and Dewitt 2000; Mikhail et al. 2001; Wang and Clarke 2001).

Collinearity is the condition that the incident nodal point of the lens (exposure station), any object point, and its corresponding image point all lie on the same line in three-dimensional space (Wolf and Dewitt 2000). Coplanarity, on the other hand, is the condition that two exposure stations of a stereo-pair, any object point, and the corresponding image points of the two photos all lie in the same plane (ibid). Since no object coordinates are involved in the coplanarity condition, initial approximations of the object space coordinates are not necessary. This proves to be a valuable asset for using the coplanarity equation.

Bundle adjustments can be performed either sequentially or simultaneously. Each method has three main components: relative orientation of each stereo model, connection of adjacent models to form continuous strips and/or blocks, and simultaneous adjustment of the photos from the strip/block to ground control. Relative orientation is used to determine the relative angular attitude and positional difference between two photographs when the images were captured (ibid). Absolute orientation takes the relatively oriented stereo models and transforms them to the ground using

three-dimensional conformal coordinate transformations. The unknown quantities of BA in either method are the object space coordinates (XYZ) of object points and the exterior orientation parameters (georeferencing parameters) of each photograph.

Both sequential and simultaneous bundle adjustments have certain advantages and disadvantages. The greatest disadvantage for sequential bundle adjustments is the nonlinear accumulation of random error along an image strip as more stereo models are added to the adjustment (ibid). Simultaneous BA avoids this error accumulation by processing all measurements at once. This provides a more robust method for determining the optimal solution. Simultaneous BA, however, comes with a computational burden in the form of huge matrix operations imposed by the large amounts of imagery in the strips/blocks, specifically with small format imagery. If a method existed for reducing error accumulation in sequential BA, the computational time incurred by doing the adjustment sequentially as opposed to simultaneously could be a great advantage especially in near real-time applications. Consequently, many experts especially in the field of navigation are immensely interested in sequential estimation as a pressing research topic.

A number of approaches to sequential estimation through bundle adjustments are used in the field of robot vision or vision metrology (Kersten and Baltsavias 1994; Edmundson and Fraser 1998; Di et al. 2008). To accurately obtain the orientation and position of the robot, a simultaneous bundle adjustment of all the previous geospatial data would not be feasible as the robot/UAV needs the geospatial information in near real-time to continue navigation. Thus, sequential estimation theory is used. Sequential estimation approaches using collinearity equations with image-matching techniques are

common (Kersten and Baltasvias 1994; Tommaselli and Tozzi 1996; Haala et al. 1998; Wang and Clarke 2001). The algorithm developed in (Webb 2007) applies coplanarity as the observation model for Kalman filtering to the sequential aerotriangulation problem with success. The premise of that research was navigation, not georeferencing the acquired imagery. Thus, research of sequential BA using Kalman filtering and optimal smoothing as a method for reducing the sequential accumulation of error normally associated with AT to provide accurate and precise georeferencing parameters is lacking.

2.3 Forest Mapping

In 2002, forests covered approximately 749 million of the 2.3 billion acres of land mass in the United States (Smith et al. 2004). This one-third proportion of forest land to non-forest land has remained relatively stable for the past 100 years; however, many forests are quite dynamic as the lands are logged and managed for their timber resources. Of the 749 million acres, only 10% (77 million acres) is reserved from commercial timber harvesting (ibid). Furthermore, timberland covers more than 504 million acres of forest land (ibid). Timberland is forest land able to produce more than 20 cubic feet per acre per year without being legally withdrawn from timber production. The volume and value of timberland resources necessitates efficient management techniques which includes having an accurate inventory.

Accurately positioning oneself in a forested environment is critical to many real-time and near real-time applications such as mapping forest inventories (Zengin and Yesil 2006), fighting forest fires (Xiaopeng et al. 2008), and harvesting trees with machine control (Rossmann et al. 2009). Since GPS positioning requires accurate timing and ranging between earth orbiting satellites and the GPS receiver, sky

obstructions pose an inherent problem to acquiring GPS signals under a forest canopy. Thus, many studies have focused on different aspects of determining GPS position in a forest.

2.3.1 GPS Positioning in the Forest

After Selective Availability (SA) was turned off on 1 May 2000, a Japanese research group studied the Signal to Noise Ratio (SNR) of GPS signals impacted by forest conditions including natural forest, plantation forest, forest road, and forest clearings (Gandaseca et al. 2001). A higher SNR indicates a better signal. Logically, the clearing area had the highest SNR and the plantation area had the lowest SNR due to dense tree canopy. Gandaseca et al. (2001) also showed that using a GPS antenna height of 4.2m significantly reduced position errors relative to 1.0m antenna height. Unfortunately, an antenna height of 4.2m is unrealistically high for most practical survey applications.

A performance study of Real-Time Kinematic (RTK) GPS using two geodetic-grade GPS receivers and a navigation-grade handheld GPS receiver under forest cover was conducted to compare point positions from the different techniques (Zengin and Yesil 2006). Nine ground control points were surveyed multiple times in nine separate stands. Each stand had a unique dominant tree species. Absolute accuracy could not be assessed since the study areas lacked absolute ground control point coordinates; thus, the two position solutions were compared relative to each other. Through numerous trials, the RTK measurements understandably were more precise (i.e. greater repeatability) than the handheld receiver measurements. Deciduous forest stands had more consistent positional precision results than coniferous stands. This difference between pine and deciduous stands has been well-documented in previous GPS

studies analyzing forest cover type during leaf-on/off and seasonal changes (Deckert and Bolstad 1996; Sigrist et al. 1999, Piedallu and Gegout 2005).

An extensive study in the forest of northeast France investigated the influence of four factors on GPS accuracy: receiver type, forest cover (open cover, coppice regeneration, and deciduous high forest), GPS survey components, and season (winter or summer) (Piedallu and Gegout 2005). The number of recordings, Positional Dilution of Precision (PDOP) threshold, time interval between recordings, and differential correction availability were modified as part of the GPS survey component analysis for four GPS receivers ranging from navigation-grade to mapping-grade. Using one ground control point with decimeter-level accuracy in each forest cover class, the only insignificant factor on GPS accuracy was the season. Receiver type and forest cover each modified the positional accuracy by a factor of 2 to 3. Increasing the number of recordings, increasing the time interval, or decreasing the PDOP threshold significantly improved precision of the positional solution.

2.3.2 Forest Canopy Density Affecting GPS Positioning

While forest canopy can significantly alter GPS performance, one omission in these studies was the lack of quantification of forest canopy characteristics such as crown cover and canopy closure. The "proportion of the sky hemisphere obscured by vegetation when viewed from a single point" is canopy closure (canopy density); meanwhile, canopy cover describes the "proportion of the forest floor covered by the vertical projection of the tree crowns" (Jennings et al. 1999). Figure 2-1 modified after Jennings et al. (1999) depicts the difference between these two terms. With respect to GPS positioning and receiving satellite signals at one moment in time, forest canopy density is the preferred metric. Thus, skyward-looking hemispherical photography,

which captures a wide angle view of the forest canopy from a single point, is used extensively in GPS studies relating canopy density to GPS positional performance (Jennings et al. 1999; Sigrist et al. 1999; Frazer et al. 2001; Holden et al. 2001; Zheng et al. 2005; Hu et al. 2009).

Holden et al. (2001) investigated a method for relating GPS performance to forest canopy using this skyward-looking hemispherical photography above the ground control points. Precision of the differential GPS solution was strongly correlated with total sky obstruction, size of the largest hole in the canopy, and fragmentation of the sky view. The authors found there was no significant difference in positional precision between open sky view and 20% closed canopy. However, positional precision degraded significantly after 20% closed canopy by a factor of 5 to 7 times for points under heavy closed canopy. Sigrist et al. (1999) analyzed the impact of quantified canopy characteristics on PDOP and absolute accuracy of the GPS positional solutions. Interestingly, Sigrist et al. (1999) reported that absolute accuracy, as measured by root mean square error, decreased by fourfold from open sky to 20% canopy cover. Absolute accuracy degradation slowed considerably with only a 50% increase in RMSE from 20% canopy cover to almost 100% closed canopy. Zheng et al. (2005) confirmed the Holden et al. (2001) study conclusions by evaluating GPS positional accuracy along a forested trail of 26 ground control points. Using an analysis of variance (ANOVA) method, the real-time GPS positional accuracy was significantly degraded by increases in the forest canopy density. From Holden et al. (2001) and Sigrist et al. (1999), the contrast between accuracy and precision is apparent. Having a precise solution does not mean that the GPS positional solution is accurate. Satellite obstruction of a minimal

portion of the sky (>20%) can alter the geometry of the satellite constellation such that the positional fixes are precise (high repeatability) but inaccurate. Likewise, the deterioration of precision may only minimally impact the already poor GPS positional accuracies.

Both Sigrist et al. (1999) and Holden et al. (2001) described the conversion of gray-scale images to black and white images. However, the thresholding methodology used to determine percentage of sky obstruction pixels was omitted. In contrast, Zheng et al. (2005) implemented the image thresholding algorithm called Otsu's method. He described in detail how he used this method to differentiate sky pixels from canopy pixels in the Olympus C-3040 digital images. From Otsu's method which minimizes the intra-group variance between sky and canopy pixels, the canopy density index (CDI) metric was determined. The Euclidean distance approximation transformation used to quantify the obstruction pattern (largest canopy hole) and fragmentation of sky view metrics was explained in the Holden et al. paper.

Comparing digital and film cameras using hemispherical photography for forest canopy metric determination, Frazier et al. (2001) found that the Nikon® Coolpix® 950 produced canopy openness estimates that were 1.4 times greater than conventional Nikon® F film camera estimates. The authors advised a cautious approach to using this digital camera model when making forest canopy measurements. Significant advances in digital camera technology have been made since 2001. However, chromatic aberration common with consumer level digital camera optics might still cause a problem. Thus, the impact color blur can have on the detection of vegetation edges and canopy gaps should be monitored in this research study.

Airborne laser swath mapping (ALSM) is another remote sensing technique that has been used to quantify the forest structure and canopy density in the development of a method to predict reliability of a GPS receiver under forest canopy (Wright 2008). Through LiDAR post-processing and GPS signal-to-noise ratio (SNR) analysis, GPS signal loss was strongly correlated with the complexity of local canopy structure and density. Encouragingly, the development of a model for prediction of GPS SNR based on canopy structure showed promise for use in future 2D signal attenuation maps.

The remote sensing techniques developed in these quantification studies will be valuable for characterizing the forest canopy density of the trails used in this study. The methodology set forth in the image thresholding algorithms will enable the author to accurately characterize the canopy closure during the inertial trajectories. This characterization will be useful in addressing a primary research question regarding the implementation of vision-aiding in high canopy density areas.

2.3.3 Mobile Mapping Systems Under Forest Canopy

Through this review of GPS performance studies in forests, signal degradation and outages are obstacles that need to be overcome in the design of MMS for forested environments. Fortunately, development of MMS in signal degraded environments is an ongoing academic and industrial pursuit. Due to the high initial cost of the systems, much of the MMS research involving GPS-outage prone areas centers on the difficulty of obtaining an accurate navigation trajectory in urban areas for commercial applications (Bayoud 2005; Kennedy et al. 2006; Nassar et al. 2007; Kukko et al. 2007; Haala et al. 2008). Signal blockages from buildings, overpasses, and/or trees were encountered in each study. Significant improvements in the navigation trajectory accuracy and positioning availability were seen with GPS-aided inertial navigation relative to a GPS-

only solution in each case. Kennedy et al. saw greater improvement during signal outages when a distance measurement instrument (DMI) update was introduced into the filtering solution acquired with Novatel®'s tactical-grade Synchronized Position Attitude Navigation (SPAN™) system. Both loosely-coupled and tightly-coupled GPS/INS integration techniques were tested. With minute-long GPS outages, the DMI updates improved relative trajectory solution accuracy by 55% relative to the baseline navigation grade IMU trajectory (Kennedy et al. 2006).

For surveying under heavy forest conditions, an Applanix™ POS™ LS backpack mounted inertial land positioning/navigation system was developed and tested (Gillet et al. 2001; Reutebuch et al. 2003). The authors emphasized the importance of using frequent zero velocity updates (ZUPTS) to dampen the 0.01 degrees/hour drift associated with the ring-laser gyros (RLG) in the twenty year old navigation grade IMU. ZUPTS occur when the MMS remains stationary for a set period of time. Initial results showed the growth rate of both the horizontal and vertical real-time errors to be approximately 2 meters per kilometer (Gillet et al. 2001). Additional field testing of the Applanix™ POS™ LV backpack system evaluated positional accuracy and terrain profile development potential (Reutebuch et al. 2003). To test the ability of the POS™ LV as an inertial-only system, this testing did not utilize GPS updates. The MMS was initialized on a point of known coordinates at the beginning and end of each run. Using ZUPTS on average every 40 seconds (s), the system had an average positional accuracy of 2.3ft in real-time and 1.4ft in post-processing. Comparing the terrain profile generated by the backpack INS with a previously generated LiDAR digital terrain model (DTM), average post-processed elevation differences along the profiles was 0.7ft. While

less frequent ZUPTs are preferred, this study is promising for a backpack INS system under heavy forest cover.

Nassar et al. (2007) analyzed different filtering and smoothing approaches to deal with GPS signal outages in computation of navigation trajectories. The non-photogrammetric bridging methods utilized showed drastic improvement in position errors regardless of which Kalman filtering technique was implemented. This study was focused primarily on improving the post-processed solution. Thus, real-time applications were not covered with this approach. Machine control for forest harvesting equipment has encouraged research in real-time forest navigation due to minimal satellite coverage under forest canopy. Approaches involving laser scanners and other non-photogrammetric sensors were the most common in forest navigation applications (Rossman et al. 2009; Morales et al. 2010). These techniques utilized Simultaneous Localization and Mapping (SLAM) algorithms. Various photogrammetric techniques are in development for aiding UAV navigation in real-time (Webb 2007; Samadzadegan et al. 2007; Taylor 2009). While land-based robots using vision-aiding has been researched (Kersten and Baltsavias 1994; Edmundson and Fraser 1998; Bayoud 2005; Di et al. 2008), studies of terrestrial based applications of image-aiding in the forest are lacking. Thus, image-aiding of the navigation solution in forested areas is a research area in need of further study.

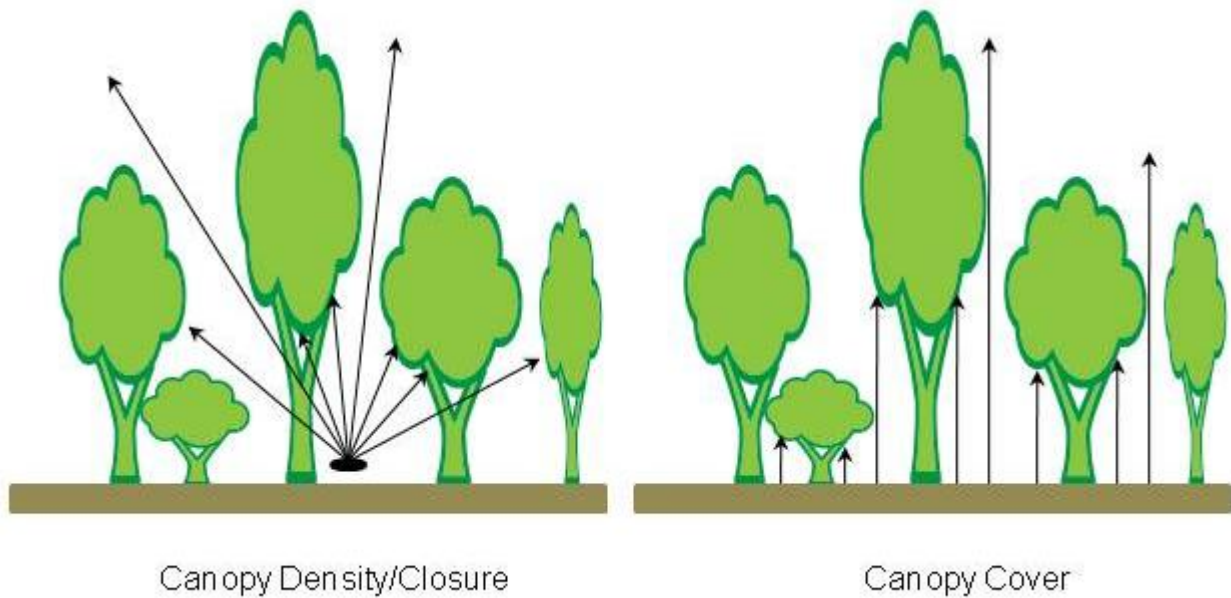


Figure 2-1. Characterization of forest canopy: canopy density versus canopy cover (modified after Jennings, S., N. Brown, and D. Sheil. 1999. Assessing forest canopies and understory illumination: canopy closure, canopy cover and other measures. *Forestry*. 72(1): 59 -74.)

CHAPTER 3 GATORMMS COMPONENTS

3.1 GatorMMS – The Mobile Mapping System for the Forest

Before designing a mobile mapping system, consideration must be paid to the platform from which the direct georeferencing will occur. The subject environment plays a large role in platform selection. When operating in a forest, roads are often unpaved and bumpy. Additionally, the platform should be capable of going off the trails. Aerial vehicles would be ideal; however, trees would obscure imagery if flown above the canopy. Flying amongst the canopy would be dangerous and unreliable due to line of sight issues. Thus, the availability of an all terrain vehicle for deployment of the GatorMMS provided a logical solution to any rugged terrain encountered.

Two primary versions of the ATV mounted GatorMMS have been deployed on board the 2006 Arctic Cat 400 4x4 ATV. GatorMMS v1.0 was purely a navigation and georeferencing system testing platform. Figure 3-1 shows the v1.0 components including Novatel®'s SPAN™ GPS/INS system and a carbon fiber antenna frame mount. All components were mounted to the rear ATV speed rack with tie straps. Results of the testing will be discussed in Chapter 4. Design limitations of GatorMMS v1.0 include flexing of the antenna frame mount during mobile observations, low profile of the GPS antenna relative to the ATV driver, prolonged setup time to secure all components to the ATV, and potential for shifting components due to ATV vibration and the loosening of tie straps. As shown in Figure 3-1, GatorMMSv2.0 has both primary mobile mapping subsystems: the georeferencing system and the imaging system. V2.0 addressed the limitations of v1.0 through the use of a rigid aluminum frame for securing all subsystem components. Mounting this frame to a motorcycle stand bolted to the ATV

elevated the system 16in above the ATV speed rack providing a better view for the imaging system and substantially decreasing the signal obstructions from the ATV driver. Details of the components of these MMS subsystems are given in subsequent Chapter 3 sections.

3.2 Georeferencing System

Recall the georeferencing system is responsible for determining the time, position/location, and attitude/orientation of an event in space. Often this event is the moment the shutter closes for an aerial or terrestrial photograph. The exterior orientation parameters for the image are the georeferencing solution. Prior to onboard inertial navigation sensors, georeferencing a strip of aerial photos was only possible through a bundle adjustment utilizing a network of ground control points (GCPs). With known coordinates for the GCPs, the bundle adjustment output includes the exterior orientation parameters for the attitude and position of each image. Figure 3-2 depicts indirect georeferencing for a stereo pair of aerial images from GCPs. Direct georeferencing provided by onboard INS sensors reduces the need for dense networks of GCPs. Instead, GCPs can serve as check points or additional control redundancy in the bundle adjustment. Direct georeferencing has been a rapidly developing area of concern for geospatial experts including navigation, remote sensing, and photogrammetry specialists. The remainder of the section discusses the direct georeferencing components: GPS and INS.

3.2.1 GPS

GPS position is the primary position input for the navigation component of MMS. GPS antennas acquire signals from the GPS satellite constellation orbiting Earth. These signals are transmitted to the GPS receiver for signal processing. After correcting for

many error sources including timing and atmospheric effects, GPS coordinates are calculated from the intersection of satellite ranges. To obtain a position fix, signals from four satellites are necessary to solve for time and the position in three-dimensions: latitude, longitude, and ellipsoidal height (Zengin and Yesil 2006). All GPS receivers are not created equal. Table 3-1 outlines the three classes of GPS receivers: survey-grade, mapping-grade, and consumer-grade. For the most accurate direct georeferencing solution, a survey-grade GPS antenna and receiver should be used. Alternatively, a mapping-grade receiver can be used as long as GPS post-processing techniques are capable of deriving survey-grade accuracies from the mapping-grade data. Recent research studies have shown that these GNSS processing algorithms with mapping-grade GPS receivers are efficient in obtaining survey-grade accuracies (DiGruttolo 2010).

3.2.2 GPS-Aided Inertial Navigation Systems

The INS forms the trajectory subsystem of the MMS. The IMU, the backbone of the INS, has two orthogonal triads of sensors. One triad consists of accelerometers to measure acceleration along three axes. Three orthogonal gyroscopes form the triad used to measure rotational velocity along the three axes. The orthogonal property means the three axes (XYZ or ENU) form right angles to each other. The orientation accuracy of an IMU is mostly determined by the gyro drift rate of the gyroscope sensor (Schwarz and El-Sheimy 2004). Thus, IMUs are classified according to the characteristics of the gyroscope drift rate. Table 3-2 classifies the different grade gyroscopes based on these drift rates.

Strategic-grade and navigation grade IMUs are extremely expensive. Thus, their use in forest MMS research for future applications is not practical. Furthermore,

strategic-grade IMUs do not require GPS positional updates for accurate georeferencing after initialization for months at a time. Their usage would render the investigation of minute long GPS outages due to forest canopy obstruction moot. Tactical-grade and low-accuracy grade IMUs are more likely to be used in a terrestrial or inexpensive MMS. Hence, these grade inertial measurement units are investigated in this study.

Accelerometers form the other sensor triad in an IMU. These sensors measure the acceleration of the body along the three orthogonal axes. The accelerometer data set is integrated with the attitude (orientation) measurements for an inertial trajectory determination. Typically, update rates for the INS system are 100 hertz (Hz) or times per second. The typical position/velocity update rate from a GPS receiver for a GPS-aided INS is 1Hz.

Without GPS positional updates, the drift associated with the lower grade IMU sensors would result in an unusable navigation trajectory. GPS and INS are complimentary because the errors are highly non-correlated. The dominant INS error is long-term drift error (error propagates over time); the dominant GPS error is short-term white noise (errors for each moment of measurement are independent) (Schwarz and Wei 2000). Thus, the INS system is best suited for filling in short gaps in the GPS determined navigation trajectory.

There are two primary GPS/INS integration techniques. The simplest closed loop GPS/INS integration approach is loosely coupled (LC) integration (Figure 3-3). The GPS position and velocity are computed in a separate filter before being integrated with the INS measurements. A common but more complex integration technique is the tightly coupled (TC) integration approach (Figure 3-4). Instead of integrating a previously

computed GPS position and velocity into the GPS/INS integration filter, satellite phase ranges and range rates are integrated. The advantage of TC processing is the ability of the TC filter to use less than the previously required four satellite ranges. TC integration will be extremely important under heavy forest canopy where acquisition of four satellite ranges at one epoch is unlikely. Unless four satellites were in view to calculate a GPS position, the GPS ranges that were collected would not be used in a LC integration approach. Thus, use of all measurements in the TC integration approach should improve the overall accuracy of the TC navigation trajectory.

Both versions of GatorMMS (Figure 3-1) employed Novatel®'s SPAN™ (Synchronous Position, Attitude and Navigation) system as the primary georeferencing system. The system consists of a tactical-grade Honeywell™ AG58 IMU, a survey-grade Novatel® DL-4plus GPS receiver, and a survey-grade Novatel® 702-GG antenna. The experimental low-cost inertial navigation system consists of a Magellan® AC12 L1 phase only GPS receiver with a low-accuracy grade MEMSense H3 IMU. GPS signals are split to each GPS receiver from the geodetic-grade Novatel® GPS-702 GG antenna. Figure 3-5 shows the relative size discrepancy in the housing between the 1°/hr tactical-grade AG58 IMU and the 100°/hr low accuracy H3 IMU.

3.3 Imaging System

The imaging system comprises the second subsystem of a MMS. Historically, film cameras were the predominant imaging sensors. However, digital cameras have superseded film cameras as the non-LiDAR imaging sensor used in virtually all terrestrial based MMS. Instead of imaging to film, the light photons from the lens are converted to electrical charge by individual diodes arranged on a charge-coupled device (CCD) array (Wolf and Dewitt 2000). Each diode corresponds with a pixel in the

resultant image. While the CCD array eliminates the need for film distortion corrections, there are imperfections in the array from the manufacturing process that can be resolved in the camera calibration.

3.3.1 Camera

The GatorMMSv2.0 employs a digital single lens reflex (DSLR) Nikon® D200 camera. This 10 megapixel (MP) camera is equipped with a flash sync terminal and a timer function capable of capturing 999 images at a minimum interval of 1Hz. The flash sync terminal was essential for providing an output signal that could be relayed to the DL-4plus receiver. After configuration, the Novatel® receiver marked each time the shutter closed in the raw navigation data file. Without this functionality, the timing differences between the internal camera clock timer and the receiver clock would have yielded imprecise results. The receiver clock is updated via the GPS signals.

When configuring the D200 for a MMS test, attention was given to the DSLR settings that could severely impact the quality of the terrestrial imagery. The most important settings were the aperture and the shutter speed. Aperture is the size of the opening in the lens which allows light onto the CCD array. Often times, the aperture is given as an f-stop number; a smaller f-stop means a larger aperture. When using a larger aperture, a greater proportion of the lens is being used. Subsequently, this increases the amount of distortion present in the resultant image. The shutter speed is the time between the mechanical shutter opening and closing. Thus, the shutter speed also affects the amount of light reaching the CCD array. When imaging static objects from a moving platform or moving objects from a static platform, the goal is to use the quickest shutter speed to capture the objects without blur. The basic concept for MMS operation is to find a balance between using the smallest aperture to reduce distortion

and the quickest shutter speed that still allows in enough light to properly image objects on the CCD array. The wide variation of shadowed areas in the forest along the MMS test track further complicated the lighting for determination of the proper settings.

The D200 lacks a full frame CCD array. This means images captured with a 50mm lens will have a smaller FOV on the D200 than images captured with a 50mm lens on a film or full frame DSLR camera. To determine the equivalent focal length for a full frame camera, a focal length multiplier (FLM) needs to be used with the focal length for the cropped sensor. The D200 has a 1.5 FLM.

3.3.2 Lenses

To properly implement vision-aiding through the use of stereo models, overlap between successive images is essential. Since the minimum timing interval for the D200 is 1Hz and the D200 lacks a full frame, two methods existed to get the necessary overlap: increase the field of view (FOV) or travel at a slower speed. For future applications, increasing the FOV was the most logical approach. A fixed focal length 24mm f/2.8D AF Nikkor® wide angle (WA) lens and an 8mm f/3.5 Manual Focus Pro-Optic® fisheye (FE) lens were explored as two lenses that could increase FOV for the mobile mapping operation (Figure 3-6). The equivalent focal length for these lenses is 36mm and 12mm, respectively.

The WA lens has central perspective geometry found in the common pinhole camera model. Figure 3-7 illustrates the difference between WA central perspective geometry and FE projection geometry. The FE lens captures a much greater FOV; however, the tradeoff of this expanded FOV is a substantial increase in radial distortion. Thus, the calibration model for a fisheye lens is more complex than the standard pinhole

camera (central perspective geometry) calibration model. Camera calibration is discussed in detail in Chapter 5.

The D200 DSLR camera is capable of being mounted either horizontally or vertically on the GatorMMSv2.0 aluminum frame (Figure 3-6). The horizontal orientation is for the VA component of the research. The vertical orientation is for capturing images of the forest canopy for canopy density determination.

3.4 MMS Coordinate Systems

The GatorMMS georeferencing and imaging systems have been discussed as separate entities to this point. Vision-aiding relies on the integration of both subsystems into one MMS. To discuss sensor integration, knowledge of the sensor coordinate frames (CF) and sensor offsets is necessary. The discussion of these relationships that follows is derived from Ellum and El-Sheimy (2002). Figure 3-8 depicts the physical relationship between the origin of the IMU orthogonal axes, the GPS antenna reference point (ARP), and the incident nodal point of the camera lens. For simplicity, the three sensors are referred to as IMU, GPS, and camera. The mathematical relationship between the coordinates of a point in the mapping CF (\mathbf{r}_p^{Map}) and the same point in the camera CF (\mathbf{r}_p^{cam}) is expressed in Equation 3-1 as:

$$\mathbf{r}_p^{Map} = \mathbf{r}(t)_{GPS}^{Map} - \mathbf{R}(t)_{IMU}^{Map} \mathbf{R}_{cam}^{IMU} (\mathbf{r}_{GPS}^{cam} - \mu_p^P \mathbf{r}_p^{cam}) \quad (3-1)$$

where

- $\mathbf{r}(t)_{GPS}^{Map}$ Coordinates of the GPS ARP in the mapping CF
- $\mathbf{R}(t)_{IMU}^{Map}$ Rotation matrix from the IMU CF to the mapping CF
- \mathbf{R}_{cam}^{IMU} Rotation matrix from the camera CF to the IMU CF

\mathbf{r}_{GPS}^{cam} Vector from the camera to the GPS ARP in the camera CF

μ_p^P Scale between the camera CF and mapping CF

Determining \mathbf{r}_{GPS}^{cam} and \mathbf{R}_{cam}^{IMU} is part of the boresight and lever arm calibration discussed in Chapter 5. Using the mathematical relationship between the imaging and georeferencing subsystems makes the vision-aiding component of MMS operation feasible.

Table 3-1. GPS receiver classification. Note that accuracy is dependent on many factors. This is expected accuracy in optimal conditions.

GPS Receiver Class/Grade	Expected Accuracy (m)
Survey	± 0.01
Mapping	± 1
Consumer/Recreational/Navigation	$\pm 5-10$

Table 3-2. Inertial navigation gyroscope classification (Schwarz and El-Sheimy 2004)

Gyroscope Class/Grade	Constant Drift Rate (deg/h)
Strategic	0.0005-0.001
Navigation	0.002-0.01
Tactical	1-10
Low-accuracy	100-10,000



A



B

Figure 3-1. GatorMMS platform configurations. A) v1.0 – Georeferencing subsystem only, B) v2.0 – Georeferencing & imaging subsystems (images courtesy of author)

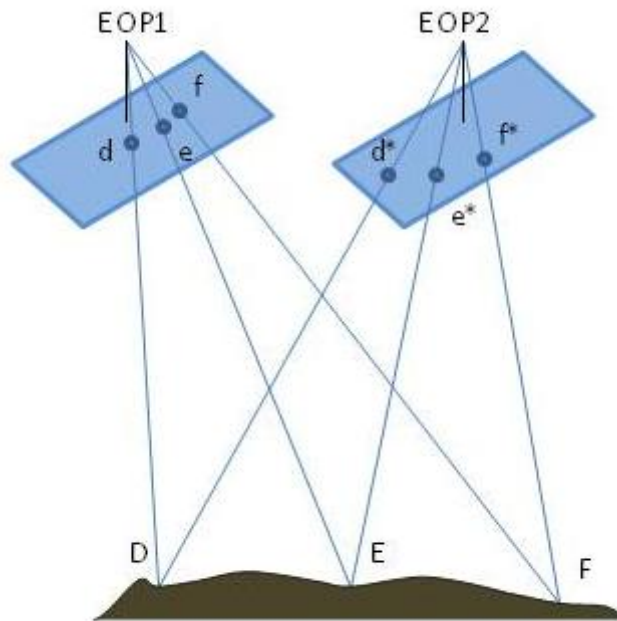


Figure 3-2. Indirect georeferencing - Collinearity condition for an aerial stereo model with EOP1 and EOP2 derived from the known coordinates of GCP-D, GCP-E, and GCP-F

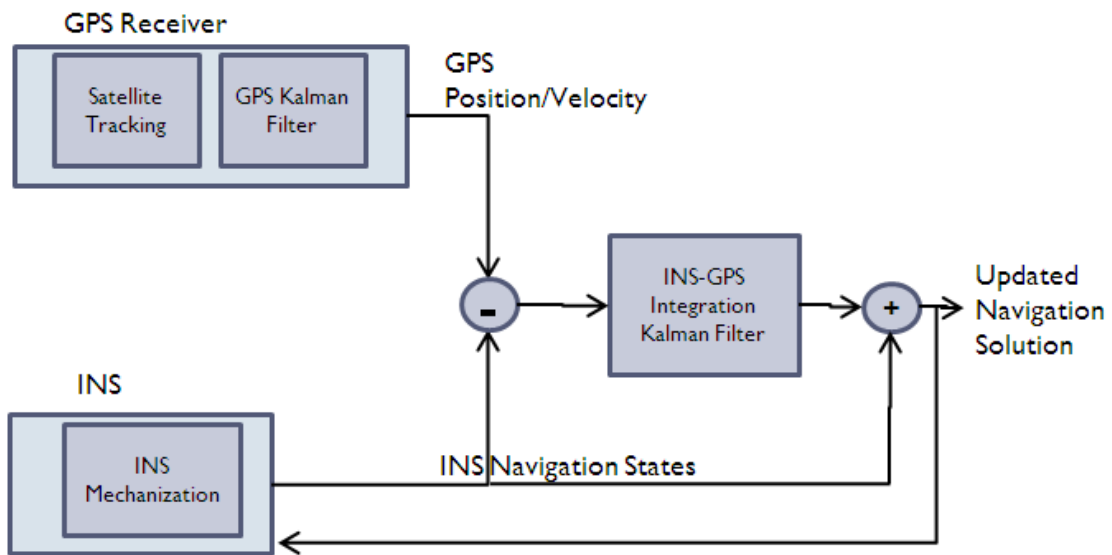


Figure 3-3. Loosely coupled GPS/INS integration flow chart (revised with permission from Mohamed, A.H. 2010. SUR 6535 GPS/INS Integration – Course Notes. University of Florida: Gainesville, Florida.)

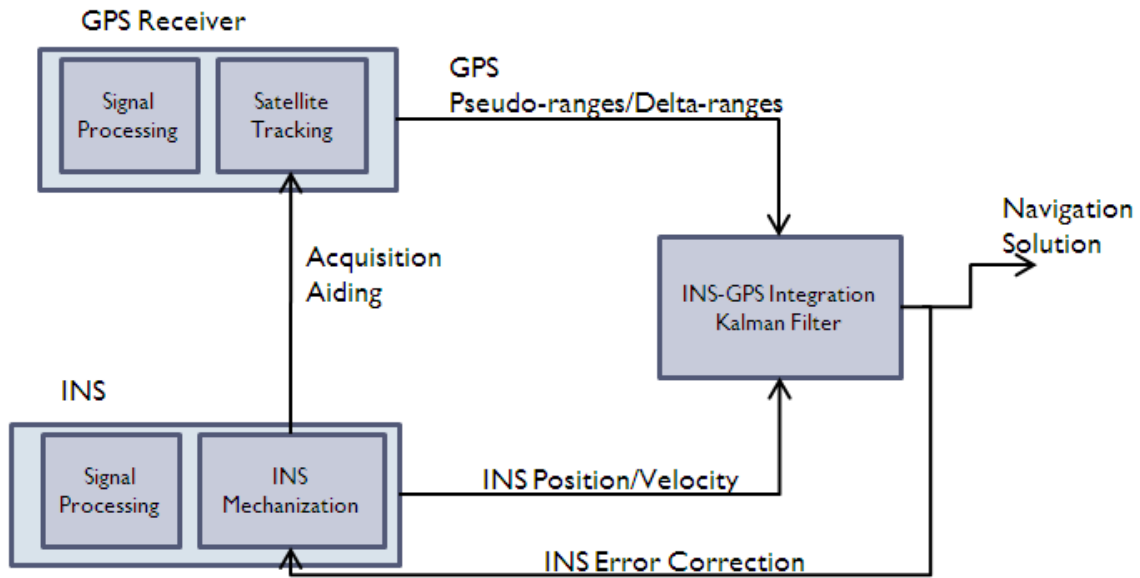


Figure 3-4. Tightly coupled GPS/INS integration flow chart (revised with permission from Mohamed, A.H. 2010. SUR 6535 GPS/INS Integration – Course Notes. University of Florida: Gainesville, Florida.)

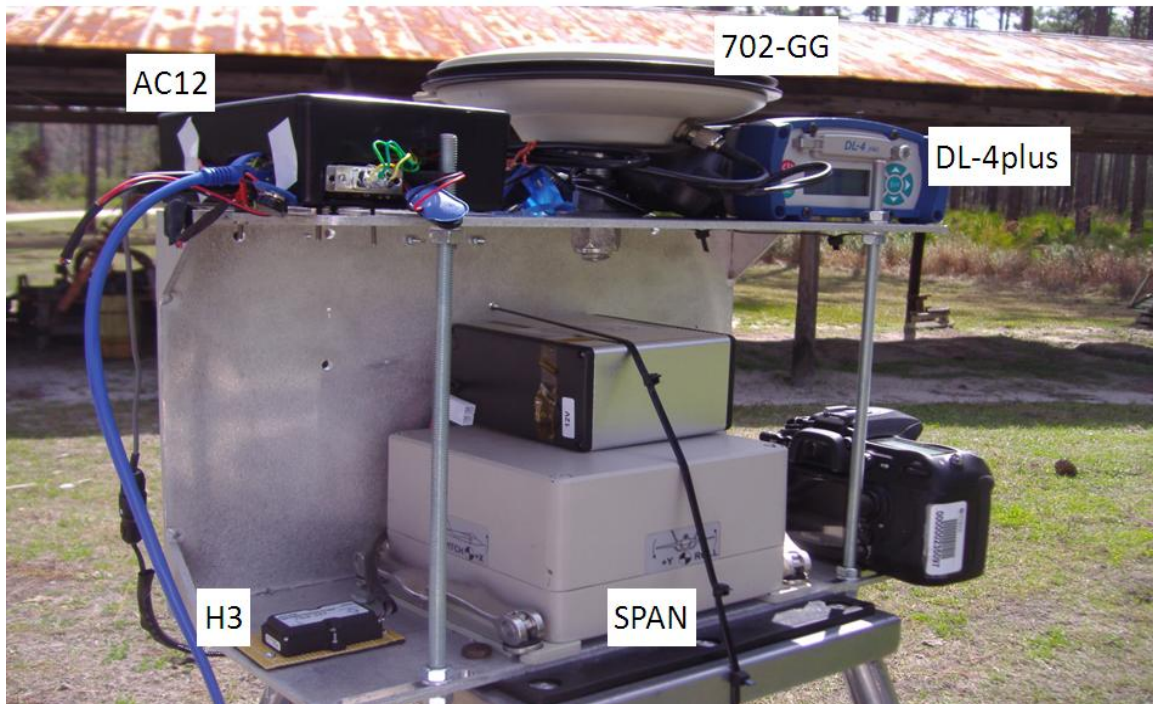


Figure 3-5. Georeferencing system components for GatorMMSv2.0 (image courtesy of author)

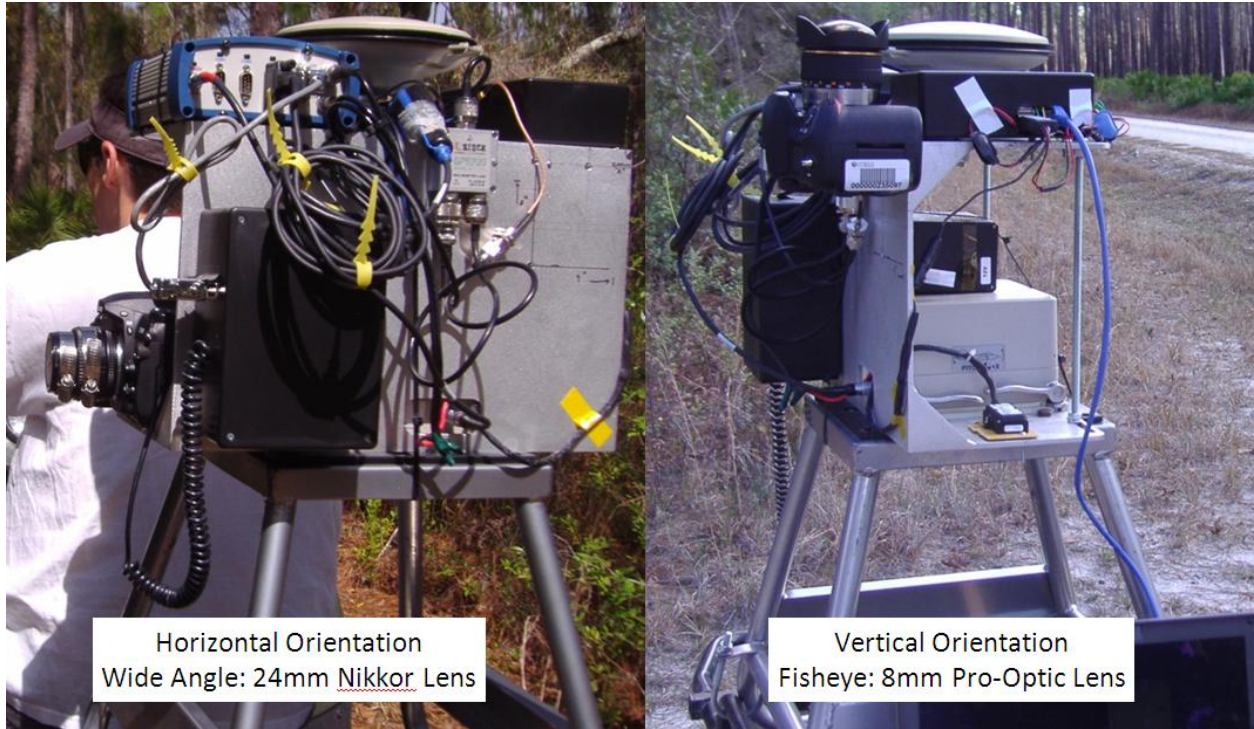


Figure 3-6. Imaging system lenses for GatorMMSv2.0. The hose clamps affixed to each lens set the focus at infinity. This was important for maintaining consistency in the data from calibration through data acquisition. (images courtesy of author)

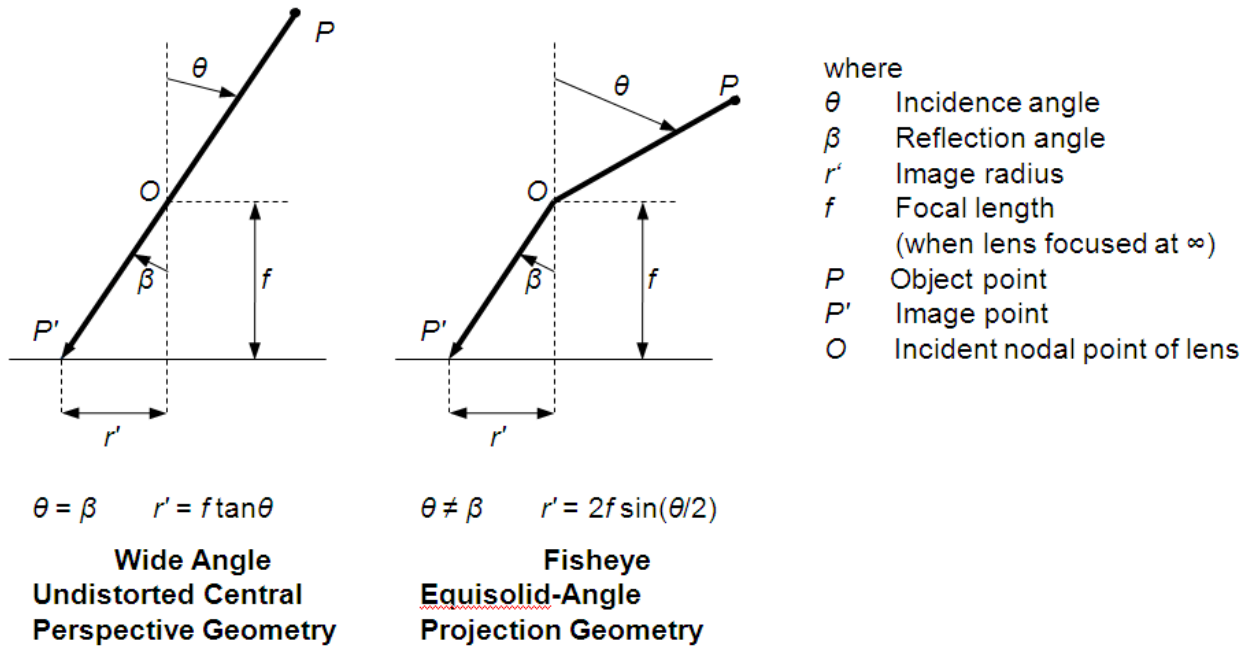


Figure 3-7. Lens geometry comparison: wide angle vs. fisheye (modified after Schneider, D., E. Schwalbe, and H. G. Maas. 2009. Validation of geometric models for fisheye lenses. *ISPRS Journal of Photogrammetry and Remote Sensing*. 64 (3): 259–266).

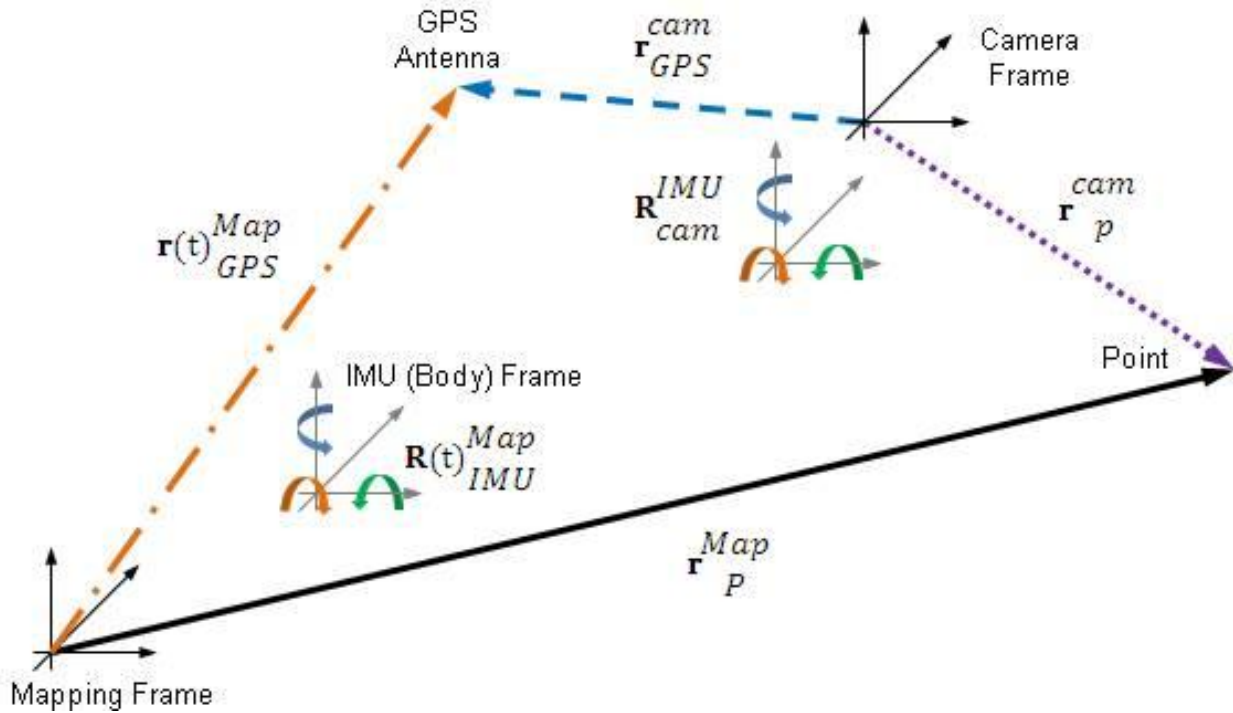


Figure 3-8. Physical relationship between GatorMMS sensors including the IMU, the GPS ARP, and the D200 camera (modified after Ellum, C.M. and N. El-Sheimy. 2002. The Calibration of Image-Based Mobile Mapping Systems. In *Proceedings of the 2nd Symposium on Geodesy for Geotechnical and Structural Engineering*. Berlin, Germany: The International Association of Geodesy (IAG)).

CHAPTER 4 GEOREFERENCING SYSTEM TESTING

4.1 Study Site – Austin Cary Memorial Forest

Austin Cary Memorial Forest (ACMF) is a 2043 acre southern pine flatwoods forest administered under the direction of the School of Forest Resources and Conservation at the University of Florida (Muller and Maehr 2000; Powell et al. 2005). The forest serves three primary purposes: resident/community/student education, extension and demonstration, and research. This managed forest has a multitude of roads and fire trails which served as an excellent location for testing the georeferencing system, GatorMMS v1.0. Figure 4-1 shows a map of the location of the forest in relation to downtown Gainesville in North Central Florida.

The goal of the GatorMMSv1.0 testing was to gain experience in the field with different GPS/INS acquisition methods and investigate various processing schemes with Waypoint® Inertial Explorer™ 8.10 (WIE). The subsequent analysis provided a template for the processing and data collection schemes with GatorMMSv2.0.

4.2 Data Acquisition

On March 26, 2010, the SUR6535 GPS/INS Integration class collected inertial navigation data using GatorMMSv1.0 at ACMF. After strapping the Novatel® GPS-aided INS to the ATV, the class members traversed through the forest on primary and secondary roads that may have been inaccessible via conventional automobile. In the summer of 2009, ground control points (GCPs) were installed along these roadways (Figure 4-2). Static GPS sessions were performed to establish coordinates for these GCPs through a GPS network adjustment using the Gainesville (GNVL) Continuously

Operating Reference Station (CORS) as the master control point. GNVL is located at the Gainesville Regional Airport approximately 8km from ACMF.

During the test runs, the ATV was stopped on a number of the GCPs to perform a static observation. The ATV was backed down over the point by centering the GPS antenna as close as possible to the GCP. The static sessions served a two-fold purpose for the post-processing of the data. First, Zero Velocity Updates (ZUPTs) would be used to bound the propagation of error in position, velocity, and attitude. Furthermore, Coordinate Updates (CUPTs) could be introduced into the processing filter to aid in the navigation solution computation. This CUPT trajectory served as a check for the navigation solution versus the non-CUPT trajectory. Fifteen static observations were made on fourteen of the twenty GCPs (one GCP was observed twice).

Before traversing the forest, INS initialization was necessary. In strap-down systems, this process is called analytical gyrocompassing. While the vehicle is stationary, sensor measurements are recorded so the initial attitude of the system can be resolved. It is advisable that stationary initialization be performed at the beginning and end of each session for two reasons. With good satellite visibility, ambiguity resolution (AR) of stationary GPS data is easier than AR on kinematic GPS data. Second, the end of session stationary period enables the processing software to perform a backwards filtering operation with greater precision since the end attitude alignment is more easily resolved.

Two traverse loops were performed by the class members: Loop West and Loop East (Figure 4-3). The origin for both loops was in the vicinity of GCP 1 near the ACMF offices. Before processing the inertial navigation data, the GPS-only solution needed to

be computed using GNVL as the master control station. This Global Navigation Satellite Systems (GNSS) solution provides the initial position for the INS-free navigation and the position updates for the GPS-aided INS navigation.

4.3 GPS/GNSS Processing in the Forest

For the initial GPS processing, the Kinematic Ambiguity Resolution (KAR) method was implemented using the WIE software. The WIE Help Manual recommends using KAR for periods of extremely poor geometry or loss of lock (Inertial Explorer™ 2008). Both are scenarios encountered in a forest environment with a multitude of satellite obstructions from the tree canopy. Figure 4-4 is a plot of the available GPS satellites during the observation period. The solid lines indicate satellite availability for the given geographic position where colors correspond to different elevations and the red bars indicate a loss of lock or no observability by the Novatel® GPS receiver. The forest canopy provided plenty of GPS signal outages. Figure 4-5 is a plot showing the ambiguity resolution status of the KAR processing. At most, one baseline solution was fixed with a high number of outages or float solutions. Redundant fixed ambiguity baselines are imperative for optimal determination of observation location.

Figure 4-6 shows the resultant KAR processing solution using WIE's defaults (automatic forward and reverse processing, loose DOP standards, etc.). The bright green areas have the highest quality solutions (Q1) while the bright red areas have the lowest quality solution (Q6). Unfortunately, areas with solutions are few and far between considering the length of the entire trajectory. Thus before proceeding with the inertial data processing, a better GPS solution was sought.

The Advanced Real-Time Kinematic (ARTK) WIE GNSS processing profile was used next. Given the results in Figure 4-7 and Figure 4-8, the ARTK profile provided a

much better position solution (more solutions along trajectory including more Q1 solutions) due to a higher number of fixed ambiguity baselines (teal bars in Figure 4-8). Having this improved GPS solution trajectory means more frequent and more reliable position updates in the inertial processing for the GPS-aided inertial navigation. Also, greater confidence can now be placed on the initial position coordinates used in the INS-free navigation processing.

4.4 INS-Free Navigation

When performing IMU-only processing, the default for WIE is to choose the first epoch for initial position. Unfortunately, this means that the estimated initial velocity and position standard deviations will be quite large. Since the initial error propagates throughout the entire trajectory bounded only by the Schuler oscillation in the horizontal channels and unbounded in the vertical channel, the optimal initial value will be derived from an initialization epoch with the highest precision (smallest standard deviations). For this field work, the original default epoch was the 400820th second of the GPS Week while the optimal epoch was the 400980th second of the GPS Week. The optimal epoch had standard deviations about one half of the original epoch standard deviations for velocity in the horizontal and vertical channels. It is apparent from Figure 4-9 that even with the optimal initial position, the gyroscope drift and misalignment makes the navigation trajectory completely unreliable. The amount by which the position drifts is remarkable in the two hour data acquisition session (Note the scale: each box is 100km by 100km).

Furthermore, the WIE IMU-only processing determines ZUPTs automatically. Thus, the bounding of the errors in the horizontal channels is not seen in Figure 4-10. When updates occur, the Schuler oscillation is broken. Furthermore, the estimated

precision of the position in Figure 4-11 confirms what the reader already intuitively knows: the INS-free navigation trajectory is not reliable.

While position updates from the previously determined GNSS solution create a drastic improvement in the trajectory, the author tested an IMU-only solution that included both ZUPTs and CUPTs. Table 4-1 has a complete list of the ZUPTs and CUPTS used. The start and end times for the ZUPTS were determined by using the field notes to estimate the time at each point and interpolating the beginning and end times from the velocity profile of the INS-free navigation solution. The GCP coordinates for the CUPTS were provided by the instructor from previous processing of the GCP static observation sessions. The projected coordinates are in UTM 17N WGS84.

While the solution as seen in Figure 4-12 is not usable as a navigation trajectory, analysis of the errors in Figure 4-13 and Figure 4-14 shows the effect that the updates have on the propagation of errors in the navigation solution. The velocity accuracy plot show the errors propagating until a ZUPT is processed. At which point, the error 'resets' and drifts again until the next ZUPT. Likewise, the CUPTS perform the same function in the positional accuracy plot. The CUPTS contribute to the spider-web-like effect of the navigation trajectory plot as seen in Figure 4-12.

Even with a tactical-grade IMU such as the SPAN™ system (1°/hr), the inertial data and infrequent updates are not sufficient enough to provide a usable navigation trajectory. Thus, the development of GPS-aided inertial navigation is necessary at this point. This complimentary pair of navigation systems works so well because the errors are highly non-correlated. The dominant GPS error is short-term white noise (errors occur on an epoch by epoch basis) while the dominant INS error is long-term drift error

(as already seen in IMU-only navigation). Thus, the extremely precise INS system is best suited for filling in short gaps in the GPS determined navigation trajectory. Through the following analysis of GPS-aided inertial navigation, improvements in the navigation trajectory are quite prevalent.

4.5 GPS-Aided INS-Navigation

There were three primary objectives in exploration of GPS-aided inertial navigation (GAIN). First, a brief comparison of forward-only processing versus combined backward and forward processing was sought. The second objective was comparison of the GAIN solution of the GCPs with the known GCP coordinates. The GAIN trajectory positions from the ZUPT intervals were averaged and compared to the known coordinates. Third, the author sought to compare GPS/INS integration techniques to compare their respective trajectories. Specifically, loosely coupled and tightly coupled integration approaches were compared.

As discussed in Chapter 3, the simplest closed loop GPS/INS integration approach is loosely coupled (LC) integration. With LC integration, the GPS position and velocity are computed in a separate filter before being integrated with the INS navigation states. A common but more complex integration technique is the tightly coupled (TC) integration approach. Instead of integrating a previously computed GPS position and velocity into the GPS/INS integration filter, satellite phase ranges and range rates are integrated. The advantage to this is the ability of the filter to use less than the LC required four satellite ranges. Thus, all measurements can be used in the TC integration approach which should help the overall accuracy of the TC navigation trajectory.

During WIE processing, the user has the choice of using a forward-only, a backward-only, or a combined (backward & forward) solution. This means the

integration techniques described above are run using the initial epoch (forward) or, alternatively, the final epoch in the data set becomes the first epoch (backward). The combined solution uses a filtering technique (Kalman Filter, EKF, etc) to combine the forward and backward solution. If further filtering of the navigation trajectory is desired, then a Rauch-Tung-Striebel (RTS) smoothing algorithm can be implemented. After all WIE processing, the RTS combined solution will be considered the final GAIN trajectory for each integration technique.

4.5.1 Loosely Coupled GPS/INS Integration

When performing filtering in one direction (i.e. forward-only) after long periods of GPS position outages, the GAIN trajectory will drift. Recall the central problem with INS navigation is the long term drift error when no GPS position updates are available. In the Figure 4-15, trajectory drift in one-directional processing is visible along the eastern edge of the eastern loop as the loop merges with the western loop and where the western loop returns to the origin. Recall the red portions of the trajectory are the Q6 positions. Thus, the longer the ATV went without receiving adequate GPS signals from at least four satellites, the INS error propagated. When the backwards LC integration technique was implemented, the drift was visible on the opposite ends of the GPS position/velocity update outages. When the two solutions were combined via filtering, the resultant GAIN trajectory in Figure 4-16 had no significant drifting. Thus, it is imperative that a combined approach be taken with GAIN trajectory determination. For further emphasis regarding the gains in a combined solution, Figure 4-17 and Figure 4-18 show the positional accuracy for the forward-only processing solution was approximately three times worse than the combined solution. Similarly, the velocity

accuracy for the forward-only processing solution in Figure 4-19 was approximately two times worse than the combined solution in Figure 4-20.

This discussion focused on a comparison of intermediate steps in the LC integration approach. The purpose was showing the increases in accuracy that are made in processing beyond the initial forward-only processing. Significant increases in accuracy were also made between the combined filtering and smoothing steps. These comparisons will be discussed in the next integration technique comparison section.

4.5.2 Loosely Coupled Integration and Tightly Coupled Integration Comparison

Using the GatorMMSv1.0 data, a comparison of GPS/INS integration techniques was undertaken. Figure 4-21 and Figure 4-22 show the resultant combined and smoothed LC and TC trajectories, respectively. The solutions seem fairly similar with subtle differences in the quality of the rendered trajectories (i.e. the hook off the eastern loop, the northeast straightaway on the eastern loop, etc.). Furthermore, the positional accuracy plots as see in Figure 4-23 and Figure 4-24 are almost identical. The maximum peaks on the TC positional accuracy plot had peaks that were slightly lower than the maximum peaks on the LC positional accuracy plot. Intuitively, this makes sense as the receiver in these poor positional accuracy areas most likely was receiving signals from less than 4 satellites. The satellite ranges were used in the computation of the GPS-aided INS positions but the estimated precision of these positions was only slightly better than having no complete (at least 4 satellites) position in the LC integration model. Similar results between the 2 techniques were found in the velocity error plots which have not been included.

A more empirical navigation trajectory comparison was necessary to determine the similarity between the two GPS/INS navigation trajectories. Both trajectories were

output from WIE in geographic coordinates (latitude/longitude – WGS84) and projected grid coordinates (UTM, Zone 17N – WGS84). The difference between the TC integration approach and the LC integration approach formed the basis of the quantitative analysis using root mean square error (RMSE) calculations. In this analysis, the 'error' in RMSE refers to the discrepancy between the two approaches. Since coordinate differences are easier to grasp in meters rather than arcseconds, the UTM projected coordinates were used as the basis for comparison. From Table 4-2, the RMSE calculations of the 7964 shared observations show the discrepancy in the northern coordinates was 50% greater than the discrepancy in the eastern coordinates. The RMSE in the vertical channel was slightly greater than the northern coordinate RMSE. Horizontally, the two trajectories were within 1ft (~0.3m) of each other. Three-dimensionally, the discrepancy was less than a foot and a half (~0.4m). From Figure 4-25 and Figure 4-26, the coordinate differences between the two GAIN trajectories were never larger than 2.5m in any channel. Thus, it is reasonable to conclude that these two GPS/INS integration approaches achieved consistently similar results with the implementation of filtering and smoothing algorithms.

4.5.3 GPS-Aided Inertial Navigation Trajectory – Absolute Accuracy Analysis

After establishing relative accuracy between the two integration approaches, an analysis of absolute accuracy was necessary. This process was accomplished through averaging position coordinates during the ZUPT intervals and comparing these to the known GCP coordinates. The GCP coordinates are from previous static observation of the ground control. The author was unable to obtain the original observation data for verification so he relied on the given coordinates. The heights were given in orthometric height. Without knowledge of the geoid used, the author applied a generic geoid

undulation correction to the entire area. The correction of -27.868m was obtained from the National Geodetic Survey's GEOID03 Geodetic Toolkit for the given latitude and longitude of GCP1. In the future, it is suggested that ellipsoidal heights be used for all trajectory comparisons.

From Table 4-3 and Table 4-4, there are four blunders in identifying the ZUPTs (error in the author's interpolation of the velocity profile). More importantly, a systematic error in the data is quite prevalent for the other 11 points. One can call this a bias due to the magnitude of the standard deviations (mm to cm) for the ZUPT session averages relative to the magnitude of the bias (m). The $\pm 3\text{m}$ bias would not be caused by the random centering and misleveling errors caused by inaccurate setup positions. Given the relative accuracy of the LC and TC integration solutions, the most likely cause of the systematic error is a datum shift. After extensive exploration of the given GCP coordinates and ArcGIS files associated with previous work at ACMF, the author was unable to ascertain the source of the datum shift. The author can assert that the coordinate trajectories provided in this analysis were all properly output from WIE in UTM projection 17N – WGS84. Without being able to locate the original observation files used in the processing of the static GCP baseline solutions, the absolute accuracy cannot be definitively answered. Lacking confidence in the known GCP coordinates, further processing with CUPTs was not investigated at this time. However, once the original files are located, a comparison of geographic coordinates is suggested to avoid the software programs (WIE vs. ArcGIS) using different NAD83 to WGS84 datum transformations as well as eliminating potential discrepancies in projections.

4.6 Georeferencing System Testing Lessons Learned

From the georeferencing system testing with GatorMMSv1.0, the following lessons can be used in future GPS-aided inertial navigation analysis with subsequent GatorMMS generations. In WIE, the ARTK profile is better at resolving kinematic integer ambiguity than the default KAR profile for terrestrial based mobile mapping in the forest. Thus, ARTK should be used for future GatorMMS data sets. Furthermore, whether implementing loosely coupled or tightly coupled integration in WIE, output trajectories should always be combined and smoothed for optimal results.

For the current data set, the given GCP coordinates are unreliable due to lack of raw observation files and datum conversion uncertainties. If short baseline observations while mobile mapping are desired, a new GCP network should be established in the project study area. Additionally, the ellipsoidal height should be used for MMS height analysis. This will avoid the need for geoids and orthometric heights.

Numerous issues encountered with the use of zero velocity and coordinate updates can be used as learning tools moving forward. First, GPS-free inertial navigation using ZUPTs is not accurate enough for mobile mapping with a tactical-grade IMU. Second, coordinate updates are difficult to incorporate into the processing accurately due to orientation and misalignment error when driving over the GCPs. Lastly, if zero velocity updates are to be integrated with GPS observations, accurate field records must be maintained for ZUPT intervals to minimize interpolation errors.

Table 4-1. Zero velocity updates and coordinate updates for inertial navigation processing. Column 1 shows the ground control point for each CUPT/ZUPT. Columns 2-4 are the coordinates for each CUPT. Column 5 is the estimated GPS time from the field notes. Columns 6-7 are the interpolated time intervals from the inertial navigation trajectory.

GCP	Easting (m)	Northing (m)	ell. h (m)	GPS Time (s)	GPS Start (s)	GPS End (s)
2	382211.505	3291945.804	21.426	403200	403230	403430
20	381841.110	3291290.946	20.593	403680	403680	403745
5	382071.696	3289614.479	15.142	403860	403820	403880
15	381963.261	3289976.695	19.566	404100	404030	404080
14	382048.035	3289918.497	18.306	404220	404150	404180
13	382216.838	3289900.409	17.987	404340	404250	404305
12	382355.906	3289946.823	17.078	404400	404365	404435
11	382389.884	3290097.208	17.884	404580	404505	404575
10	382400.410	3290285.061	19.029	404700	404660	404695
1	382476.296	3291663.698	21.875	404880	404905	405305
18	382991.968	3292085.940	22.455	405600	405590	405660
17	383910.385	3292751.706	21.543	405840	405850	405920
16	383870.391	3291761.493	19.395	406080	406135	406255
3	383840.367	3291325.734	17.462	406500	406425	406470
1	382476.296	3291663.698	21.875	407400	407380	407730

Table 4-2. Tightly coupled & loosely coupled GPS-aided inertial navigation solution comparison

	DE (m)	DN (m)	DHor (m)	DE ² (m ²)	DN ² (m ²)	DZ (m)	DZ ² (m ²)
Average	0.027	0.009	0.107			0.010	
SD	0.161	0.249	0.278			0.270	
			RMSE	0.163	0.249		0.270
			RMSE_Hor	0.298			
			RMSE_All	0.402			

Table 4-3. Absolute accuracy investigation of loosely coupled integration through comparison of the loosely coupled ZUPT interval average with the CUPT

GCP	DE	DN	Dh	ErrorDist	σ Hor	σ Ver
2	0.699	-2.480	-1.499	2.981	0.093	0.025
20	1.130	-2.065	-1.315	2.696	0.027	0.009
5	294.262	-1322.827	-6.420	1355.177	0.062	0.013
15	1.203	-2.658	-1.540	3.299	0.005	0.010
14	0.912	-2.457	-1.369	2.957	0.014	0.019
13	1.511	-2.338	-2.934	4.044	0.174	0.069
12	0.839	-2.194	-1.558	2.819	0.015	0.025
11	0.532	-2.323	-1.589	2.864	0.011	0.012
10	0.328	-2.332	-1.603	2.849	0.131	0.034
1	0.917	-2.647	-1.460	3.159	0.011	0.024
18	0.852	-2.666	-1.424	3.140	0.009	0.020
17	0.470	-3.463	1.111	3.667	0.012	0.006
16	1395.009	95.153	-3.930	1398.256	0.007	0.011
3	1622.682	397.257	-4.496	1670.608	0.008	0.015
1	-1393.856	193.161	2.512	1407.178	201.459	1.022

Table 4-4. Absolute accuracy investigation of tightly coupled integration through comparison of the tightly coupled ZUPT interval average with the CUPT

GCP	DE	DN	Dh	ErrorDist	σ Hor	σ Ver
2	0.698	-2.479	-1.496	2.979	0.093	0.021
20	1.130	-2.064	-1.312	2.694	0.009	0.021
5	294.262	-1322.827	-6.421	1355.177	0.061	0.013
15	1.216	-2.650	-1.561	3.308	0.004	0.011
14	0.950	-2.472	-1.467	3.027	0.054	0.122
13	1.313	-2.176	-3.508	4.332	0.077	0.065
12	0.856	-2.107	-1.882	2.952	0.067	0.290
11	0.460	-2.312	-1.672	2.890	0.100	0.116
10	0.265	-2.590	-1.059	2.810	0.350	0.342
1	0.917	-2.646	-1.460	3.159	0.011	0.025
18	0.851	-2.666	-1.424	3.140	0.010	0.022
17	0.470	-3.460	1.115	3.665	0.012	0.005
16	1395.010	95.154	-3.930	1398.257	0.007	0.011
3	1364.997	-340.625	-5.888	1406.868	0.008	0.016
1	-1393.833	193.161	2.530	1407.156	201.453	1.042

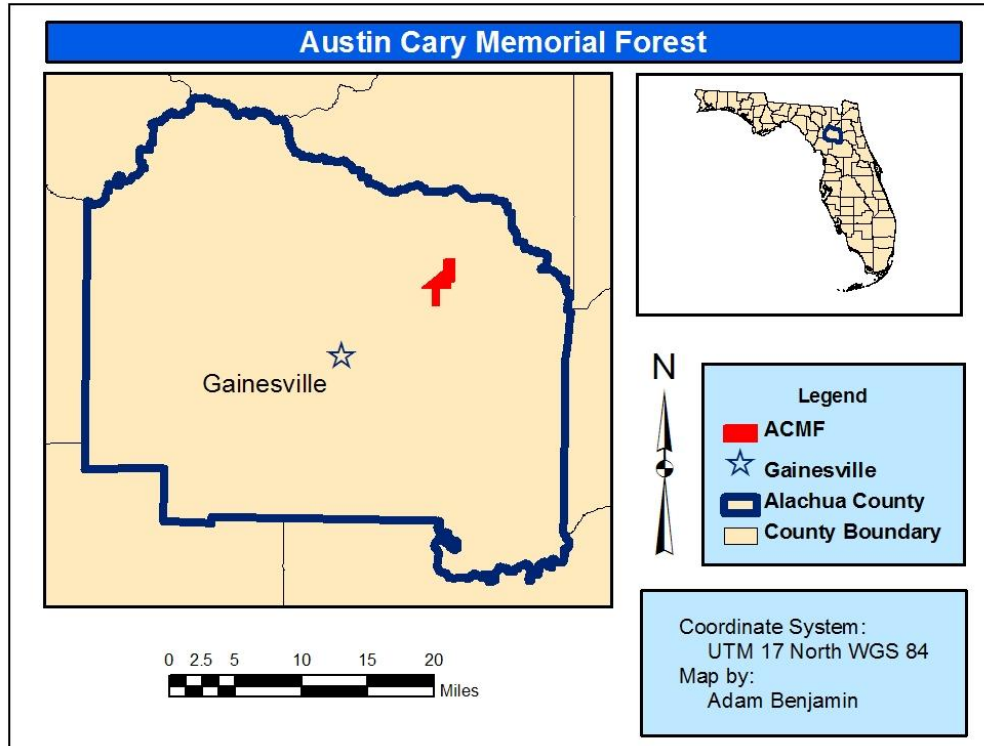


Figure 4-1. Vicinity map of Austin Cary Memorial Forest



Figure 4-2. Static GPS observation of ACMF ground control points. Each GCP is monumented with a 36" rebar reinforcing rod, held in place by an anchor bolt, and flagged with a rigid plastic numbered witness. (image courtesy of author)

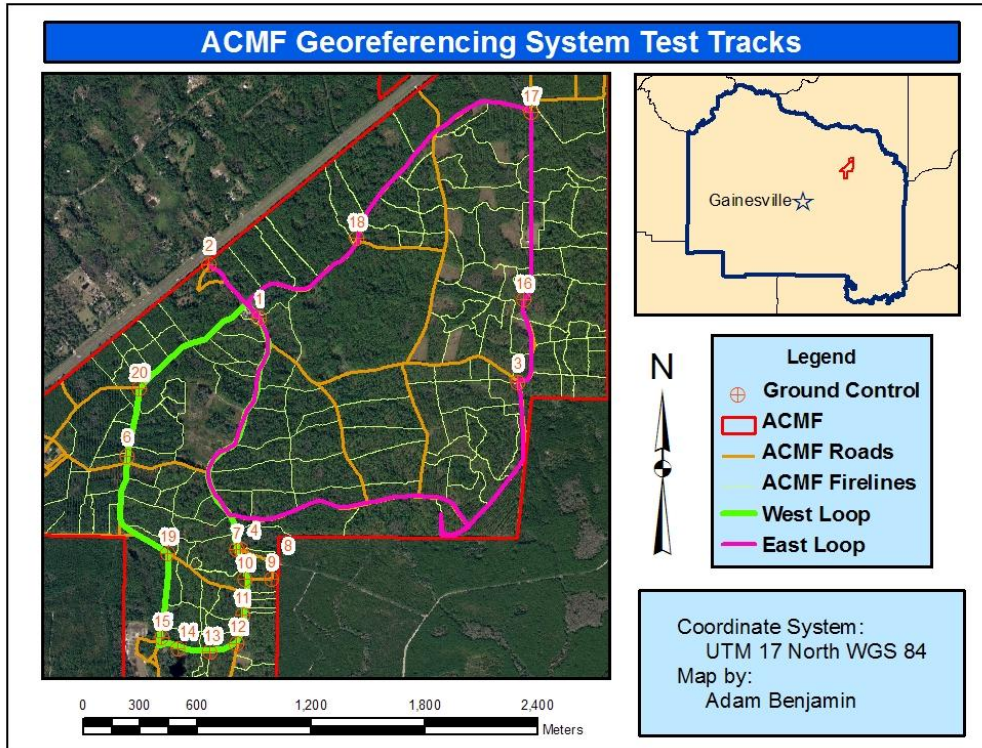


Figure 4-3. GatorMMSv1.0 georeferencing system test tracks in Austin Cary Memorial Forest

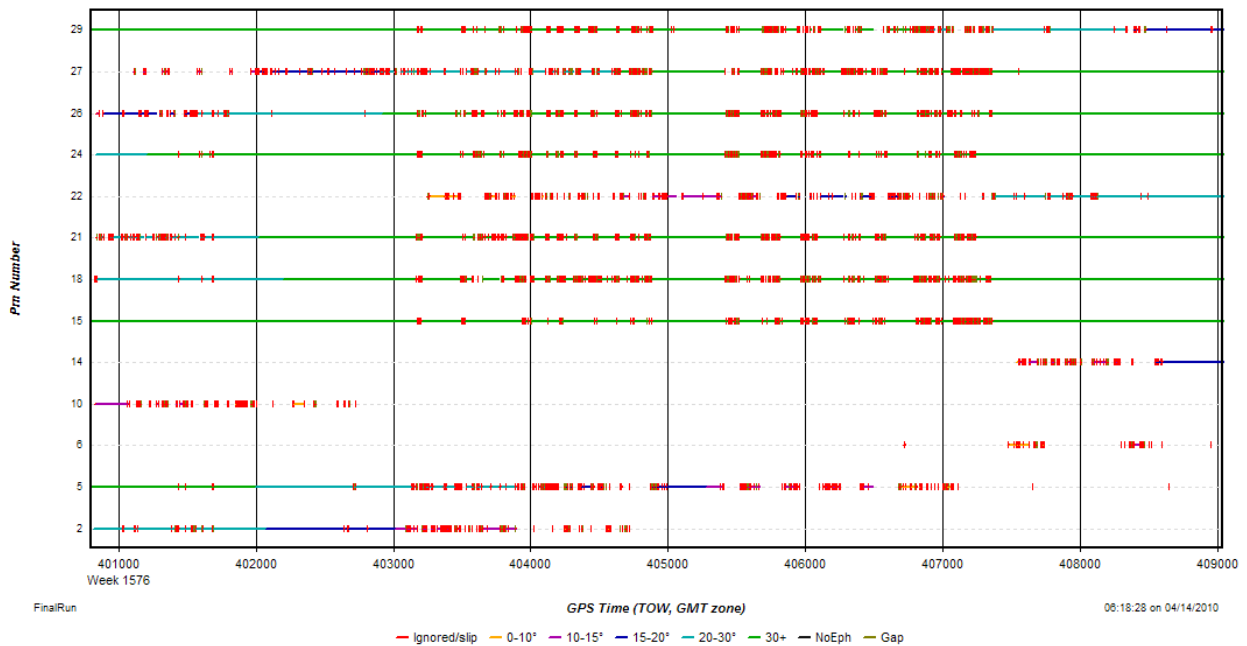


Figure 4-4. GPS satellite status

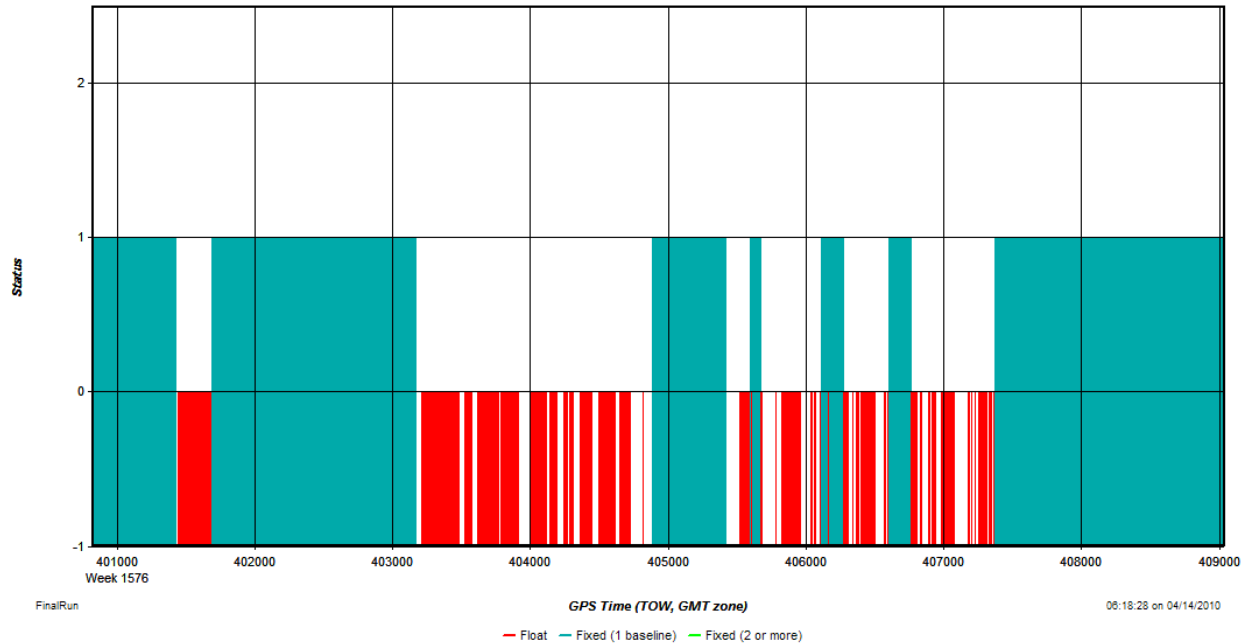


Figure 4-5. GPS baseline status (float vs. fixed ambiguity) – KAR processing.

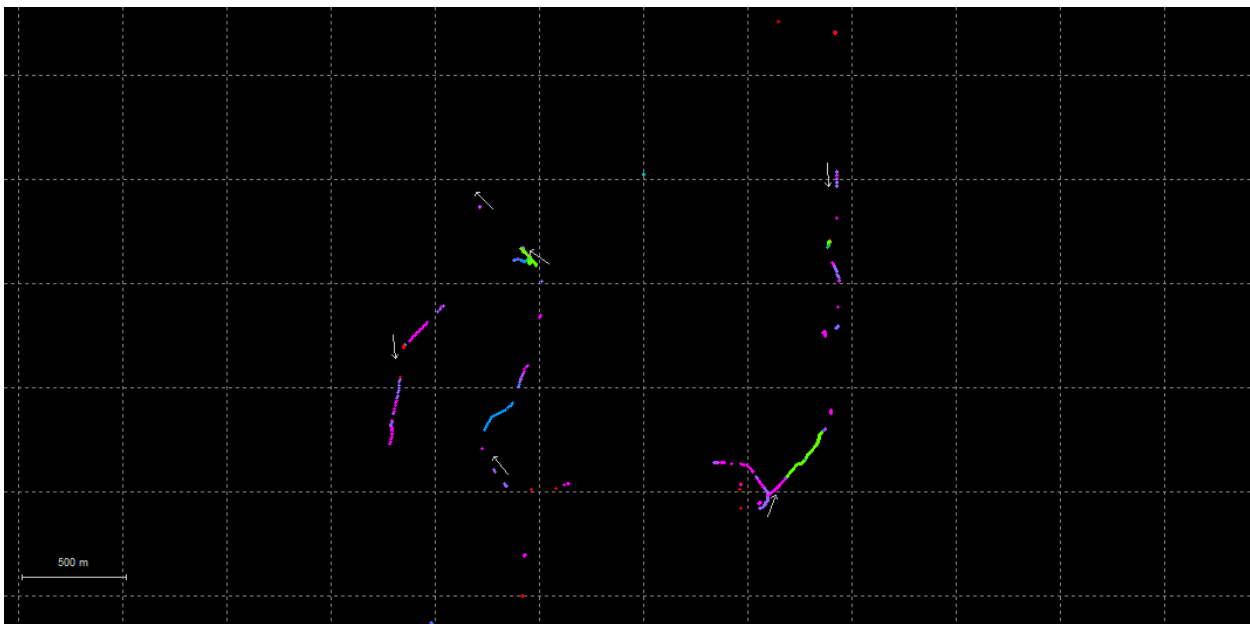


Figure 4-6. GPS solution plot – KAR processing. Note that green is the best quality solution (Q1) and red is the worst quality solution (Q6).

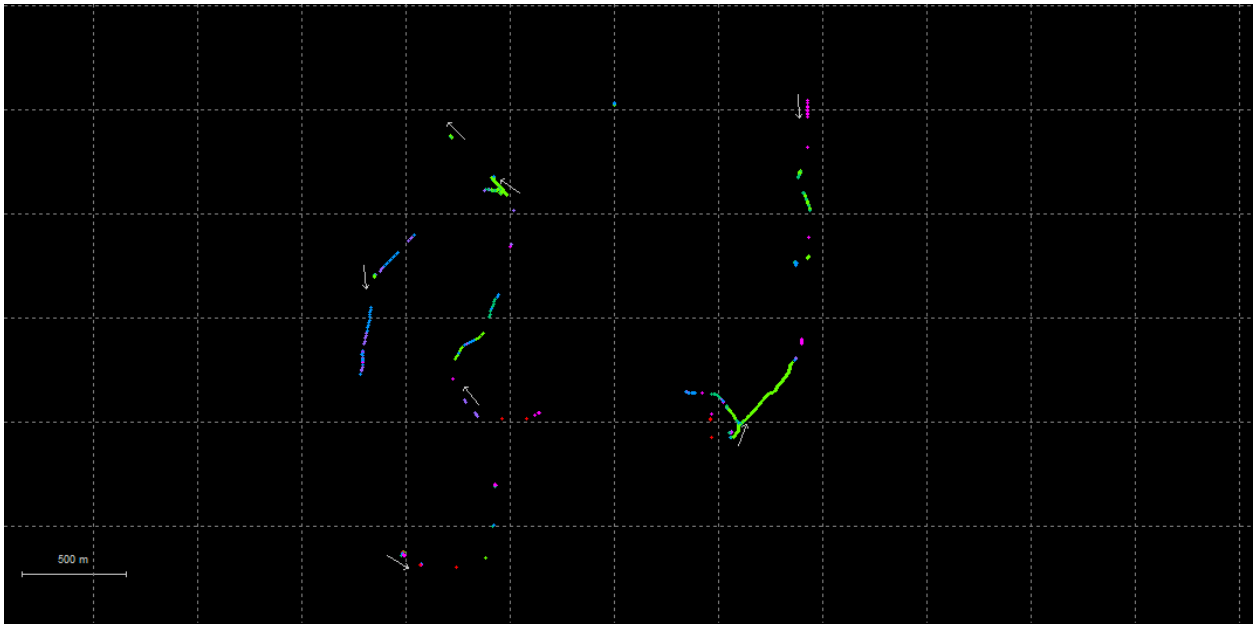


Figure 4-7. GPS solution - ARTK processing

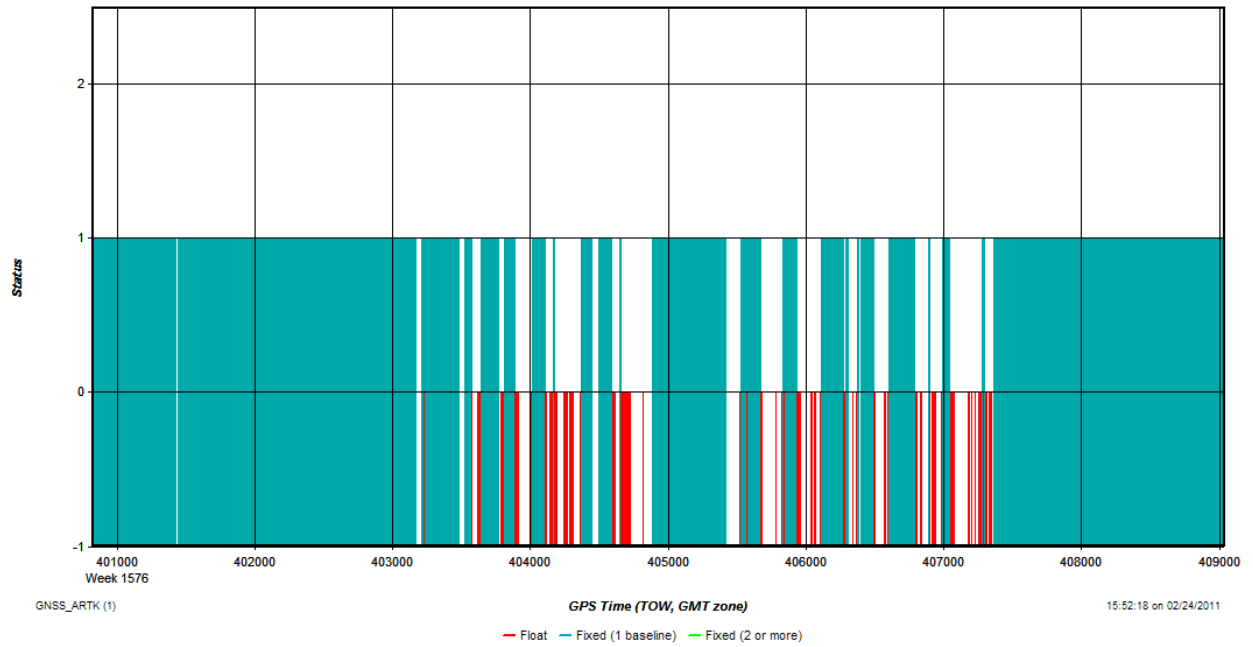


Figure 4-8. GPS baseline status (float vs. fixed ambiguity) - ARTK processing

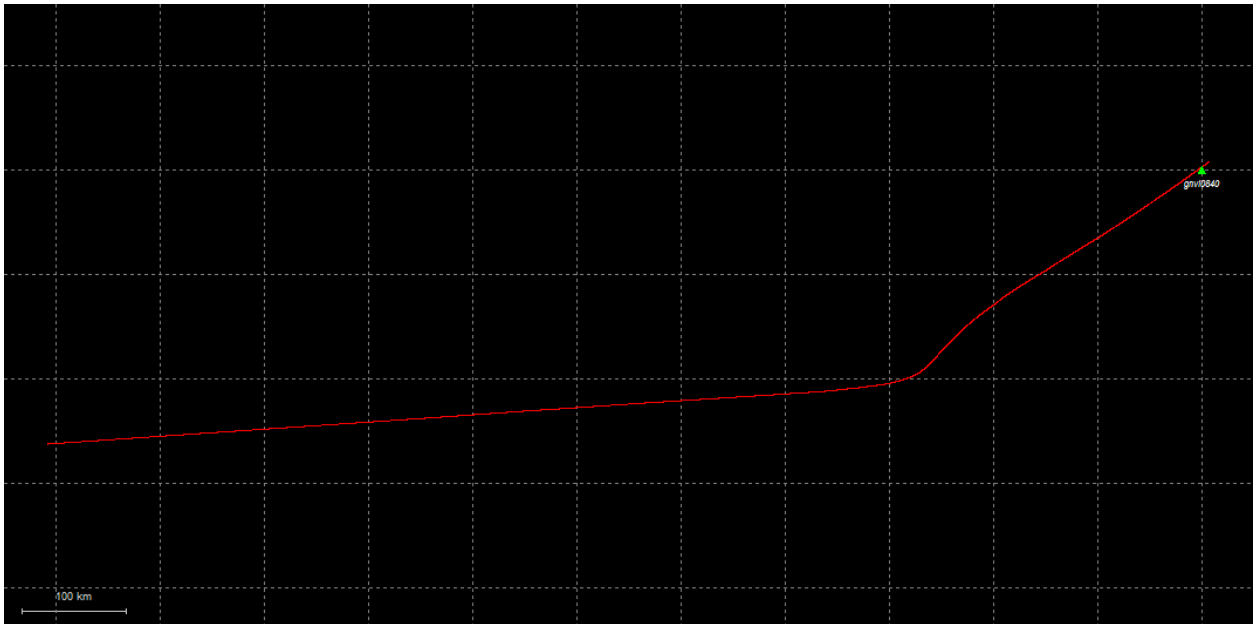


Figure 4-9. IMU-only navigation trajectory

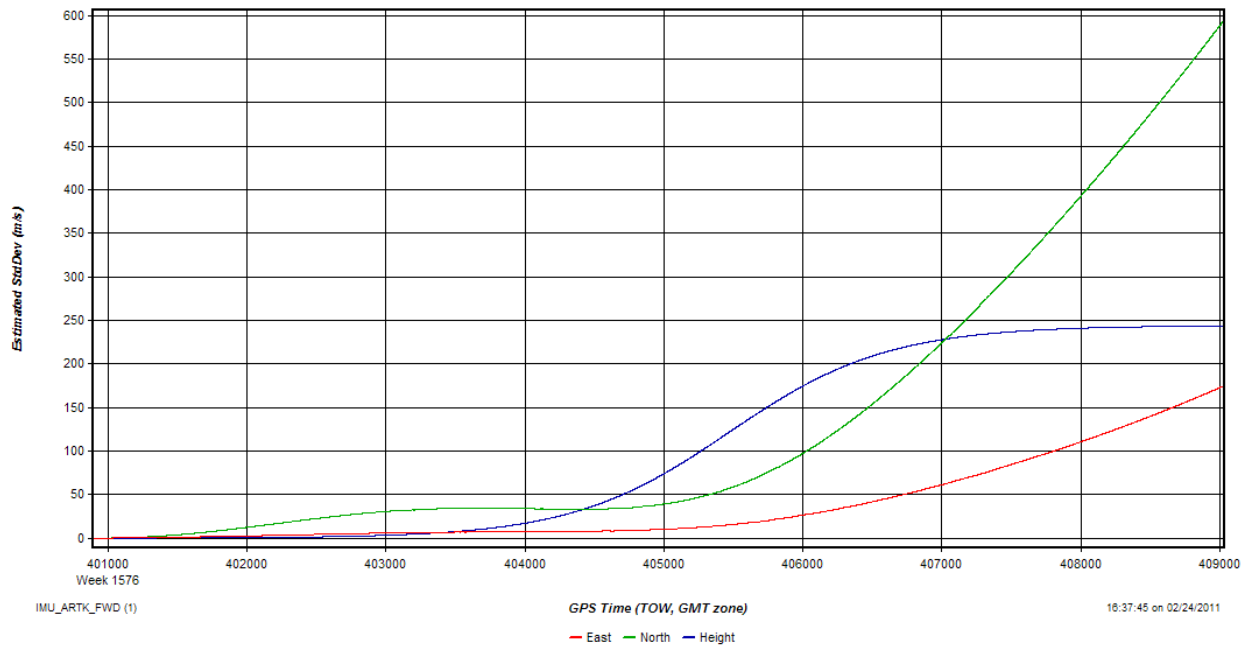


Figure 4-10. INS-free navigation - velocity accuracy plot

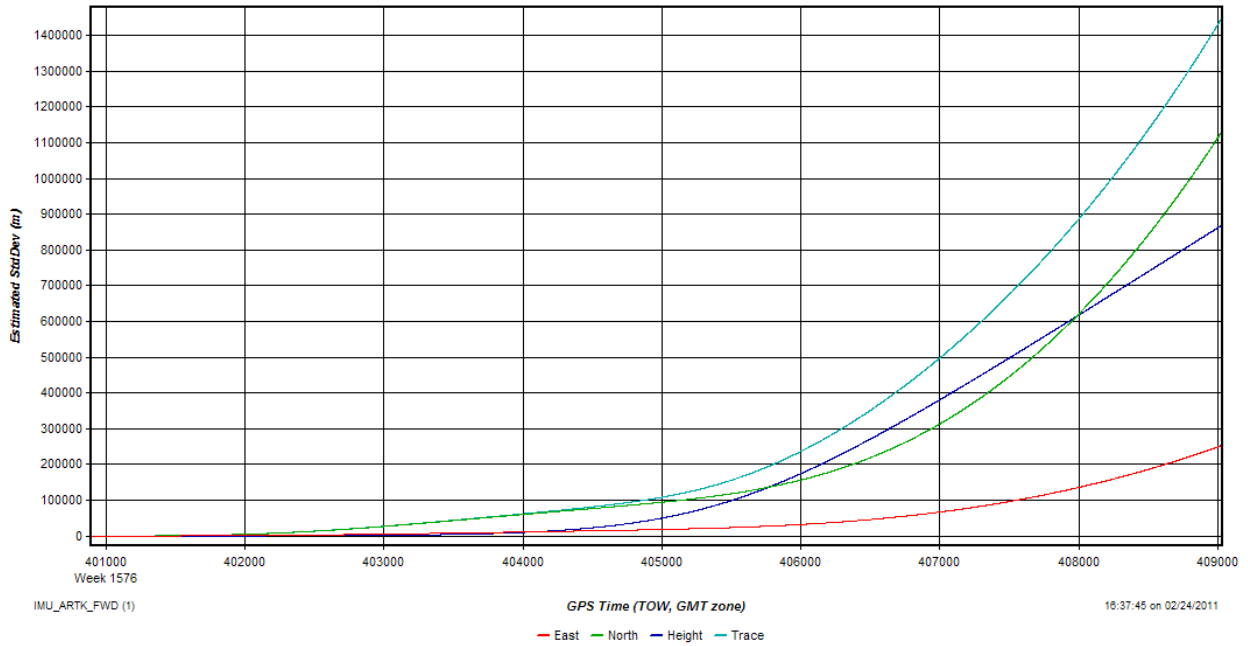


Figure 4-11. INS-free navigation - position accuracy plot

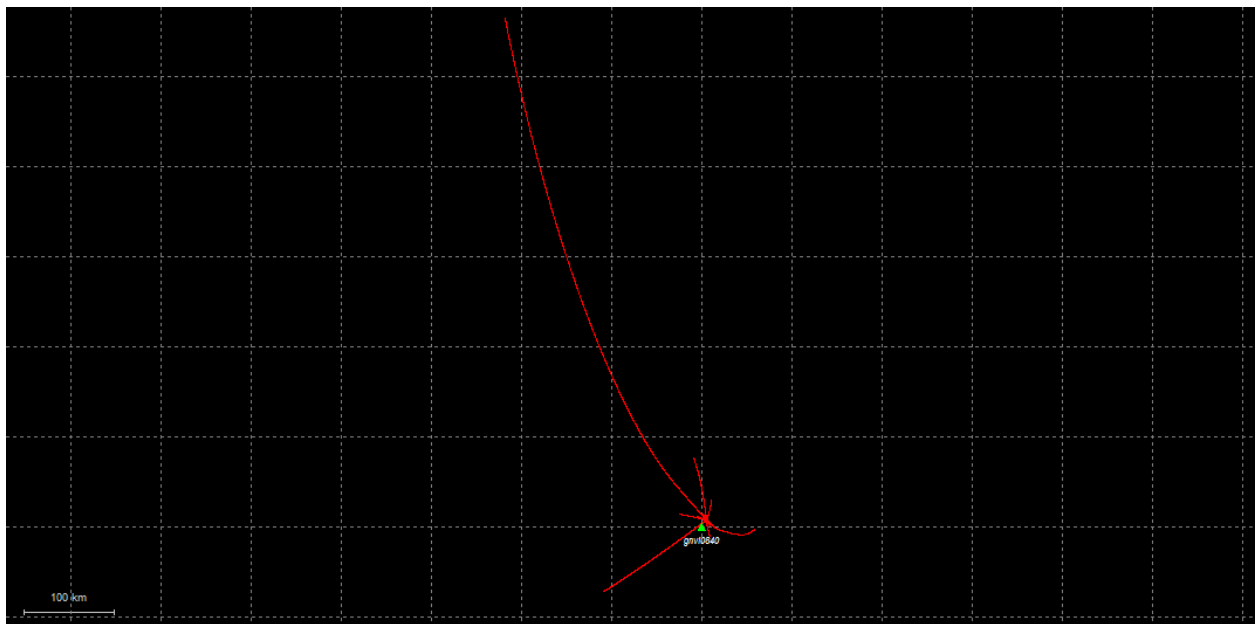


Figure 4-12. INS-free navigation – ZUPTS and CUPTS trajectory

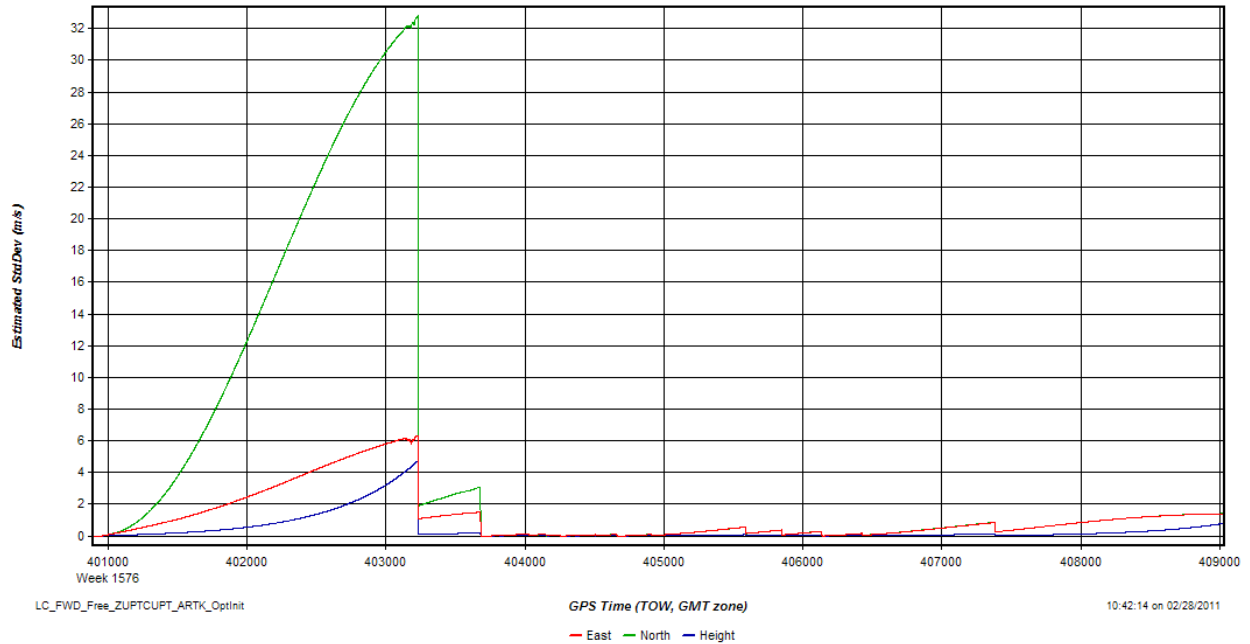


Figure 4-13. INS-free navigation – ZUPTs and CUPTs – velocity accuracy

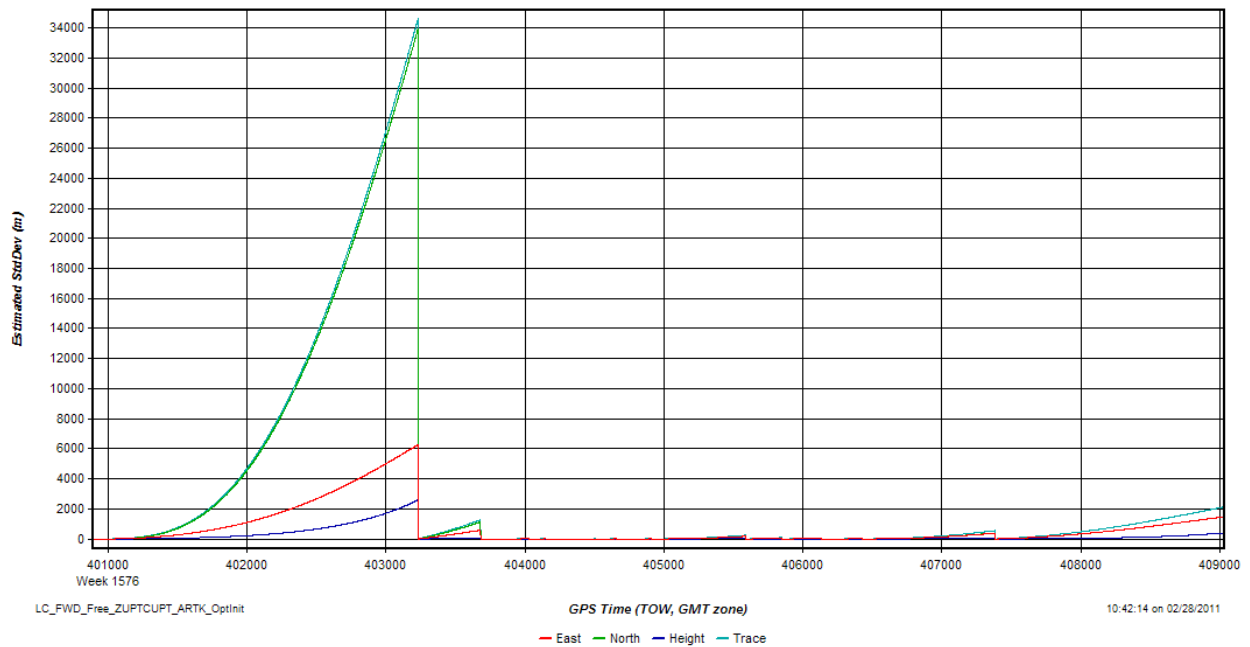


Figure 4-14. INS-free navigation – ZUPTs and CUPTs –positional accuracy



Figure 4-15. GPS-aided INS navigation – forward-only solution



Figure 4-16. GPS-aided INS navigation – combined filtered solution

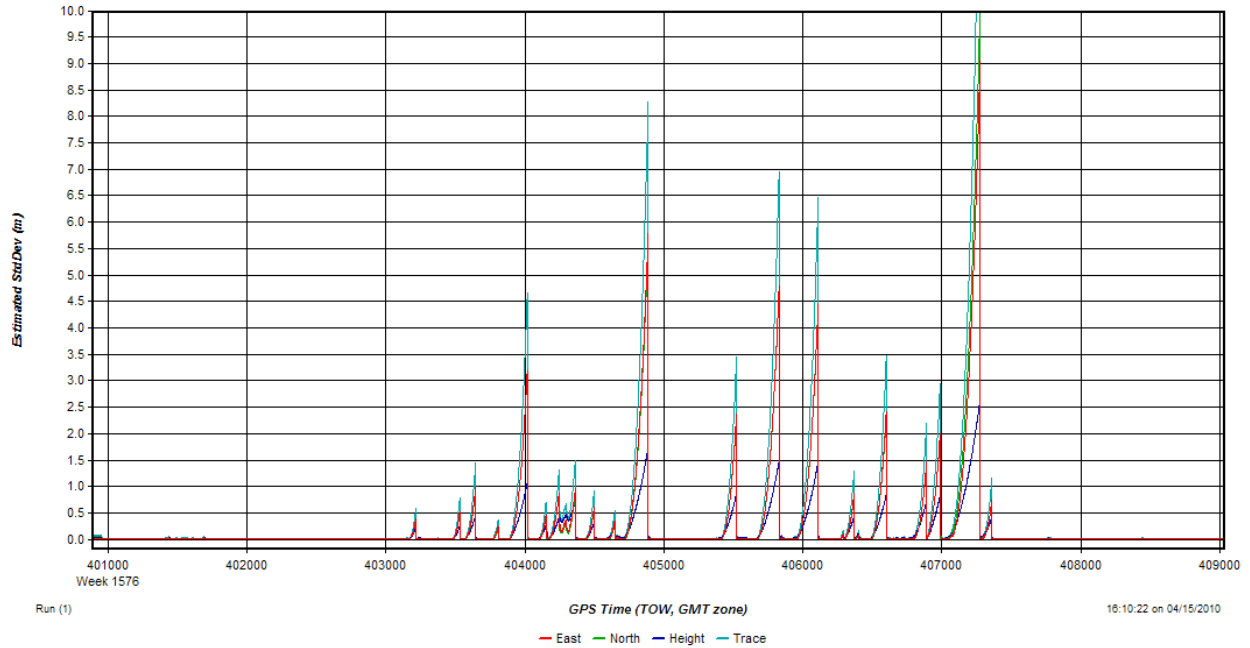


Figure 4-17. GPS-aided INS navigation – forward solution – positional accuracy

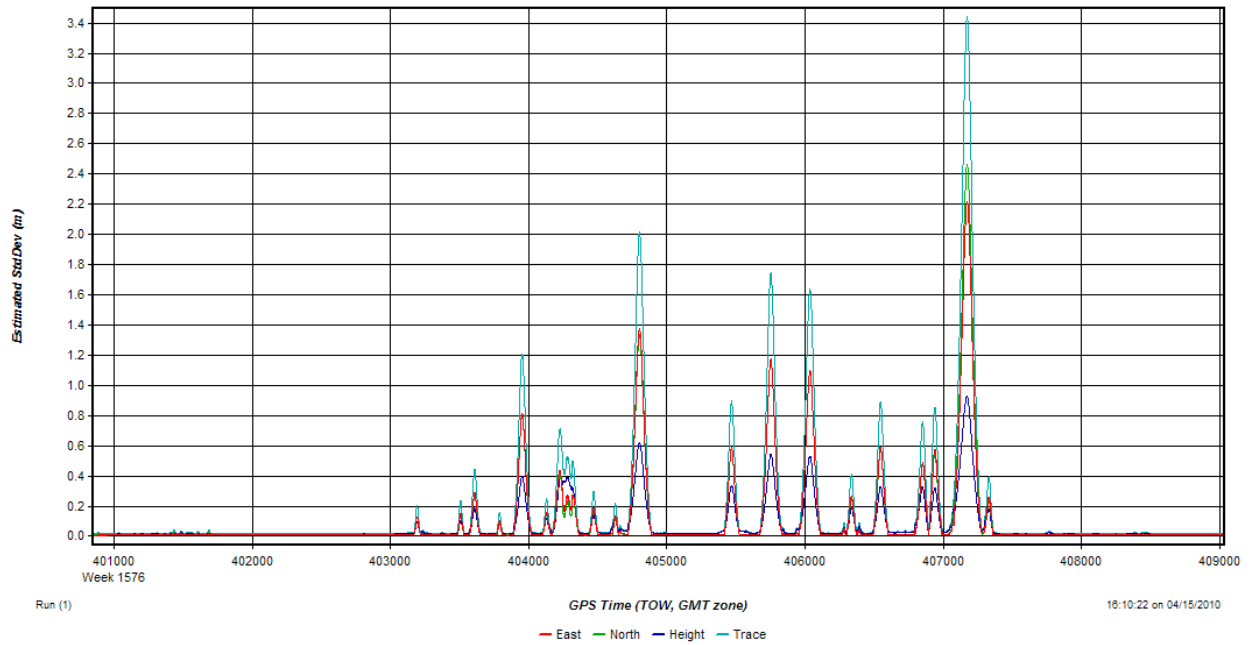


Figure 4-18. GPS-aided INS navigation – combined filtered solution – positional accuracy

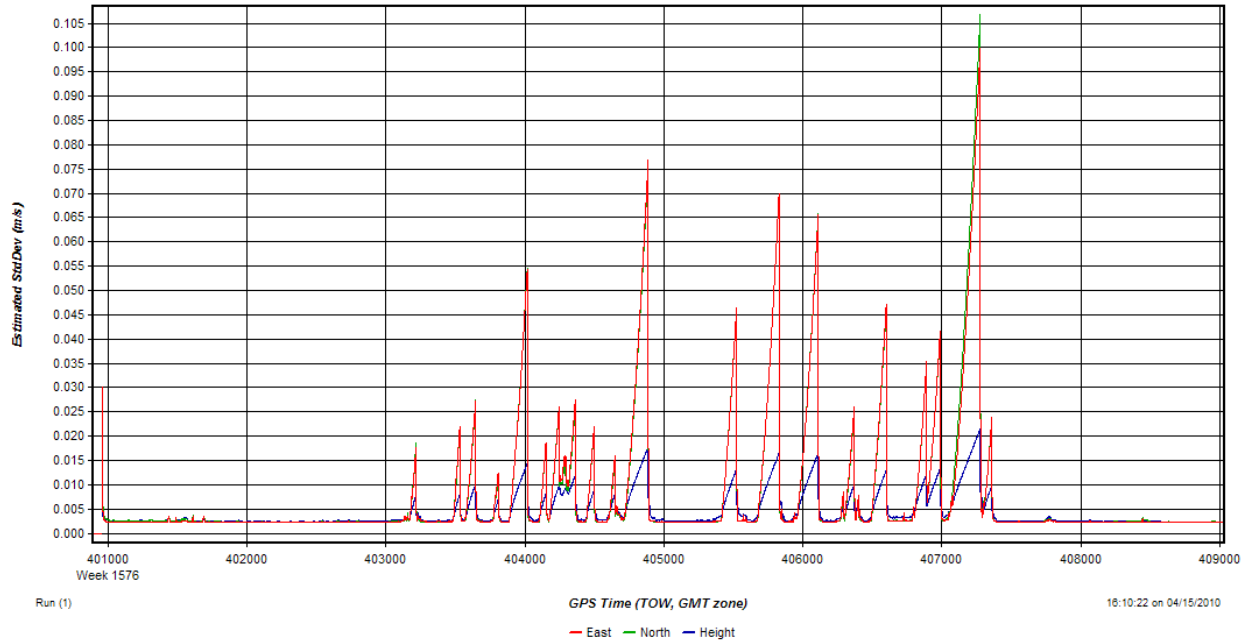


Figure 4-19. GPS-aided INS navigation – forward solution – velocity accuracy

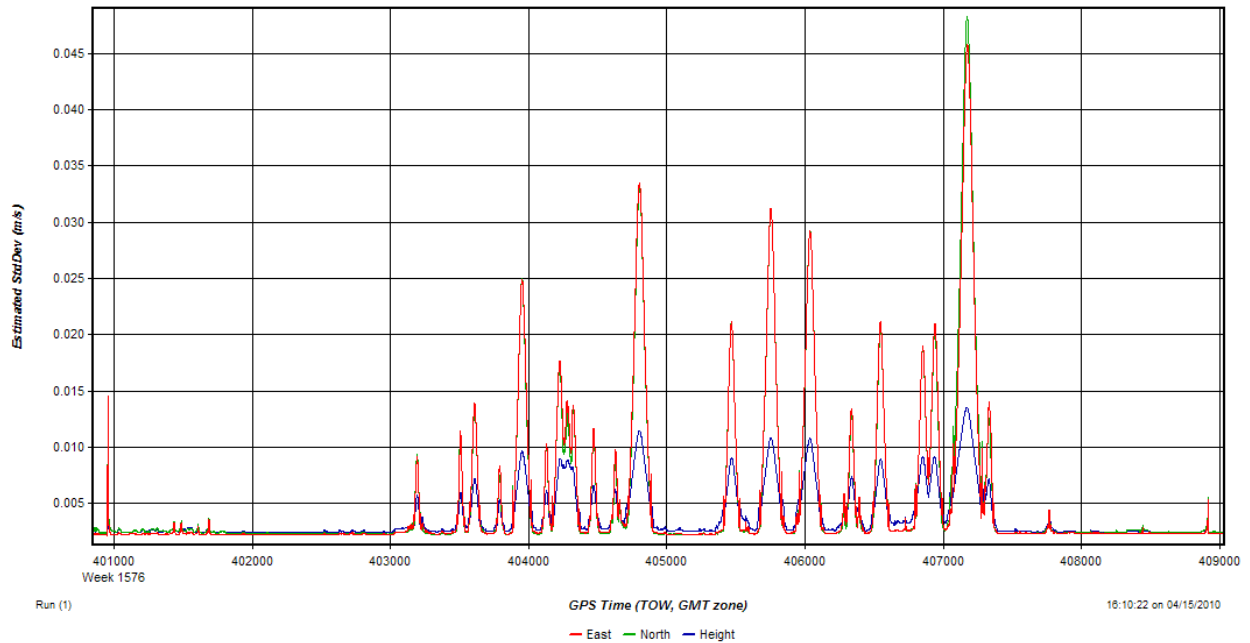


Figure 4-20. GPS-aided INS navigation – combined filtered solution – velocity accuracy



Figure 4-21. GPS-aided INS navigation – loosely coupled combined and smoothed navigation trajectory



Figure 4-22. GPS-aided INS navigation – tightly coupled combined and smoothed navigation trajectory

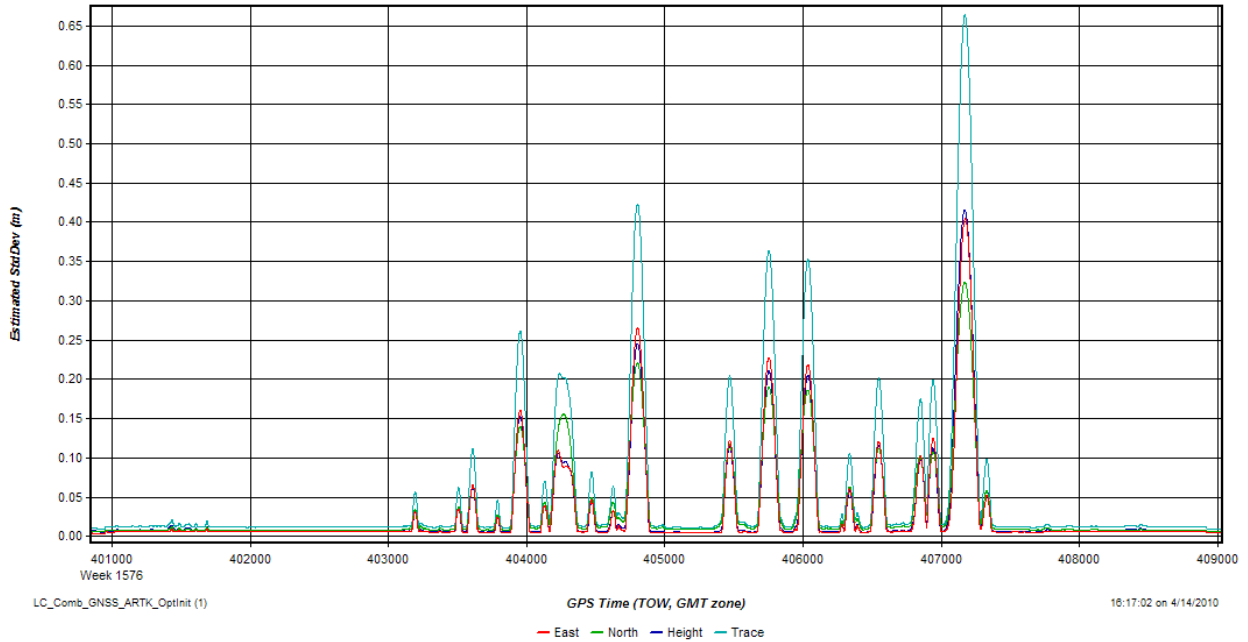


Figure 4-23. GPS-aided INS navigation – loosely coupled combined and smoothed positional accuracy

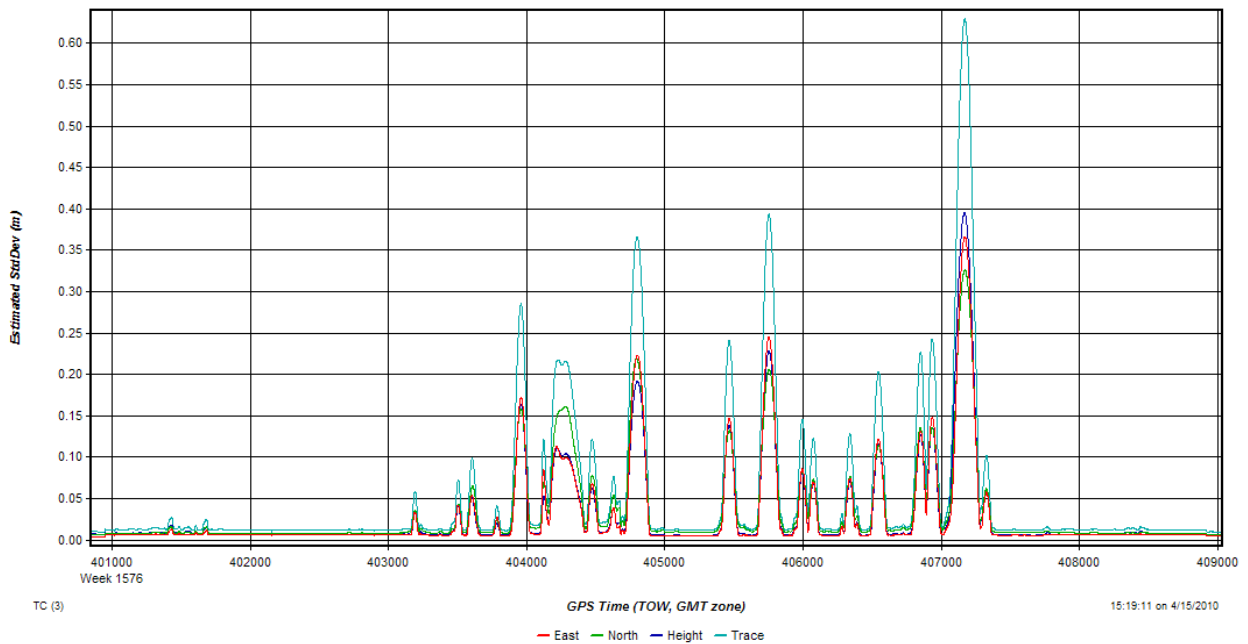


Figure 4-24. GPS-aided INS navigation – tightly coupled combined and smoothed positional accuracy

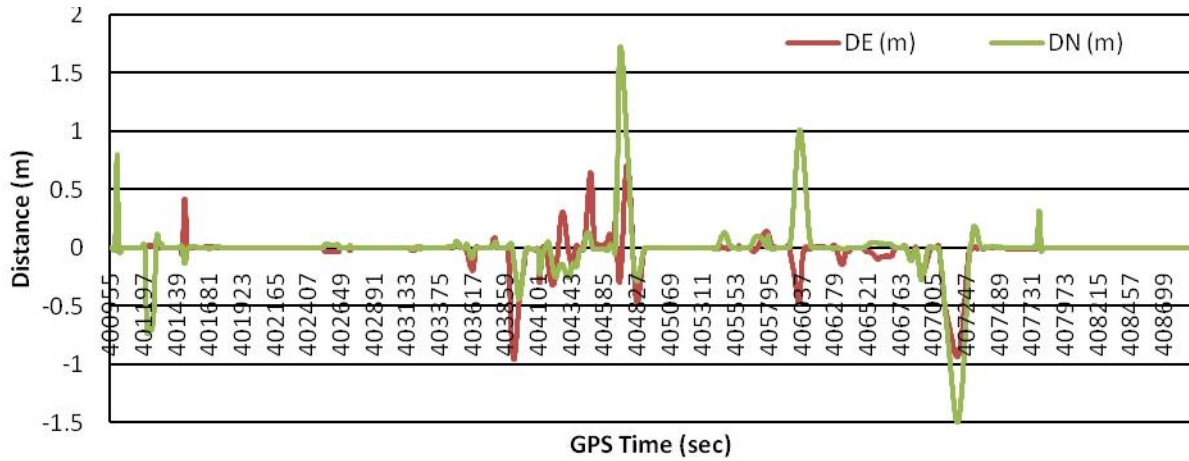


Figure 4-25. Tightly coupled & loosely coupled horizontal GPS-aided inertial navigation trajectory comparison

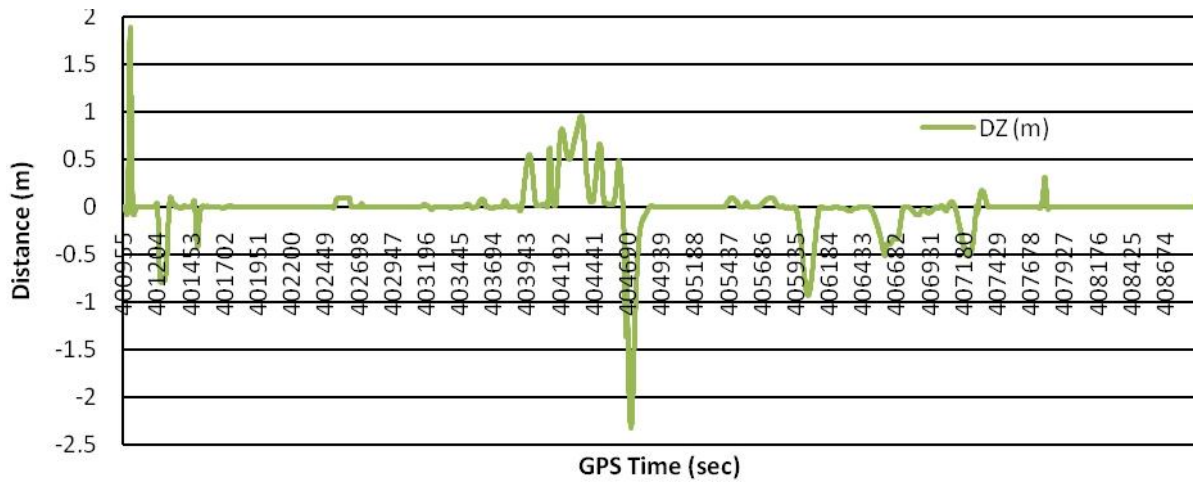


Figure 4-26. Tightly coupled & loosely coupled vertical GPS-aided inertial navigation trajectory comparison

CHAPTER 5
IMAGING SYSTEM TESTING

5.1 Self-Calibrating Bundle Adjustment

Obtaining accurate and precise results from the georeferencing system is only valuable for MMS operation if the imaging system is calibrated. Knowledge of the intrinsic/interior orientation parameters (IOPs) and extrinsic/exterior orientation parameters (EOPs) is imperative for vision-aiding implementation. Results from a self-calibrating bundle adjustment (SCBA) include both the IOPs and EOPs.

The computational process of analytic SCBA is a common photogrammetric process that incorporates the use of augmented collinearity equations. The augmentation is due to the inclusion of the additional IOP terms including principal point offsets, calibrated focal length, radial lens distortion, and decentering lens distortion (Wolf and Dewitt 2000). The SCBA mathematical model presented in Equations 5-1 through Equation 5-8 is from Wolf and Dewitt (2000), where x_a, y_a are measured photo coordinates, x_o, y_o are principal point coordinates, k_1, k_2, k_3 are symmetric radial lens distortion coefficients, p_1, p_2, p_3 are decentering distortion coefficients, and f is calibrated focal length.

$$x_a = x_o - \bar{x}_a(k_1 r_a^2 + k_2 r_a^4 + k_3 r_a^6) - (1 + p_3^2 r_a^2)[p_1(3\bar{x}_a^2 + \bar{y}_a^2) + 2p_2 \bar{x}_a \bar{y}_a] - f \frac{r}{q} \quad (5-1)$$

$$y_a = y_o - \bar{y}_a(k_1 r_a^2 + k_2 r_a^4 + k_3 r_a^6) - (1 + p_3^2 r_a^2)[2p_1 \bar{x}_a \bar{y}_a + p_2(\bar{x}_a^2 + 3\bar{y}_a^2)] - f \frac{s}{q} \quad (5-2)$$

$$\bar{x}_a = x_a - x_o \quad (5-3)$$

$$\bar{y}_a = y_a - y_o \quad (5-4)$$

$$r_a^2 = \bar{x}_a^2 + \bar{y}_a^2 \quad (5-5)$$

The terms (q, r, s) are from the linearization of the collinearity equations, where m_{xx} are elements of the 3x3 Omega-Phi-Kappa (OPK) rotation matrix, X_A, Y_A, Z_A are object point coordinates, and X_L, Y_L, Z_L are exposure station coordinates.

$$q = m_{31}(X_A - X_L) + m_{32}(Y_A - Y_L) + m_{33}(Z_A - Z_L) \quad (5-6)$$

$$r = m_{11}(X_A - X_L) + m_{12}(Y_A - Y_L) + m_{13}(Z_A - Z_L) \quad (5-7)$$

$$s = m_{21}(X_A - X_L) + m_{22}(Y_A - Y_L) + m_{23}(Z_A - Z_L) \quad (5-8)$$

If the IOPs were omitted, the focal length and principal point offsets would need to be known from a previous calibration to perform a bundle adjustment with the non-augmented collinearity equations. The EOPs would be the only parameters solved for in this case.

5.2 Camera Calibration – Interior Orientation

Recall from Chapter 3 (Figure 3-8) that the offsets between the camera and GPS ARP are needed to determine the lever arm. Likewise, the rotation matrix between the camera coordinate frame (CF) and the IMU CF is necessary to rotate points captured by the imaging system into the mapping CF for vision-aiding. This rotation matrix is called the boresight calibration. The goal of performing a SCBA for determining the IOPs is to eventually fix these intrinsic parameters when performing the boresight angle-lever arm (BSLA) calibration.

Using a consumer off-the-shelf (COTS) DSLR camera has its potential disadvantages relative to using a traditional aerial photogrammetric sensor. Traditional aerial photogrammetric sensors have extremely stable interior orientation parameters. After calibration, the IOPs of these sensors are considered known parameters. Fewer unknowns in the bundle adjustment can result in higher confidence in the EOP results. Accurate and precise EOPs are essential for the BSLA calibration.

As COTS DSLR cameras have been used increasingly in close-range terrestrial applications, the IOPs for these cameras have been routinely studied to better understand the geometric consistency and stability of the intrinsic parameters. (Wackrow et al. 2007) studied the COTS Nikon® Coolpix® 5400 camera. During the investigation of 7 identical camera/lens combinations, the authors determined that the lens distortion curves were stable over the 1 year testing interval. The IOP stability from the Wackrow et al. (2007) study was encouraging that the IOPs for the 24mm Nikkor® lens (focus fixed at infinity and aperture fixed at f/22) would also have geometric stability through BSLA calibration and VA field testing.

5.2.1 Methods

Two software programs were used for camera calibration, PhotoModeler® 6 (PM) by Eos Systems™ Inc. and SCBUN by Bon Dewitt, PhD. SCBUN implements the SCBA mathematical model discussed in Section 5.1. Without explicitly indicating in the program documentation which SCBA model PM implements, the PM camera calibration module outputs the same interior orientation parameters as SCBUN. Using PM is advantageous for automarking hundreds of targets with sub-pixel accuracy. After performing camera calibration with PM, the results were verified against SCBUN. Before

comparing IOP results from the SCBAs, Table 5-1 outlines the primary differences in the programs that needed to be accounted for.

For the camera calibration process, a 3ft by 3ft calibration grid of 144 targets was used (Figure 5-1). To orient the camera in object space, four of the grid targets were auto-coded fiducial targets. Sub-pixel automarking of the targets was achieved through least squares matching or centroid determination. Since the object space distances between each target in the grid were known, targets which did not fit the object space coordinates with 95% certainty were rejected prior to the SCBA. Figure 5-1 also depicts a typical image after the automarking process.

Due to the use of a flat sheet calibration field, the main drawback to using PhotoModeler® 6 for the camera calibration is the lack of depth of field. This property makes the focal length a difficult parameter to resolve. A subsequent version of PM, PhotoModeler® 2011, has remedied this issue through the use of multi-sheet calibrations with autocoded targets. The sheets can be placed at varying heights giving proper depth of field. The author did not have access to the newer version of PM but suggests that others use that newest PM version for intrinsic camera calibration.

5.2.2 Results

Two intrinsic camera calibrations were run using PM to ensure calibration consistency. The data sets were collected on different days after attaching and detaching the 24mm lens. PM requires at least 6 photos of the calibration grid from a variety of angles and positions. When capturing images, the main premise is to fill the image with grid targets to properly model the lens distortion at the periphery of the image. The decision to use the smallest aperture setting available (f/22) was based on

reducing distortion for MMS operation. Table 5-2 outlines the IOP results for both 24mm Nikkor®-Nikon® D200 calibration tests

Since the intrinsic parameters directly affect the image coordinates (measured in pixels), it makes sense to convert these IOPs from mm to pixels. Furthermore, the mm-pixel conversion needs to be completed to verify the results with SCBUN. The dimensions of the D200 CCD array are 3872 x 2592 pixels. Using the format width and format height from each SCBA, the number of pixels per mm in height and width can be determined. The average of pix/mm(h) and pix/mm(w) is the conversion factor used. Table 5-3 shows the PM calibration results in an easier format to understand relative to the image points being measured.

As previously stated, the focal length is the most difficult parameter to resolve due to lack of depth of field. Thus, the geometric consistency between the two solutions especially with the radial distortion modeling is excellent. One additional check was performed to verify the solution uses the correct SCBA mathematical model. The image coordinates, control coordinates, and exterior orientation parameters were input into SCBUN. The interior orientation parameters were allowed to adjust without constraint. The results in Table 5-4 show that the SCBA model used by PM is consistent with SCBUN. The radial distortion curve produced from the SCBUN IOP results is shown in Figure 5-2. This figure shows the polynomial increase in distortion relative to the increase in the radial offset distance an image object is from the principal point. The SCBUN results were held for the BSLA calibration.

5.3 Boresight-Lever Arm Calibration

When designing GatorMMSv2.0, it was important that detaching and reattaching the D200 camera could be done with repeatable results. Thus, a goal of the design was

a fixed BSLA calibration. The bottom of the D200 has two sockets: a threaded tripod socket and a smaller locking socket. By fixing the camera to the aluminum frame with a 1/4"-20 tripod screw, the orientation was repeatable by inserting the head of a fixed 1/16" machine screw into the locking socket. The use of two screws provided repeatable BSLA results for both the horizontal and vertical D200 orientations.

5.3.1 Reed Lab Roof BSLA Calibration Field

To perform a BSLA calibration, establishment of a network of ground control points is necessary for accurate EOP determination from the SCBA. Thus, the GCPs needed mapping CF coordinates established with geodetic control. GPS observations and total station surveying were used to establish these mapping CF coordinates.

As the home to the University of Florida Geomatics department, the roof of Reed Lab (RLA) shown in Figure 5-3 provided a convenient location to perform the BSLA calibration. Three observation pillars are established on the RLA roof for previous and ongoing geodetic observation/testing. One of the pillars is used for the Florida Department of Transportation CORS station, RLAB. The pillar on the southwest corner of the RLA roof (RLABsw) was the occupation station for the reflectorless total station survey of the GCPs. A backsight (BS) for the TS survey was established $\pm 57\text{m}$ away on the ground near Rhines Hall. Each GCP target was observed with four sets of forward and reverse face reflectorless TS shots for maximum redundancy. Figure 5-4 shows a majority of the GCP targets viewed from the BSLA calibration area. The GCP targets were primarily retro-reflective targets with a 2mm diameter center hole used for sighting purposes

To establish geodetic control, two hour plus static GPS observations were undertaken simultaneously at RLABsw, BS, RLAB, and GNVL on four separate days in

September 2010 and October 2010. A network adjustment was performed with WIE's GrafNet® software package using GNVL and RLAB as master control stations. While GrafNet® is purely a geodetic processing software package, the GNSS processing engines are the same GNSS engines used when processing the inertial trajectories. This ensures consistency in the GPS/GNSS processing solutions. The results of the network adjustment were imported into Topcon® Corporation's Topcon Tools™ 7.2 software, a package capable of processing both total station and GPS observations. When adjusting the total station observations, the WGS84 GNSS solution from GrafNet® was held as control. The sub-cm precision mapping CF control point coordinates found in Table 5-5 are given in WGS84 UTM 17N.

5.3.2 BSLA Calibration Methods

From Chapter 3 and (Ellum and El-Sheimy 2002), the two variables being solved for in the BSLA calibration are the lever arm from the GPS ARP to the camera (\mathbf{r}_{GPS}^{cam}) and the boresight angles between the IMU CF and the camera CF (\mathbf{R}_{cam}^{IMU}). The lever arm between the GPS ARP and the IMU center (\mathbf{r}_{IMU}^{GPS}) is straightforward using conventional measuring techniques and mechanical drawings. This lever arm position vector (DX, DY, DZ) in the IMU CF for GatorMMSv2.0 is (0.000m, -0.008m, 0.242m). The default navigation trajectory output from Waypoint® Inertial Explorer™ is the mapping CF coordinates of the IMU CF origin. Thus, the lever arm between the ARP and the camera has been reduced to the lever arm between the IMU center and the incident nodal point of the lens (\mathbf{r}_{IMU}^{cam}). The incident nodal point of the lens can only be estimated as its physical location is difficult to measure. Using EOPs derived from the

SCBA of the BSLA calibration field (\mathbf{r}_{cam}^{Map} and \mathbf{R}_{Map}^{cam}) and the position from the navigation trajectory solution (\mathbf{r}_{IMU}^{Map}), the lever arm is easily derived in Equation 5-9.

$$\mathbf{r}_{IMU}^{cam} = \mathbf{R}_{Map}^{cam} (\mathbf{r}_{IMU}^{Map} - \mathbf{r}_{cam}^{Map}) \quad (5-9)$$

To determine the boresight angles, the angular rotations in the OPK convention are output from WIE as the orientation component of the navigation trajectory. The OPK convention is used to describe the angular rotation matrix from the mapping CF (ground) to the camera (\mathbf{R}_{Map}^{cam}) and the IMU (\mathbf{R}_{Map}^{IMU}). To utilize the boresight angles in WIE after calibration, the rotation matrix from the IMU CF to the camera CF (\mathbf{R}_{IMU}^{cam}) is desired as shown in Equation 5-10.

$$\mathbf{R}_{IMU}^{cam} = \mathbf{R}_{Map}^{cam} (\mathbf{R}_{Map}^{IMU})^T \quad (5-10)$$

To perform the SCBA in SCBUN, initial approximations for the EOPs were necessary. The simplest method for obtaining the angular approximations was estimating the initial boresight angle rotation matrix (\mathbf{iR}_{IMU}^{cam}) to be ($\omega=90^\circ$, $\phi=90^\circ$, $\kappa=0$) within the export wizard of WIE. Figure 5-5, which depicts the camera and IMU CFs, is a visual aid for approximating the orientation of the IMU CF with respect to the camera CF.

5.3.3 BSLA Calibration Results

The BSLA calibration was performed on February 8, 2011. Thirty images captured at various EOP angles were acquired over a ± 5 m path on the RLA roof while maintaining a set distance from the calibration field. Thirteen images from the 30 second sample were used in the calibration. After quality checking the GNSS and inertial navigation solutions, one navigation trajectory was output from WIE. This

trajectory included the position of the IMU center with respect to the mapping CF and OPK expressed in the orientation of the camera coordinate frame as estimated with the (90°-90°-0°) boresight angles. The image points were marked by hand using an ImagePick script written for MATLAB®. The magnification tools with this script enabled the estimated precision of the image coordinates to be ±0.5pix. Also, recall that the IOPs from the camera calibration testing were fixed. This means the inputs subject to greatest adjustment were the EOP initial approximations.

The difference between the initial EOP approximations and the EOP results from the SCBA provided the data for the BSLA calibration derivation. The lever arm offsets for \mathbf{r}_{IMU}^{cam} of GatorMMSv2.0 expressed along the x, y, and z axes of the IMU coordinate frame are in Table 5-6. Likewise, the boresight angle updates ($\Delta\mathbf{R}_{IMU}^{cam}$) for GatorMMSv2.0 expressed in OPK are in Table 5-7. Figure 5-6 shows the estimated angular precision of the navigation trajectory. The orientation results from the BSLA calibration with mm level precision for the lever arm and milliradian precision for the boresight angles are excellent relative to the input standard deviations.

The original boresight angle estimation (\mathbf{iR}_{IMU}^{cam}) and the boresight angle correction ($\Delta\mathbf{R}_{IMU}^{cam}$) are combined in Equation 5-11 to determine the final set of boresight angles.

$$\mathbf{R}_{IMU}^{cam} = \Delta\mathbf{R}_{IMU}^{cam} \mathbf{iR}_{IMU}^{cam} \quad (5-11)$$

The final boresight angles were input into WIE. A navigation trajectory with the final boresight angles was checked against the EOP results from the SCBA. The discrepancies between these sets of orientation angles for each image were all within the acceptable tolerance level of milliradian precision noted in Table 5-7. Angular

precision is essential because angular error propagates over the distance the object is from the sensor. The BSLA orientation angle precisions are approximately 0.05 degrees which is one milliradian apiece. This means for every meter an object is from the sensor the corresponding error grows by approximately 1mm. These satisfactory final BSLA calibration results to be used in the vision-aiding testing are in Table 5-8.

5.4 Imaging System Testing Lessons Learned

Multiple lessons can be taken from the GatorMMSv2.0 imaging system testing for application to subsequent GatorMMS generations. For camera calibration, it is essential to maximize the depth of field for determining the IOPs of a camera, especially focal length. Thus, a three-dimensional calibration grid as opposed to the two-dimensional calibration plane used herein is ideal. Furthermore, a commercial software package that automarks points using coded targets is excellent for efficiency. However, the automarking method must contain quality control measures to ensure accuracy. Also, initial difficulty was encountered with the transfer and comparison of camera calibration parameters between software packages. Thus, knowing the camera coordinate system orientation for each software package is essential.

For future testing, BSLA calibration could be performed for each canopy density or vision-aiding test. To do so, a routine should be established to minimize systematic errors. For instance, a calibration grid could be brought to the field for IOP determination both before and after data collection for geometric stability of the COTS DSLR lens/camera combinations.

Table 5-1. Differences in camera calibration software programs.

Property	PhotoModeler® 6	SCBUN
Origin of Image Plane	Top Left	Bottom Left
Direction of +Z Axis	Out from Camera Body	Into Camera Body
IOP Output Units	mm	pixels

Table 5-2. IOP camera calibration results from PhotoModeler® 6. The parameters are consistent between the two data sets. Note that the decentering distortion is negligible for this lens/camera combination.

	Test 1	Test 2
SCBA Images	9	7
Focal Length (mm)	25.173516	25.197745
σ – FL (mm)	0.008	0.017
Xp - principal point x (mm)	11.903442	11.918081
σ – Xp (mm)	0.001	0.003
Yp - principal point y (mm)	8.145751	8.126415
σ – Yp (mm)	0.002	0.005
Fw - format width (mm)	23.999625	23.999150
σ – Fw (mm)	3.5e-004	5.9e-004
Fh - format height (mm)	16.066116	16.066116
K1 - radial distortion 1	1.58E-04	1.60E-04
σ - K1	1.80E-06	2.40E-06
K2 - radial distortion 2	-1.97E-07	-2.12E-07
σ - K2	8.90E-09	1.10E-08
K3 - radial distortion 3	0.00E+00	0.00E+00
P1 - decentering distortion 1	0.00E+00	0.00E+00
P2 - decentering distortion 2	0.00E+00	0.00E+00

Table 5-3. IOP camera calibration results from PhotoModeler® 6 converted to pixels from mm. The largest discrepancies between the two data sets are the principal point offsets and focal length.

	Test 1	Test 2
SCBA Images	9	7
Fw - format width (mm)	23.999625	23.99915
Fh - format height (mm)	16.066116	16.066116
Fw - pix	3872	3872
Fh - pix	2592	2592
pix/mm (w)	161.336	161.339
pix/mm (h)	161.333	161.333
avg pix/mm	161.335	161.336
Focal Length (pix)	4061.359	4065.308
σ - FL (pix)	1.291	2.743
Xp - principal point x (pix)	1920.437	1922.818
σ - Xp (pix)	0.161	0.484
Yp - principal point y (pix)	1314.191	1311.085
σ - Yp (pix)	0.323	0.807
K1 - radial distortion 1	6.05E-09	6.13E-09
σ - K1	6.92E-11	9.22E-11
K2 - radial distortion 2	-2.91E-16	-3.13E-16
σ - K2	1.31E-17	1.62E-17
K3 - radial distortion 3	0.00E+00	0.00E+00
P1 - decentering distortion 1	0.00E+00	0.00E+00
P2 - decentering distortion 2	0.00E+00	0.00E+00

Table 5-4. IOP camera calibration verification results. The differences between the two camera calibration software packages were negligible. This ensures the correct implementation of the SCBA mathematical model in PM. Note the principal point offset for y of the SCBUN solution was converted from the SCBUN camera CF orientation to the PM camera CF orientation.

	Test 2 - PM	Test 2 - SCBUN
SCBA Images	7	7
Focal Length (pix)	4065.308	4065.872
σ - FL (pix)	2.743	2.822
Xp - principal point x (pix)	1922.818	1922.972
σ - Xp (pix)	0.484	0.844
Yp - principal point y (pix)	1311.085	1310.453
σ - Yp (pix)	0.807	1.029
K1 - radial distortion 1	6.12769E-09	6.35E-09
σ - K1	9.22036E-11	1.75E-10
K2 - radial distortion 2	-3.13197E-16	-4.33E-16
σ - K3	1.62355E-17	8.65E-17
K3 - radial distortion 3	0	1.96E-23
σ - K2		1.45E-23
P1 - decentering distortion 1	0	-8.47E-10
σ - P1		1.65E-08
P2 - decentering distortion 2	0	-4.07E-08
σ - P2		1.76E-08

Table 5-5. RLA BSLA calibration field coordinates. These coordinates will be used for the EOP determination in the SCBA. Note that the standard deviations for RLAB and GNVL are 0 because these are published coordinates transformed into the WGS84 UTM 17N mapping CF.

Name	Easting (m)	Northing (m)	h (m)	Control	σ_h (m)	σ_{Hor} (m)
G1	369508.558	3280549.591	23.886	None	0.005	0.006
G2	369510.449	3280549.570	23.886	None	0.005	0.006
G3	369512.322	3280549.546	23.889	None	0.005	0.006
G4	369520.075	3280543.551	23.906	None	0.005	0.006
G5	369520.026	3280538.822	23.904	None	0.005	0.006
OB1	369511.790	3280550.624	24.202	None	0.005	0.006
OB2	369512.275	3280550.622	25.822	None	0.005	0.006
OB3	369512.696	3280550.616	25.423	None	0.005	0.006
OB4	369512.905	3280550.613	24.202	None	0.005	0.006
OB5	369514.525	3280550.596	25.035	None	0.005	0.006
OB6	369515.211	3280550.587	25.634	None	0.005	0.006
GB1	369516.596	3280550.570	25.506	None	0.005	0.006
GB2	369516.897	3280550.552	26.242	None	0.005	0.006
GB3	369517.362	3280550.552	25.947	None	0.005	0.006
BS1	369454.111	3280530.302	12.343	Both	0.004	0.005
GNVL	376457.776	3284735.156	22.421	Both	0	0
RLAB _{sw}	369509.654	3280523.723	24.950	Both	0.004	0.005
RLAB	369518.291	3280523.869	25.130	Both	0	0

Table 5-6. GatorMMSv2.0 lever arm calibration results. The results are expressed along the x, y, and z axes for the IMU CF. The x and z lever arm offsets are quite stable. Meanwhile, the y lever arm offset is not as stable.

Image	x	y	z
AB5_0042	-0.262	0.030	0.020
AB5_0044	-0.253	0.030	0.013
AB5_0046	-0.254	0.037	0.019
AB5_0048	-0.252	0.035	0.011
AB5_0050	-0.247	0.037	0.009
AB5_0051	-0.249	0.029	0.010
AB5_0053	-0.265	0.024	0.026
AB5_0059	-0.267	0.023	0.018
AB5_0062	-0.252	0.006	0.020
AB5_0063	-0.264	0.012	0.009
AB5_0066	-0.258	0.012	0.030
AB5_0067	-0.258	-0.008	0.021
AB5_0068	-0.247	0.018	0.018
Mean	-0.256	0.022	0.017
σ	0.007	0.014	0.007

Table 5-7. GatorMMSv2.0 boresight angle calibration results. These angles reflect the difference from the initial (90°-90°-0°) approximation. The precision of all three boresight angles is less than 5 arcminutes each.

Image	ω	ϕ	κ
AB5_0042	-0.7319	-4.0082	-0.2174
AB5_0044	-0.7360	-4.0221	-0.2692
AB5_0046	-0.7690	-3.7949	-0.2430
AB5_0048	-0.7397	-4.0195	-0.2012
AB5_0050	-0.7558	-4.0123	-0.3068
AB5_0051	-0.7077	-3.9893	-0.2786
AB5_0053	-0.6527	-3.9329	-0.2294
AB5_0059	-0.7047	-3.8797	-0.2493
AB5_0062	-0.6031	-3.9582	-0.2218
AB5_0063	-0.6532	-4.0442	-0.2630
AB5_0066	-0.6607	-3.9097	-0.2485
AB5_0067	-0.5094	-3.9495	-0.3053
AB5_0068	-0.7427	-4.0244	-0.2568
Mean	-0.6898	-3.9650	-0.2531
σ - deg	0.0730	0.0715	0.0320
σ - arcmin	4.4	4.3	1.9

Table 5-8. GatorMMSv2.0 final BSLA calibration results. The lever arm is the position of the camera with respect to the center of the IMU in the IMU CF. The boresight angles are the rotations from the center of the IMU to the incident nodal point of the camera lens about the x, y, and z axes of the IMU CF.

Boresight Angles			Lever Arm Offsets		
Omega	Phi	Kappa	x	y	z
80.14711°	85.97555°	9.62366°	-0.256m	0.022m	0.017m

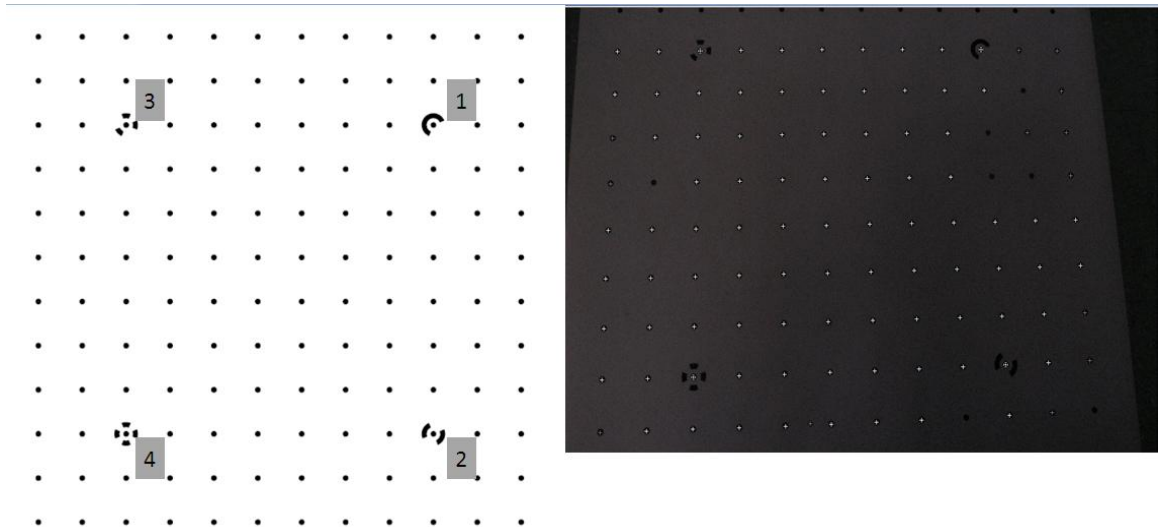


Figure 5-1. PhotoModeler® camera calibration grid. The fiducial targets labeled in the left photo are automatically identified by the number of dashes around the target. The white sub-pixel automarks in the right photo passed all quality control checks for inclusion in the SCBA. (images courtesy of author)

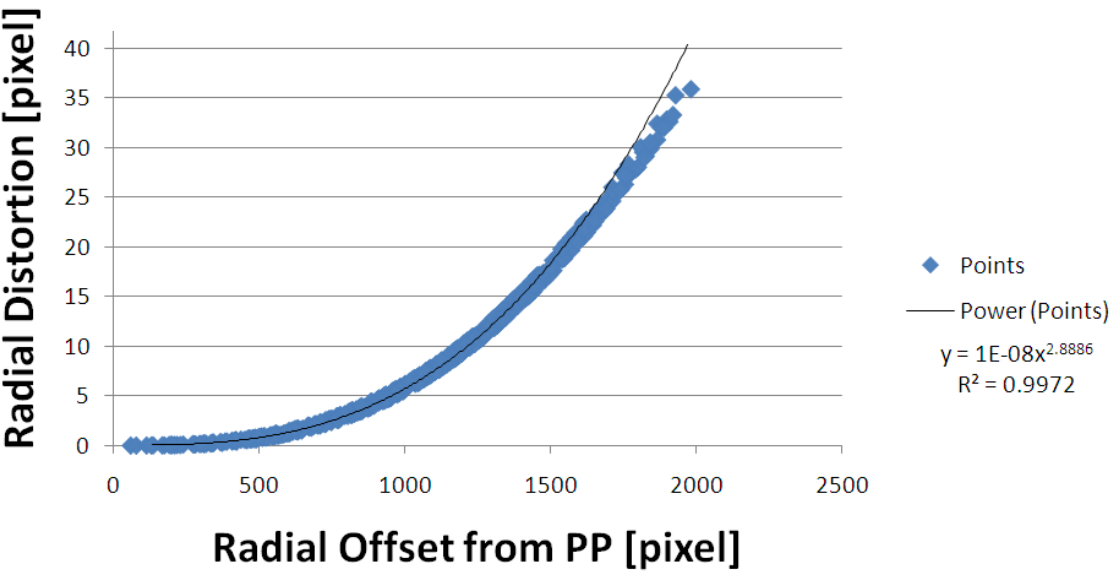


Figure 5-2. Radial lens distortion curve for the Nikon D200. Radial distortion increases polynomially the further away from the principal point. Without correcting for lens distortion in the SCBA model, a BA utilizing the collinearity equations would not provide usable results.



Figure 5-3. Vicinity map of Reed Lab BSLA calibration field. The field was established with nine targets on the wall of the staircase to the roof (southern face of the white rectangle lying to the north of the RLA roof) and five targets along the northern portion of the RLA roof gutter. (image from Google Earth™)

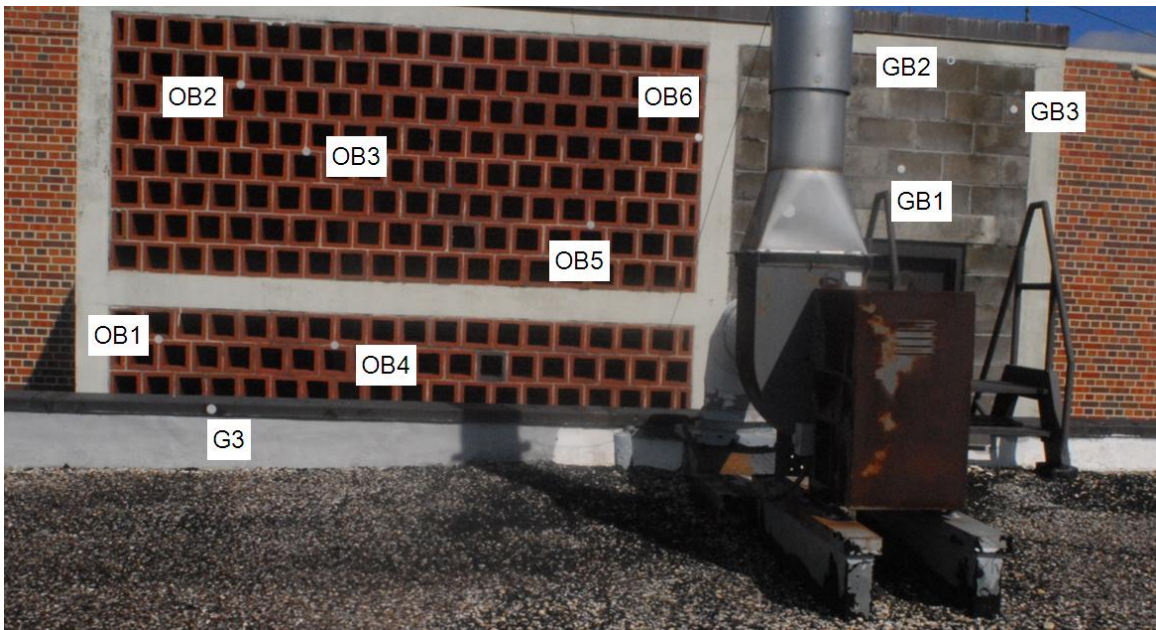


Figure 5-4. Roof view of RLA BSLA calibration field GCPs. The GCP targets were primarily retro-reflective targets with an approximately 2mm diameter center hole for sighting purposes. Target GB2 was a PK nail surrounded by alternating white and black concentric circular washers for maximum contrast in the imagery. (image courtesy of author)

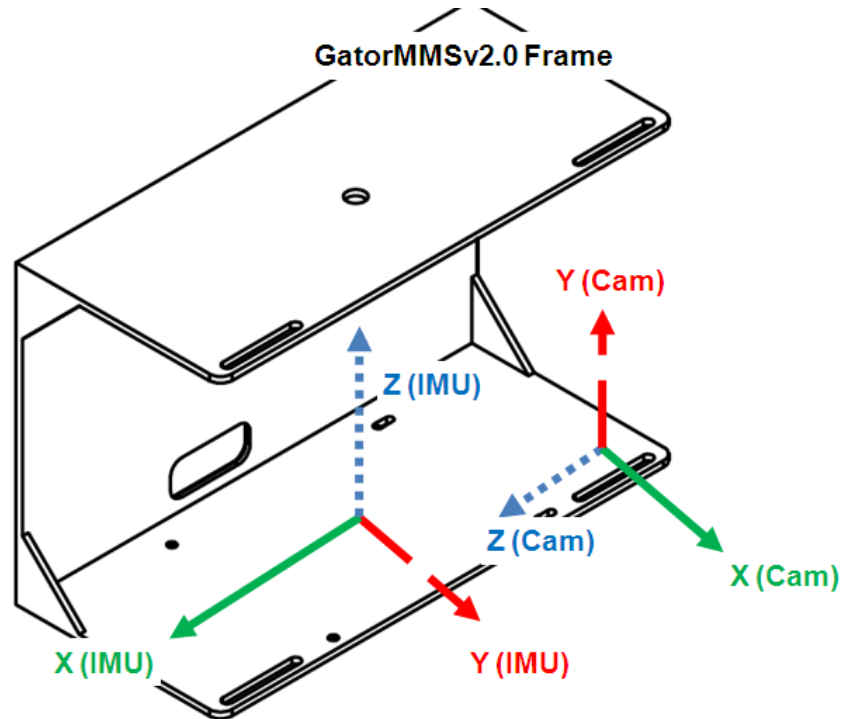


Figure 5-5. GatorMMSv2.0 camera & IMU coordinate frames. Note that the angular rotations are positive counterclockwise when looking down the arrow towards the origin of the CF. Omega (ω) is about the x-axis. Phi (ϕ) is about the once rotated y-axis. Kappa (κ) is about the twice rotated z-axis.

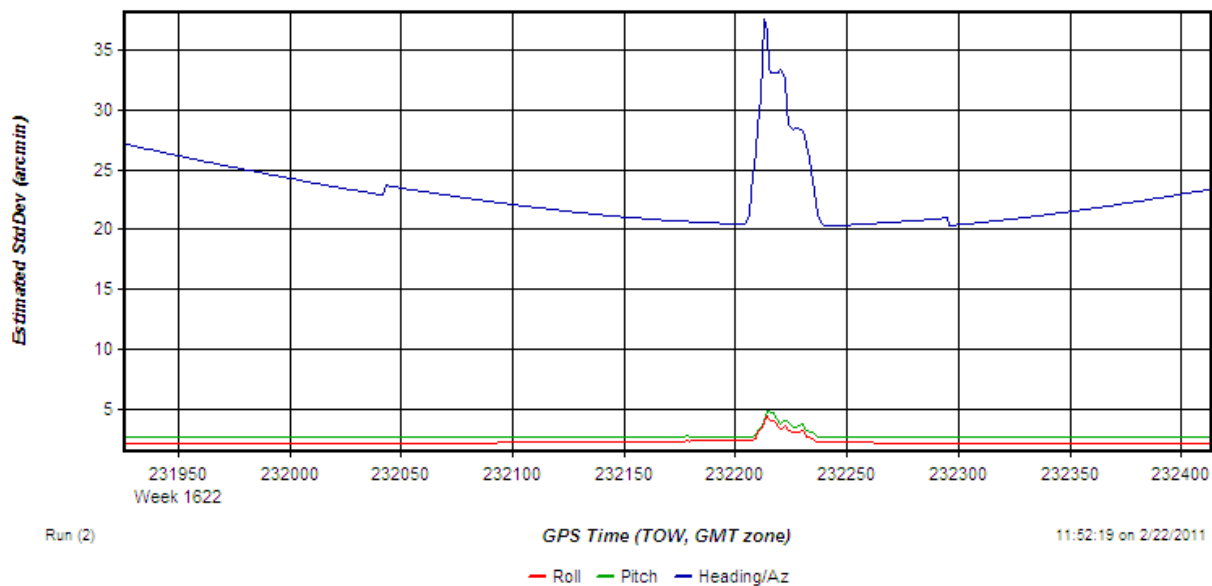


Figure 5-6. Estimated angular orientation precision from BSLA calibration. As expected, the orientation precision is more stable in the horizontal channels than the vertical channel.

CHAPTER 6
GATORMMS: VERTICAL ORIENTATION FOR CANOPY DENSITY ANALYSIS

6.1 GatorMMSv2.0 Applications – Canopy Density Analysis

GatorMMS development has been the focal point of discussion thus far.

Discussion of the application of this technology for use as a mobile terrestrial remote sensing system has been minimal. This chapter investigates one remote sensing application of the GatorMMSv2.0, canopy density analysis.

Canopy density is the proportion of the sky obscured by vegetation when viewed from a single point near the ground (Figure 2-1). Thus, the term ‘canopy’ actually includes overhead vegetation, tree trunks, and lower tree branches. Previously mentioned in the forest mapping background, skyward-looking hemispherical photography used to capture a wide angle view of the forest canopy from a single point is implemented extensively in GPS studies relating canopy density to GPS positional performance (Jennings et al. 1999; Sigrist et al. 1999; Frazer et al. 2001; Holden et al. 2001; Zheng et al. 2005; Hu et al. 2009). To determine canopy density using a digital image, sky pixels need to be differentiated from canopy pixels. Image thresholding is the simplest method for segmenting images. The canopy density index (CDI) is the proportion of canopy pixels to total pixels in a segmented image.

6.2 Methods

To capture the necessary canopy imagery, the vertically-oriented D200 is equipped with the 8mm f/3.5 Manual Focus Pro-Optic® fisheye (FE) lens (Figure 3-6). The Pro-Optic® FE lens and D200 camera produce a diagonal 180° fisheye image. Figure 6-1 modified after Schneider et al. depicts the effective field of view (FOV) of this lens-camera combination relative to the FOV for a circular 180° fisheye lens-camera

combination. The primary drawback of using the diagonal FE format is cropping large areas of the canopy in front of and behind the GatorMMS. An advantage of the diagonal FE format is using the entire sensor means greater detail of objects captured in the image.

After acquiring jpeg images of the canopy, image processing is necessary to determine the CDI. Conversion of the full color jpegs to grayscale images is a simple process whereby only the intensity channel is preserved. The grayscale images are the input for the image thresholding algorithm. The goal of the algorithm is to convert these grayscale images into binary images with the two binary classes representing forest canopy and sky.

Zheng et al. (2005) had success using Otsu's image thresholding method for segmenting canopy pixels from sky pixels. Otsu's image thresholding method analyzes the intensity pixel data for a bimodal distribution. Briefly, a mean is calculated for each mode. From the means, variances for each of the subsets are computed. The variance is a common measure for subset homogeneity. Thus, a low homogeneity subset will have high variance (Zheng et al. 2005). The goal of Otsu's image thresholding is minimizing the intra-group variance between the two subsets. For more information on this method, consult Zheng et al. (2005), Otsu (1979), or Appendix A for the derivation of Otsu's thresholding method.

For algorithm success, it is important that homogenous lighting is available throughout the image. On a sunny day, the area where the sun shines through the canopy on one part of the image makes the intensity values for those sky pixels vastly

different than sky pixel intensity values in another portion of the image. This phenomenon skews the bimodal distribution. Thus, a cloudy day is ideal.

Using MATLAB®, a batch processing algorithm was developed to handle all of the images along the navigation trajectory. MATLAB® has a built-in function called 'graythresh' which implements Otsu's algorithm. Quality control and quality assurance (QC\QA) of the output binary images is necessary. Visual comparison of original images with binary images is sufficient QC\QA for this analysis. A simple ratio of canopy pixels to total pixels is satisfactory for computing the canopy density index (CDI).

6.3 Preliminary Image Processing Results

Preliminary testing of the image processing algorithm was necessary prior to implementation on the forest navigation data sets. On January 6, 2011, a set of vertically-oriented images was collected along a walkway adjacent to the North Lawn on the University of Florida Gainesville campus. The partly sunny weather conditions were not ideal for the bimodal distribution. Figure 6-2 is a sample image from the set of 26 images with the subsequent output grayscale and binary images. The use of the intensity channel for the grayscale image was not reliable due to a large portion of the sky misclassified as canopy.

Previous studies indicated using the intensity from only the blue channel of a red-green-blue (RGB) jpeg image was the best way to separate sky from canopy (Frazer et al. 2001, Nobis and Hunziker 2005). After implementing this change in the MATLAB® algorithm, the results were drastically improved (Figure 6-3). Further preliminary testing under cloudy conditions confirmed that using the blue channel intensity was the optimal image component for thresholding.

6.4 GatorMMS Testing Results

The premise of this remote sensing application is to analyze CDI relative to the navigation trajectory solution. GatorMMS testing of the vertically-oriented D200 FE lens combination was conducted in Austin Cary Memorial Forest on January 27, 2011 and March 3, 2011 (Figure 6-4).

The cloudy conditions near dusk in January were optimal for canopy density analysis. The MATLAB® script using blue channel intensity was implemented with excellent results. Figure 6-5 shows typical results of the image processing.

Unfortunately, the inertial navigation data acquired with the images was not capable of being processed in Waypoint® Inertial Explorer™. Short initial static alignments with poor GPS satellite coverage are the likely culprits for lack of an inertial navigation trajectory solution. This processing issue was resolved in March. With a lack of GPS positions along the trajectory in January, georeferencing the images without the inertial data was not an option. Thus, the primary relationship sought in the CDI versus navigation trajectory analysis could not be pursued from the January data sets.

Interestingly, analysis of the CDI spikes in Figure 6-6 can help with interpolation of the GatorMMS location along test track 2. For instance, the GatorMMS was initialized in an open area lacking substantial forest canopy at the southern end of test track 2. Shortly after heading northward, the canopy became denser in image 25 before opening up again near a newly planted pine stand in image 40.

On March 3, 2011, conditions for acquiring quality canopy imagery were suboptimal due to bright sun visible in most photos. While the acquisition time of day was approximately the same as during the January data collection, the daylight hours were considerably longer in March leading to a higher sun elevation. Furthermore, few

clouds meant the sun would rarely be obscured from the FOV of the lens. These discouraging factors meant only one trial around test track 1 of vertically-oriented imagery was collected. Given the obstacles encountered in the field, Figure 6-7 is a typical example of the surprisingly decent CDI results from the March testing. The impact of the sun directly shining through portions of the canopy was expected to have a more adverse impact on the thresholding algorithm than the final March results reveal. Post mission analysis of the CDI levels over the course of the test trail show there is considerably less variability in the canopy density of test track 1 (Figure 6-8) than in test track 2 (Figure 6-6).

There were no issues preventing the raw inertial navigation data from being processed in WIE. However, the lack of canopy variability severely hampered the analysis of a relationship between the navigation trajectory position solution and CDI. Precision statistics regarding the inertial trajectory solution were output from Inertial Explorer™. Unfortunately, important data regarding signal-to-noise ratio (SNR) was unavailable. Analysis of the independent variable CDI against the available positional precision metrics was undertaken through graphical analysis and then more rigorous hypothesis testing. CDI significantly impacts the horizontal and vertical positional precision of the tightly coupled position solution (Figure 6-9) or the GNSS-only position solution (Figure 6-10). Furthermore, the positional precision is most significantly impacted by the long static initialization periods at the beginning and end of the data sets (Figure 6-11).

From visual analysis of Figure 6-11, further investigation into the relationship between time elapsed from static observation and horizontal precision was necessary.

A correlation coefficient of nearly 1 seen in Figure 6-12 indicated that there is a strong linear relationship between elapsed time from static observation and horizontal precision.

To test the statistical significance of the correlation coefficients discussed in Figure 6-9 through Figure 6-12, correlation hypothesis testing was undertaken. Hypothesis testing determined if the sample correlation coefficient (R-value) was statistically significant relative to the population correlation coefficient (ρ) at a 99.9% level of significance. Table 6-1 shows the only statistically insignificant linear or exponential relationship between two variables at a 99.9% confidence level was the linear relationship between CDI and PDOP.

$$H_0(\text{Null Hypothesis}): \rho = 0 \quad (6-1)$$

$$H_A(\text{Alternate Hypothesis}): \rho \neq 0 \quad (6-2)$$

$$n(\text{Sample Size}) = 200 \quad (6-3)$$

$$\alpha = 0.001 \text{ (Two-Tailed Test)} \quad (6-4)$$

$$\text{Test statistic: } t = \sqrt{r^2} * \frac{\sqrt{n-2}}{\sqrt{(1-r^2)}} \quad (6-5)$$

$$\text{Critical value from } t \text{ table: } t_{\alpha/2, \infty} = t_{0.005, \infty} = 3.300 \quad (6-6)$$

$$\chi_v^2(\text{See table test statistics}) < \chi_{0.05, 4}^2(3.300) \text{ False} \quad (6-7)$$

For all variable pairs except the linear relationship between CDI and PDOP, the null hypothesis H_0 can be rejected with a 0.1% probability of committing a Type 1 error

(false positive). Therefore, it can be said that the population correlation coefficient between each remaining variable and CDI is both nonzero and significant. From Table 6-1, the correlation between time elapsed and horizontal precision was the most statistically significant relationship.

6.5 GatorMMS Canopy Density Analysis Lessons Learned

Many difficulties were encountered with the analysis of canopy density relative to the navigation trajectory solution. These issues included imagery acquisition conditions, inertial processing aspects, and data analysis conclusions. Multiple lessons learned can be applied to future canopy density studies.

While cloud cover and an acquisition time near dusk are optimal, excellent results can still be achieved when the sun is visible by using the blue channel of RGB images to separate sky from forest canopy. Unfortunately, using these thresholding results with inertial navigation data is often not feasible without long static initializations at the beginning and end of each test. The long initializations reduce the chances that inertial navigation data sets will be unusable.

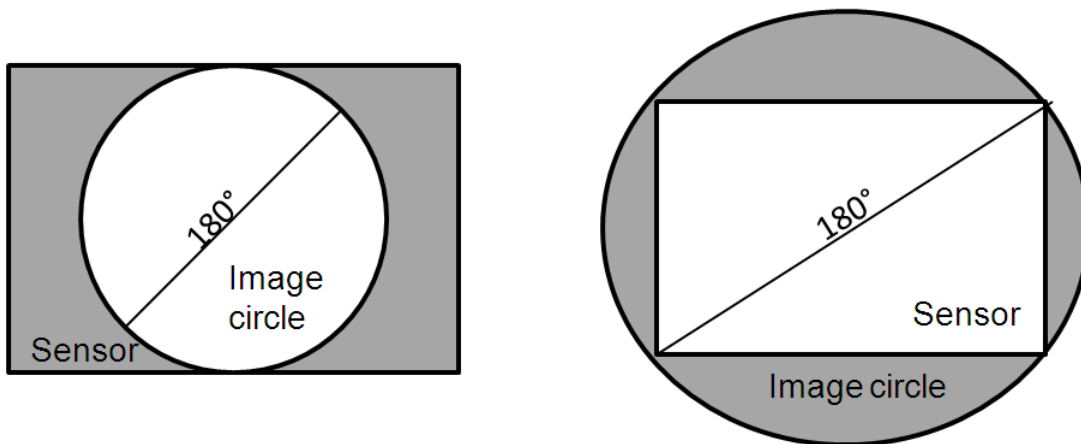
The ideal test track should have large variability in canopy density with multiple iterations of traversing between open field and thick woods. This will help break the correlation between initialization and positional precision. Furthermore, multiple passes of the same test track over different days will create a solid foundation for the relationship between CDI (which should be fairly static) and position precision (which should fluctuate depending upon the satellite configuration).

Investigation of additional parameters could make the comparison of canopy characteristics and inertial navigation parameters more robust. Using software that is capable of extracting the signal-to-noise ratio (SNR) would provide another metric to

evaluate against CDI. Also, canopy gap (structure) is another canopy metric that could be evaluated against positional precision and SNR.

Table 6-1 Hypothesis testing of CDI correlation for statistical significance of relationships. All but one relationship is statistically significant at a 99.9% level of confidence.

Variable Relationship	r^2	t (Test Statistic)
Time vs. Hor σ - Linear	0.9884	129.888
CDI vs. Satellites - Linear	0.1231	5.272
CDI vs. Satellites - Exponential	0.1133	5.030
CDI vs. PDOP – Linear	0.0434	2.997
CDI vs. PDOP - Exponential	0.0738	3.972
CDI vs. Hor σ TC - Linear	0.5570	15.778
CDI vs. Hor σ TC - Exponential	0.7079	21.905
CDI vs. Hor σ GNSS - Linear	0.2171	7.410
CDI vs. Hor σ GNSS - Exponential	0.5743	16.344
CDI vs. Ver σ TC - Linear	0.4926	13.865
CDI vs. Ver σ TC - Exponential	0.7219	22.671
CDI vs. Ver σ GNSS – Linear	0.2142	7.347
CDI vs. Ver σ GNSS – Exponential	0.5528	15.645



Circular 180° FE

Diagonal 180° FE

Figure 6-1. Fisheye field of view comparison. Depending on the application, a diagonal or circular FE could be more beneficial. (i.e. greater detail vs. greater coverage area) (Modified after Schneider, D., E. Schwalbe, and H. G Maas. 2009. Validation of geometric models for fisheye lenses. *ISPRS Journal of Photogrammetry and Remote Sensing*. 64 (3): 259–266).



Figure 6-2. Image thresholding implementation example for grayscale images. Less than ideal sky conditions led to poor final canopy density index results. (images courtesy of author)



Figure 6-3. Image thresholding implementation example for blue channel only grayscale images. Less than ideal sky conditions did not corrupt the canopy density index results. The binary image passes the visual QC/QA. (images courtesy of author)

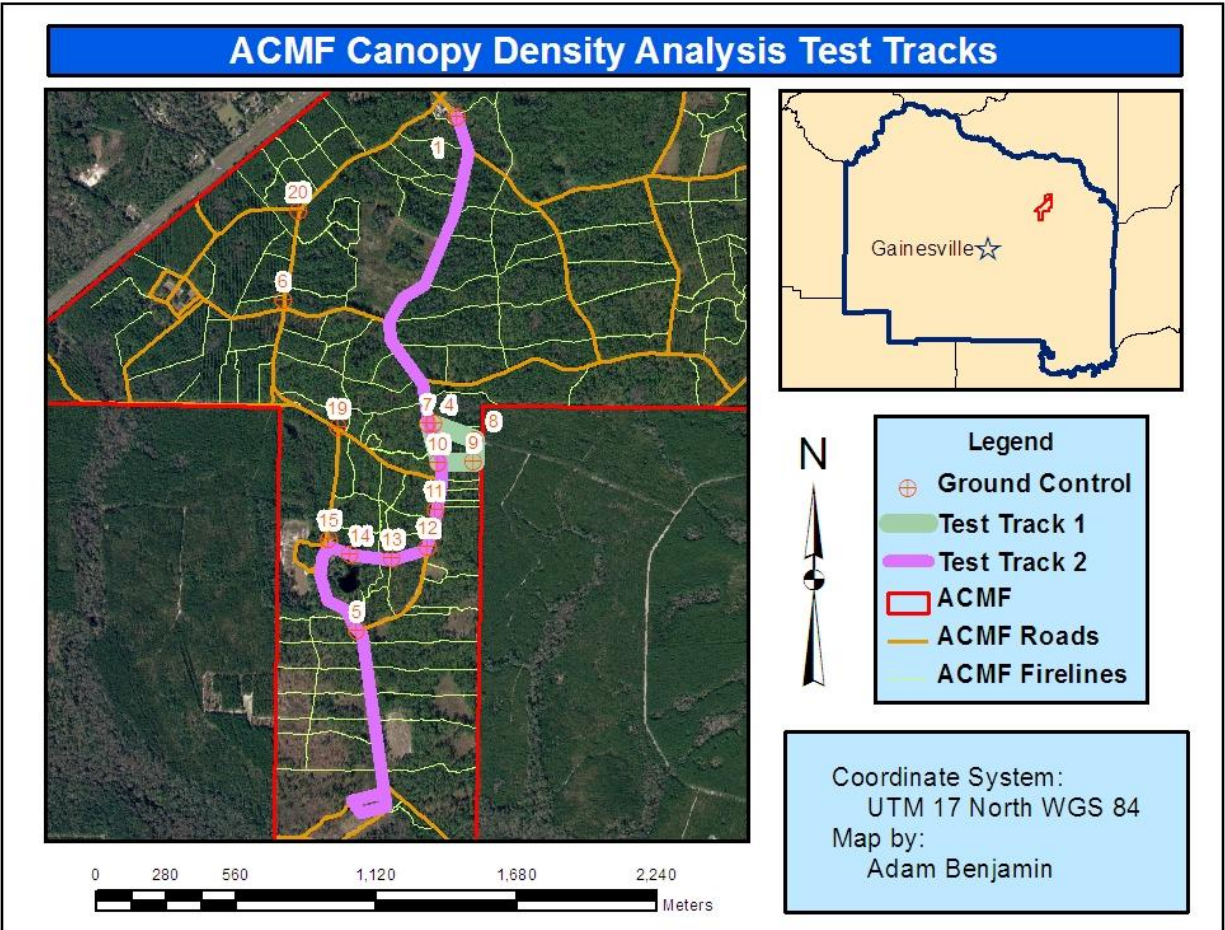


Figure 6-4. Map of ACMF CDI analysis test tracks. On January 27, 2011, the northern portion of track 2 and track 1 was run as one combined test trial. Also in January, track 2 was run once from south to north. On March 3, 2011, track 1 was run once.



Figure 6-5. Typical image from ACMF CDI analysis on January 27, 2011. With dusk approaching and consistent cloud cover, weather conditions were optimal. Excellent results such as these from the CDI algorithm implementation passed the visual QC/QA. (images courtesy of author)

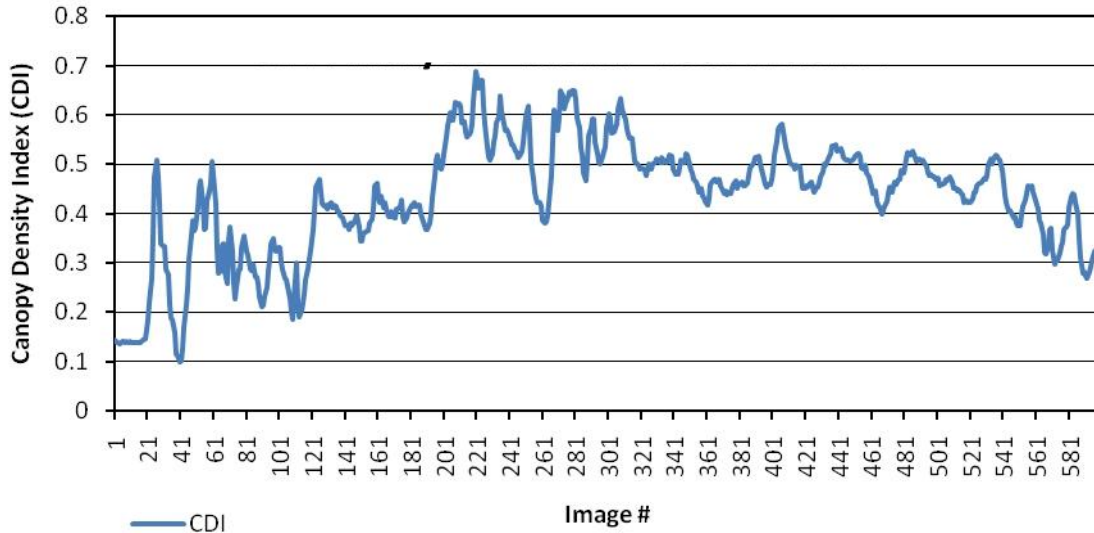


Figure 6-6. Plot of CDI results from ACMF test track 2. The sharp spikes in the CDI trajectory indicate leaving/entering open canopy areas. For example, the GatorMMS was initialized in an open area lacking substantial forest canopy at the southern end of test track 2. Shortly after heading northward, the canopy became denser in image 25 before opening up again near a newly planted pine stand in image 40.



Figure 6-7. Typical image from ACMF CDI analysis on March 3, 2011. The sun is visible in the lower left hand corner of the RGB image. This causes a portion of the final binary image to be washed out (Note the missing tree trunk in the lower left hand portion of the binary image). The washout causes the reported CDI level to be slightly lower than the true CDI. However, the CDI value is still representative of the canopy density. (images courtesy of author)

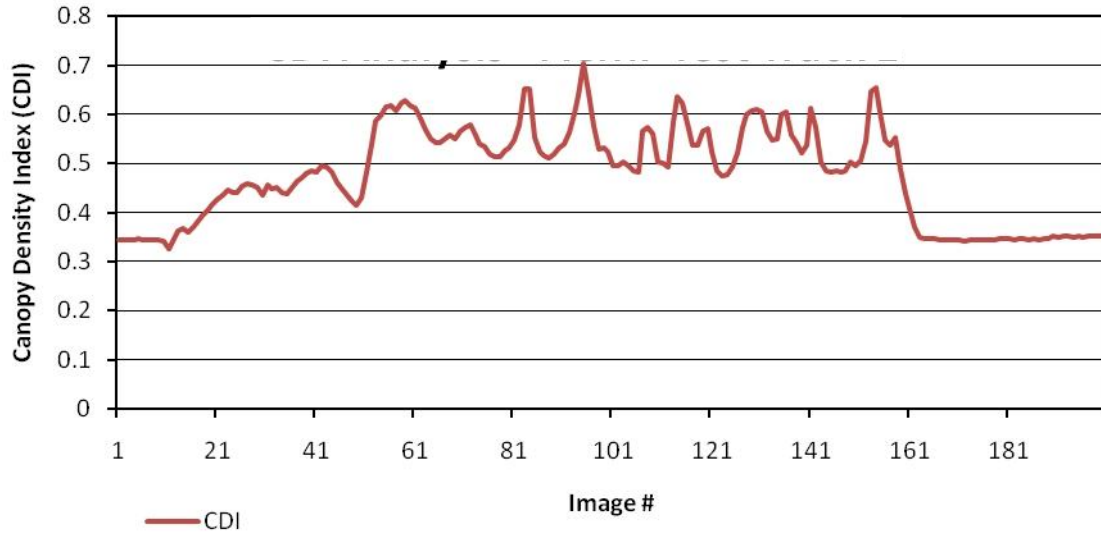


Figure 6-8. Plot of CDI results from ACMF test track 1. GatorMMS initialization was in the area with the least amount of canopy cover along test track 1. However, the canopy density at initialization was still substantial. This led to little variability along the test track.

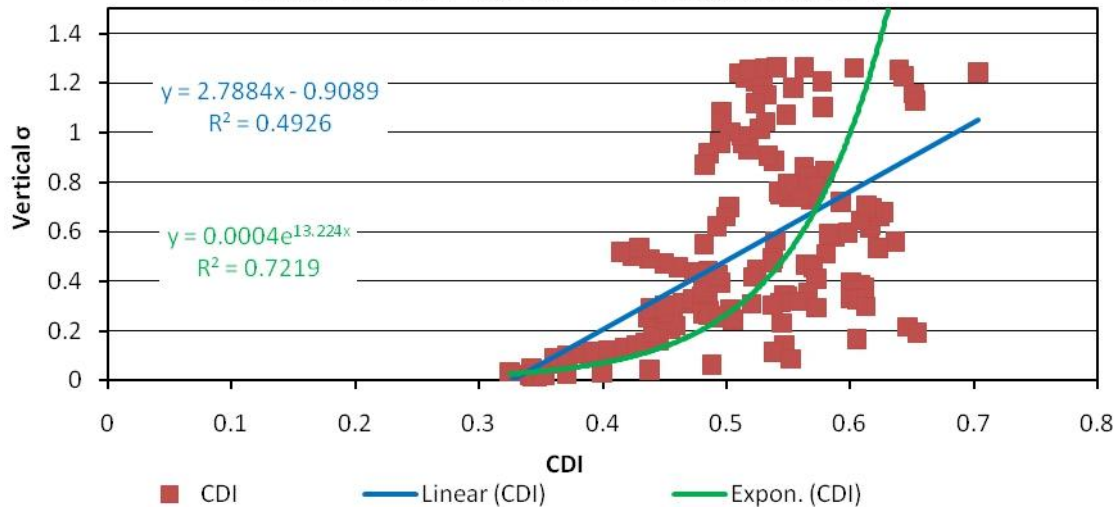
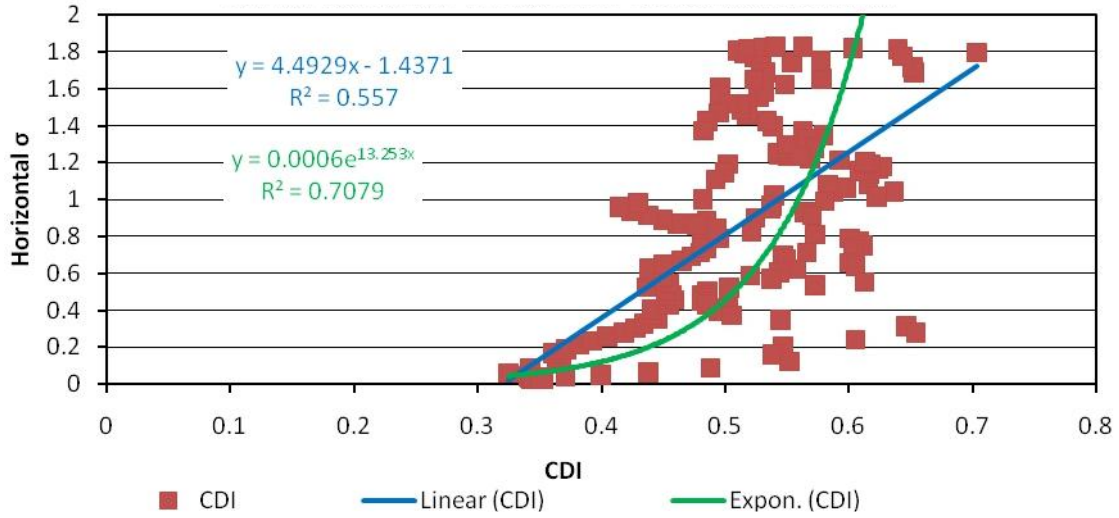


Figure 6-9. Plot of CDI results relative to tightly coupled position solution from ACMF test track 1. The exponential trend lines and corresponding R-squared values indicate the horizontal and vertical precisions are correlated with the CDI.

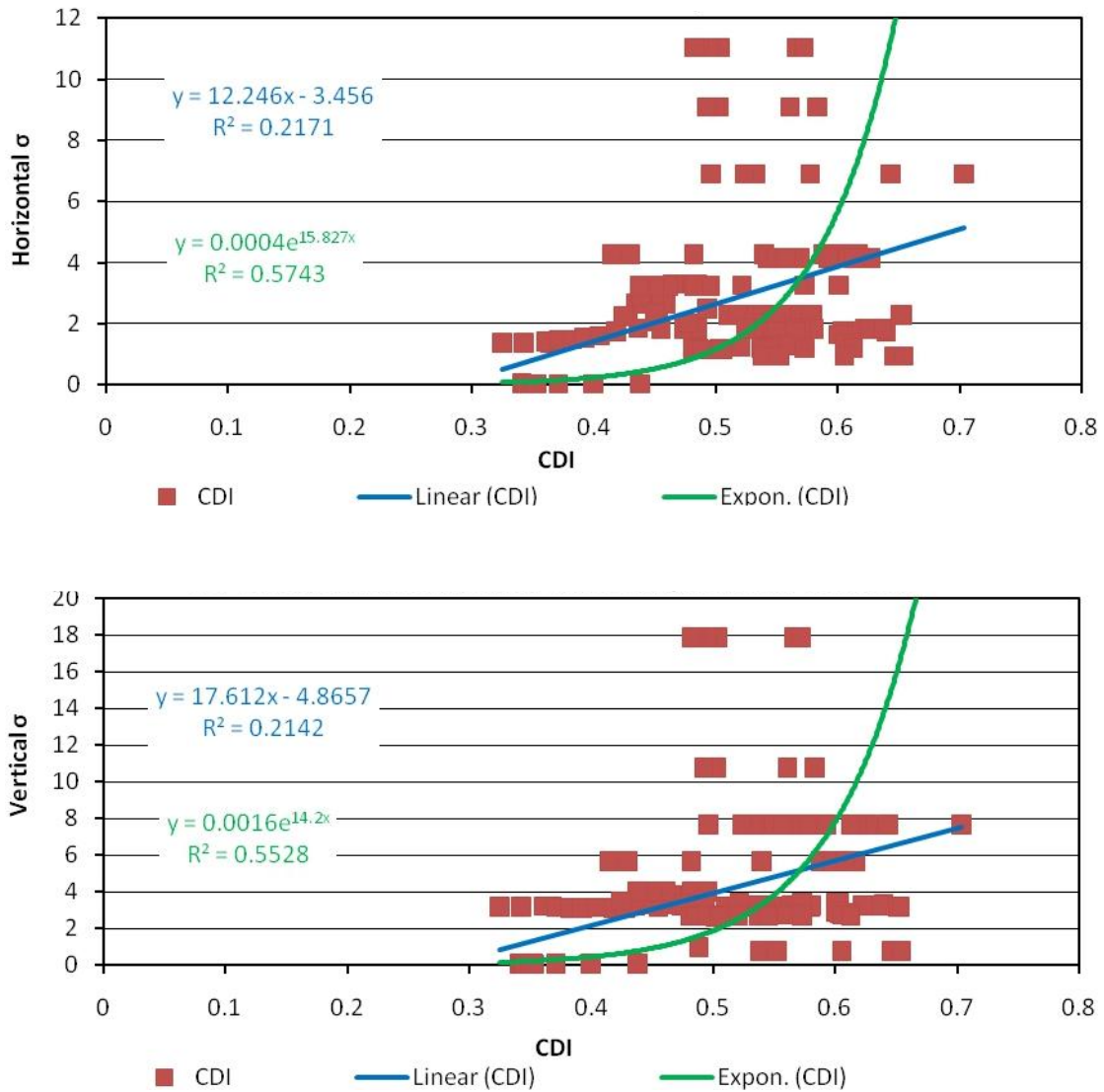


Figure 6-10. Plot of CDI results relative to GNSS-only position solution from ACMF test track 1. The linear trend lines indicate the horizontal and vertical precisions have minimal correlation with the CDI. Meanwhile the exponential trend lines between the CDI and positional precisions have some correlation.

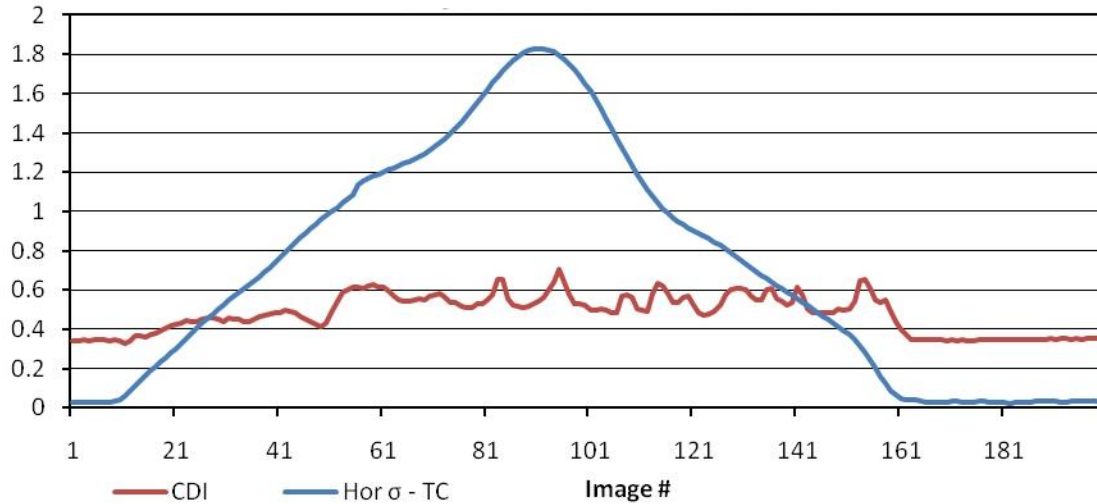


Figure 6-11. Plot of CDI results with tightly coupled positional solution precision from ACMF test track 1. The greatest precision was at the beginning and end of the test run. These small standard deviations can be attributed primarily to the long static initializations not the small relative decrease in canopy density.

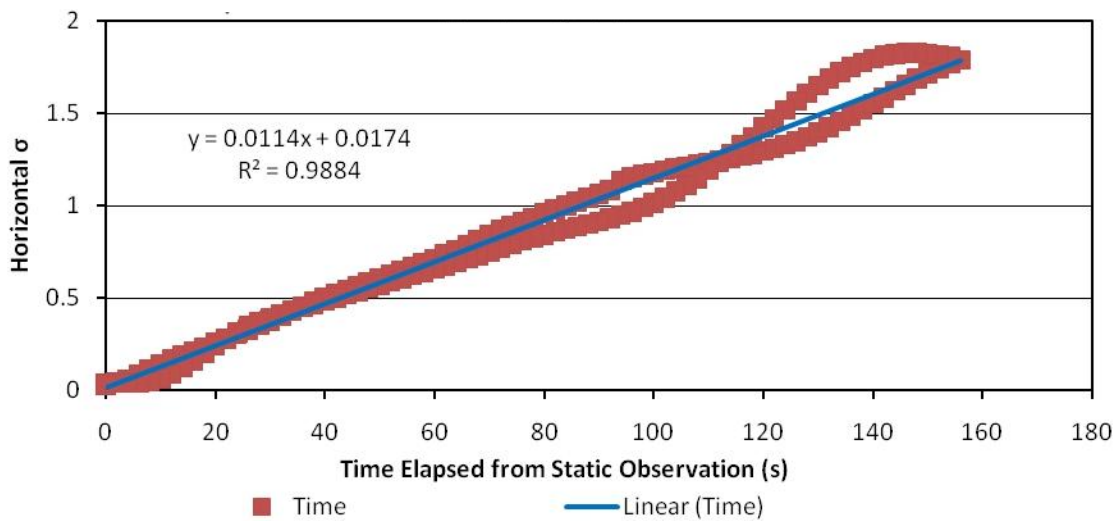


Figure 6-12. Plot of relationship between horizontal precision and time elapsed from static observation. The strong linear relationship between these two variables is substantiated by the correlation coefficient of nearly 1.

CHAPTER 7 GATORMMS: HORIZONTAL ORIENTATION FOR VISION-AIDING

7.1 GatorMMSv2.0 Application: Vision-Aiding

The previous chapter discussed canopy density analysis as the first application of GatorMMS technology. This chapter explores another GatorMMS application implemented in the Austin Cary Memorial Forest: vision-aiding (VA). VA is improving the georeferencing parameters of the navigation trajectory through imagery-derived exterior orientation parameter (EOP) updates. Recall georeferencing is the process of determining the time, position/location, and attitude/orientation of an event in space (Skaloud 1999). Thus, improving the precision and accuracy of the orientation parameters (OPK) and position parameters (XYZ of the incident nodal point of the lens) will help the final goal of accurately mapping features captured in the imagery.

Recall from Chapter 2 the discussion of VA and bundle adjustments (BA). The progression of any bundle adjustment is determining the interior orientation first, the relative orientation between two images in a stereo model second, and the absolute orientation of the stereo model in a mapping coordinate frame last. Using relative orientation between two images, the noise from the inertial navigation sensors can be reduced significantly through BA implementation. This noise reduction is seen through increased precision in the georeferencing orientation angles post-BA.

Common points between overlapping images are necessary for the creation of stereo models, the basis of photogrammetric bundle adjustments. These common points are also referred to as tie points or pass points. For VA implementation, accurate image space coordinates are necessary to ensure that the correct corresponding pass point features are used in the relative/absolute orientation. A multitude of least-squares

algorithms exist for minimizing errors in determining and matching points between images. Recall that PhotoModeler® 6 used centroid determination and least squares matching (LSM) on the camera calibration grid images. The Scale Invariant Feature Transform (SIFT) algorithm developed by Lowe has been used extensively in computer vision for automatically creating tie points between images (Lowe 1999). Pass point generation from aerial video imagery is another example of the growing research interest in automating these functions (Wilkinson et al. 2009).

The purpose of this GatorMMSv2.0 VA research is to develop a proof of concept in the forest. Thus, a manual approach to pass point generation is undertaken. Automatic pass point generation is a research opportunity to be explored in future studies.

7.2 ACMF VA Methods

7.2.1 Orientation

VA imagery was captured with the 24mm f/2.8D AF Nikkor® wide angle (WA) lens mounted on the horizontally oriented D200 Nikon® camera (Figure 3-6). The horizontal orientation means the widest portion of the camera sensor is aligned with the direction of travel. This feature is important for maximizing overlap between stereo images.

Relative to the 180° diagonal field of view (FOV) for the 8mm Pro-Optic® FE lens D200 camera combination, the horizontal FOV and vertical FOV for this VA camera-lens combination are approximately 51° and 35°, respectively. Between orienting the sensor horizontally, reducing vehicle speed, or increasing camera acquisition rates, maximum image overlap is crucial for creating usable stereo models.

7.2.2 ACMF VA Test Site

The test track for the GatorMMSv2.0 VA implementation in Figure 7-1 was chosen based on the dense canopy cover and existing network of ground control points (GCPs)

(Figure 4-2). From the Chapter 4 georeferencing system testing analysis, resurveying of the existing control was suggested due to discrepancies between the navigation trajectory and potential datum transformation errors in the original GPS network adjustment processing.

On March 3, 2011, six hour simultaneous static GPS observations of all six GCPs were conducted. The occupations were split into one hour observations and processed in Waypoint® GrafNet® software using the Gainesville airport CORS (GNVL) as the master control station. The UTM 17N WGS84 coordinates from the network adjustment are in Table 7-1.

To develop the VA proof of concept, high contrast targets were mounted to trees along test track 1. These VA targets featured in Figure 7-2 made manual target detection easier and represented a best case scenario for VA implementation. Furthermore, accurate and precise surveying of these targets could be accomplished with the well-defined cross from a Philips-head screw as the center point.

To concentrate VA implementation efforts, the southwestern portion of the approximately 550m test track 1 served as the focal VA testing area (Figure 7-3). Typical imagery acquired by the GatorMMSv2.0 in the vicinity of the VA test area is shown in Figure 7-4. A survey of this area was conducted with a reflectorless total station (TS) on February 25, 2010. Each VA target was surveyed with two sets of forward and reverse face readings from both GCP10 and CP50. Using Topcon Tools™ 7.2 (TT), the GCP coordinates from Table 7-1 were imported and held as control relative to the TS measurements. From the TT network adjustment, the UTM 17N WGS84 coordinates for the VA targets are in Table 7-2.

7.2.3 ACMF VA Procedure

To test if VA implementation can improve the reliability of the navigation trajectory for mapping purposes, the EOPs derived from self-calibrating bundle adjustments (SCBA) of the VA test area imagery are analyzed. The boresight-lever arm (BSLA) calibration parameters from Table 5-8 are input into WIE to determine the initial estimated image EOPs for the SCBA. Likewise, the target coordinates from Table 7-2 are SCBA inputs for the object space coordinates. These target coordinates are used as tie points not control points. The pre-adjustment EOP standard deviations generated by WIE and the post-adjustment EOP standard deviations generated by SCBUN are compared in an analysis of precision. Both ZUPT and non-ZUPT trials are used.

The primary limitation of this VA methodology is the need for approximations of the VA target object space coordinates. Knowing these coordinates is the primary drawback of using the collinearity equations in the SCBA for VA purposes. In Chapter 8, exploration of the coplanarity condition as the observation model for the BA is discussed. Initial object space coordinate approximations are not necessary for coplanarity condition implementation. Additional limitations of the ACMF VA target methodology are discussed in the results.

7.3 GatorMMS VA Results

On March 3, 2011, three trial runs of VA test track 1 commencing near GCP7 were conducted. During each run, the GatorMMSv2.0 ATV travelled between 5 and 10 miles per hour. Trial 1 and trial 2 were continuous non-ZUPT trajectories. Trial 3 was a ZUPT trial with zero velocity updates at each corner of the loop (SW near GCP10; SE near GCP9; NE near GCP8).

7.3.1 ACMF VA Non-ZUPT Trials

Twenty-three images of the VA test area along test track 1 were used in the SCBA for trial 1. Twelve VA targets were seen in at least 2 of the 23 images. Furthermore, each image had between 3 and 8 VA targets. Two additional images in the test area were unused due to image blur. The trial 1 shutter speed of 1/125s was much slower than the ideal speed of close to 1/1000s. Unfortunately, dark shadows under the forest canopy and a fixed aperture setting meant the only option for letting in enough light to the camera sensor was slowing the shutter speed.

After processing the GPS and inertial data as outlined in the georeferencing system testing recommendations from Chapter 4, the precision of the orientation parameters for the tightly coupled (TC) and smoothed inertial navigation trajectory of trial 1 is shown in Figure 7-5. The heading is the least precise orientation angle. When comparing the pre-adjustment and post-adjustment EOPs, the SCBA significantly improves the orientation precision in Figure 7-6. Recall from Figure 5-5 that heading/azimuth is related to the angle κ about the twice-rotated z-axis of the IMU. This axis corresponds to the angle ϕ about the once-rotated y-axis of the camera coordinate frame (CF). Thus, seeing the greatest improvement from VA implementation in the angle ϕ is expected.

VA implementation had similar positive results on the position precision of the smoothed TC navigation trajectory. Figure 7-7 shows the Easting-Northing-height (ENh) coordinate precision for the estimated nodal point of the camera lens along the entire trajectory. The half meter to meter precision is not suitable for many mapping operations. Thus, significant gains in position precision by almost two orders of

magnitude (m-level to mm-level precision) shown in Figure 7-8 were definitely encouraging.

To test the statistical significance of the improvement in the horizontal precision between pre-BA and post-BA, hypothesis testing of population variances was undertaken using the F-distribution. Hypothesis testing determined if the difference in the population variances of the two sample sets was statistically significant at a 99.9% level of significance. The results shown in Table 7-3 indicate the improvement in position and orientation precision is significant for all exterior orientation parameters.

$$H_0 \text{ (Null Hypothesis): } \frac{\sigma_{SCBA}^2}{\sigma_{WIE}^2} = 1 \quad (7-1)$$

$$H_A \text{ (Alternate Hypothesis): } \frac{\sigma_{SCBA}^2}{\sigma_{WIE}^2} < 1 \quad (7-2)$$

$$v_1, v_2 \text{ (Degrees of Freedom)} = 22 \quad (7-3)$$

$$\alpha = 0.001 \text{ (One-Tailed Test)} \quad (7-4)$$

$$\text{Test statistic: } F = \frac{\text{larger } S^2}{\text{smaller } S^2} \quad (7-5)$$

$$\text{Critical value from } F \text{ table: } F_{\alpha, v_1, v_2} = F_{0.001, 20, 20} = 4.29 \quad (7-6)$$

$$F \text{ (See table test statistics)} < F_{0.001, 20, 20} (4.29) \text{ False} \quad (7-7)$$

The null hypothesis H_0 can be rejected with a 0.1% probability of committing a Type 1 error (false positive) for all 6 parameters. Therefore, it can be said that the gains in precision from SCBA are both nonzero and significant.

After brightness analysis of the trial 1 imagery, the shutter speed was decreased to 1/200sec for trial 2. The goal was to minimize image blur of VA targets for accurate determination of image space coordinates. In trial 2, the same 12 VA targets were seen in at least 2 images. Likewise, 23 images were used in the SCBA. No images were omitted due to image blur. The trial 2 input EOP orientation precision was similar to trial 1. Meanwhile, trial 2 position precision was slightly better than trial 1. Figure 7-5 and Figure 7-7 are representative of the WIE smoothed TC navigation trajectory results for trial 2. Furthermore, Figure 7-9 and Figure 7-10 reinforce the approximately one order of magnitude position and orientation precision gains made during non-ZUPT trials.

Similar to trial 1, variance hypothesis testing showed the improvement in precision for each exterior orientation parameter was statistically significant. Table 7-4 summarizes these findings.

7.3.2 ACMF VA ZUPT Trial

Zero velocity updates (ZUPT) have been used in GPS outage prone areas to bound position and attitude errors in the inertial navigation trajectory. ZUPTs serve as a type of static reinitialization or alignment procedure. ACMF VA trial 3 had 3 ZUPTs during the course of the test track 1 loop. Prior to reaching CP50 in the southwestern VA test area (Figure 7-3), a 65 second ZUPT was implemented. The goal was to determine if gains in position and orientation precision from SCBA would still be significant relative to the more precise ZUPT navigation trajectory.

Analysis of the entire WIE smoothed TC navigation trajectory shows excellent position precision for each of the 3 ZUPTS. Furthermore, Figure 7-11 and Figure 7-12 show the maximum position and orientation standard deviations during trial 3 ATV

navigation are less than the maximum kinematic trial 1 or trial 2 EOP standard deviations.

Only kinematic images were used in the trial 3 SCBA. There were 9 kinematic VA test area images pre-ZUPT and 15 kinematic images post-ZUPT. The 66 static images during the ZUPT were omitted. Interestingly, 15 VA targets were visible in at least 2 images with 3 to 9 targets visible per image. As expected, Figure 7-13 shows similar heading precision gains for the SCBA results. Furthermore, Figure 7-14 shows that gains in input position precision are possible even right before and right after a ZUPT.

Using a critical F-statistic of 4.29, hypothesis testing on the pre and post SCBA EOP precisions in Table 7-5 confirmed the gains in EOP precision were statistically significant. This is similar to the results from the non-ZUPT ACMF VA Trials.

From this ACMF VA analysis, photogrammetric adjustments through VA are the most crucial tactical-grade inertial navigation supplement for aiding **heading** orientation angles both in the ZUPT and non-ZUPT trials.

7.3.3 ACMF VA Trials: Low-Accuracy H3 IMU

Another component of the ACMF VA analysis was comparing a low-accuracy MEMSense H3 IMU to the tactical-grade SPAN™ system (Figure 3-5). If the H3 could be used with results nearly equivalent to Novatel®'s SPAN™ system, then consumer costs would drop dramatically. This could lead to a subsequent rise in availability of this GatorMMS mobile mapping technology for forest managers.

Unfortunately, the implementation of VA with the H3 inertial navigation trajectory was not possible in these non-ZUPT or ZUPT trials. After overcoming the difficulty of processing the raw H3 inertial data in WIE, additional problems arose. WIE was incapable of aligning the H3 without transferring the alignment. The mean and standard

deviations for roll/pitch/yaw (RPY) during the long static initializations at the beginning and end of each trajectory were transferred as the forward and reverse alignment. When processing the inertial data, the model that WIE uses to weight the inertial and GPS observations was not sufficient at handling the drift associated with the low-accuracy H3 IMU. Figure 7-15 shows the erroneous trial 1 non-ZUPT smoothed LC position trajectory. The trajectory not only lacks the shape of test track 1 (Figure 7-1) but interpolation of the ATV speed from the trajectory at approximately 10m/s is approximately four times faster than the true speed. As a result, the precision and accuracy of the EOPs from the non-ZUPT trajectory were not reliable for VA without consistent position updates.

Initial analysis of the ACMF VA ZUPT trial 3 was encouraging. The relative position of all static time intervals resembled the location of the test track 1 loop (Figure 7-16). Since the ZUPT in the southwest corner was at the VA test area, there was potential that VA implementation using SCBA was feasible. Upon looking at the smoothed LC EOP trajectory for trial 3, it was apparent that the rapid deterioration of the coordinate quality and wild fluctuations in the OPK angles was not suitable for SCBA. The OPK angles seemed to suggest the dynamics of the ATV were similar to that of a fighter jet. Upon SCBA implementation, the adjustment failed.

7.4 GatorMMS VA Lessons Learned

Vision-aiding using photogrammetric adjustments can be implemented in the forest given certain conditions. Thus far, VA implementation conditions include preprocessing of the inertial navigation trajectory, knowledge of control point/target coordinates, use of artificial VA targets, access to a tactical-grade IMU, and robust proprietary software for inertial processing. To implement vision-aiding for near real-time

applications, the system must be capable of integrating GPS, inertial, and image updates sequentially on the fly. Thus, knowledge of absolute control point targets must not be a necessity. The development of a vision-aiding algorithm from an aerial platform that satisfies these requirements is discussed further in Chapter 8.

For the GatorMMSv2.0, issues existed that provided valuable lessons for future forest GatorMMS VA implementation including guidance on algorithm development. First, knowing absolute control point coordinates for mapping operations is not feasible on a large scale whether in a forest or urban landscape. Thus, direct georeferencing must provide the position and orientation updates.

Tracking targets in shadowed areas without distinct features from the built environment is a difficult and complex task. Testing the reliability of existing pass point generating algorithms under forest canopy is a research area in need of future study.

Additionally, deciding the best shutter speed at the beginning of a mobile mapping operation under forest canopy is difficult due to shifting shadows and highly variable lighting along the trail. Decisions should be based on the canopy density (i.e. shadows) of the most important areas.

For future terrestrial algorithm development, consideration must be paid to the difference in base-to-height ratio between aerial photogrammetry and close-range terrestrial photogrammetry. Objects in the background will pass behind foreground objects throughout a strip of photos. This property could complicate the automatic pass point generating software. The use of a camera with a frame rate greater than 1Hz could limit large geometric differences between sequential images.

Additional inertial sensors could help the low-accuracy H3 IMU navigation trajectory. A magnetic compass or a dual antenna GPS receiver for heading updates could help resolve the lack of azimuthal precision. Odometer updates could also help with velocity updates and dampen errors associated with gyro drift.

Lastly, accurately calibrating imagery for the radial distortion in FE lenses could aid the difficulty often encountered with image feature overlap in terrestrial MMS operation from typical wide angle lens. The FE FOV captures a broader view of the area leading to greater redundancy of common pass points. This is assuming that the coordinates of each pass point can be accurately captured in spite of the reduced resolution of each feature in the image.

Table 7-1. VA test area ground control point coordinates in UTM 17N WGS84. The coordinates for GNVL are published by the National Geodetic Survey (NGS). Thus, the default coordinate precision horizontally and vertically is 0.000m.

Station	Easting (m)	Northing (m)	H-Ell (m)	σ - Hor (m)	σ - Ver (m)
GNVL	376457.773	3284735.156	22.425	0.000	0.000
CP50	382414.526	3290286.258	16.108	0.007	0.011
GCP10	382399.897	3290285.729	15.997	0.007	0.011
GCP4	382380.698	3290441.226	17.311	0.007	0.011
GCP7	382357.859	3290442.814	17.357	0.007	0.010
GCP8	382545.217	3290376.449	16.886	0.007	0.011
GCP9	382538.835	3290287.678	16.090	0.007	0.011

Table 7-2. VA test area target coordinates in UTM 17N WGS84. The horizontal and vertical precision of the coordinates reflect the precision of the TS measurements. The precision of the GPS coordinates was not propagated through to the VA targets due to limitations within the TT software.

Station	Easting (m)	Northing (m)	H-Ell (m)	σ - Hor (m)	σ - Ver (m)
5	382426.871	3290275.157	18.120	0.007	0.002
6	382432.339	3290283.814	18.787	0.007	0.003
7	382427.220	3290291.590	17.888	0.005	0.002
8	382433.750	3290295.504	18.092	0.005	0.002
9	382432.572	3290304.570	18.383	0.005	0.002
10	382434.883	3290313.943	18.597	0.005	0.002
11	382426.823	3290311.884	18.872	0.005	0.002
12	382420.172	3290319.260	18.776	0.005	0.002
13	382415.302	3290315.752	18.844	0.005	0.002
14	382408.753	3290315.497	18.844	0.005	0.002
15	382405.451	3290318.787	20.665	0.005	0.002
16	382410.478	3290310.438	18.610	0.004	0.002
17	382414.510	3290304.015	18.940	0.004	0.002
18	382413.691	3290300.875	20.423	0.004	0.002
19	382419.347	3290297.611	18.318	0.004	0.002
20	382424.071	3290298.848	18.352	0.005	0.002
21	382419.079	3290290.537	17.737	0.004	0.002

Table 7-3. Hypothesis testing of population variances for VA trial 1. All exterior orientation parameters had statistically significant improvements in precision through the implementation of SCBA.

Exterior Orientation Parameter	<i>F (Test Statistic)</i>
Omega (σ)	16.49
Phi (σ)	1541.42
Kappa (σ)	6.49
Easting (σ)	31.22
Northing (σ)	51.29
Height (σ)	59.96

Table 7-4. Hypothesis testing of population variances for VA trial 2. With a critical F test statistic, all exterior orientation parameters had statistically significant improvements in precision through the implementation of SCBA with a 99.9% level of confidence.

Exterior Orientation Parameter	<i>F (Test Statistic)</i>
Omega (σ)	12.01
Phi (σ)	1080.22
Kappa (σ)	6.37
Easting (σ)	24.76
Northing (σ)	42.92
Height (σ)	46.33

Table 7-5. Hypothesis testing of population variances for VA trial 3. All exterior orientation parameters had statistically significant improvements in precision through the implementation of SCBA with a 99.9% level of confidence.

Exterior Orientation Parameter	<i>F (test statistic)</i>
Omega (σ)	25.73
Phi (σ)	2467.48
Kappa (σ)	17.71
Easting (σ)	43.31
Northing (σ)	112.73
Height (σ)	133.47

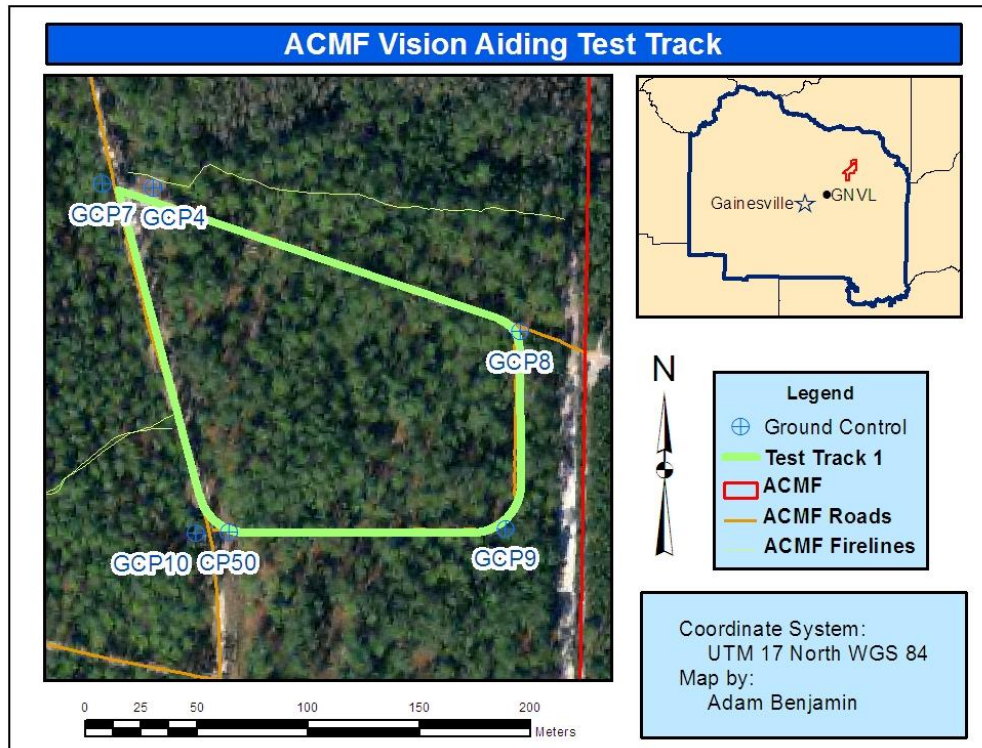


Figure 7-1. ACMF VA test track. Test track 1 from Figure 6-4 is the subject area for testing the VA implementation of the GatorMMSv2.0. All VA targets were surveyed from GCP10 and CP50 using GCP9 as a backsight.



Figure 7-2. ACMF VA field setup. The left image is a detail of the high contrast VA targets. Each VA target consists of a white Phillips-head screw inside black and white concentric washers mounted to a 4in by 4in square of black aluminum flashing. The original silver materials are spray painted black and white for maximum contrast. The right image is the typical setup for fixing the targets to the mature pine trees in the VA test area. (images courtesy of author)

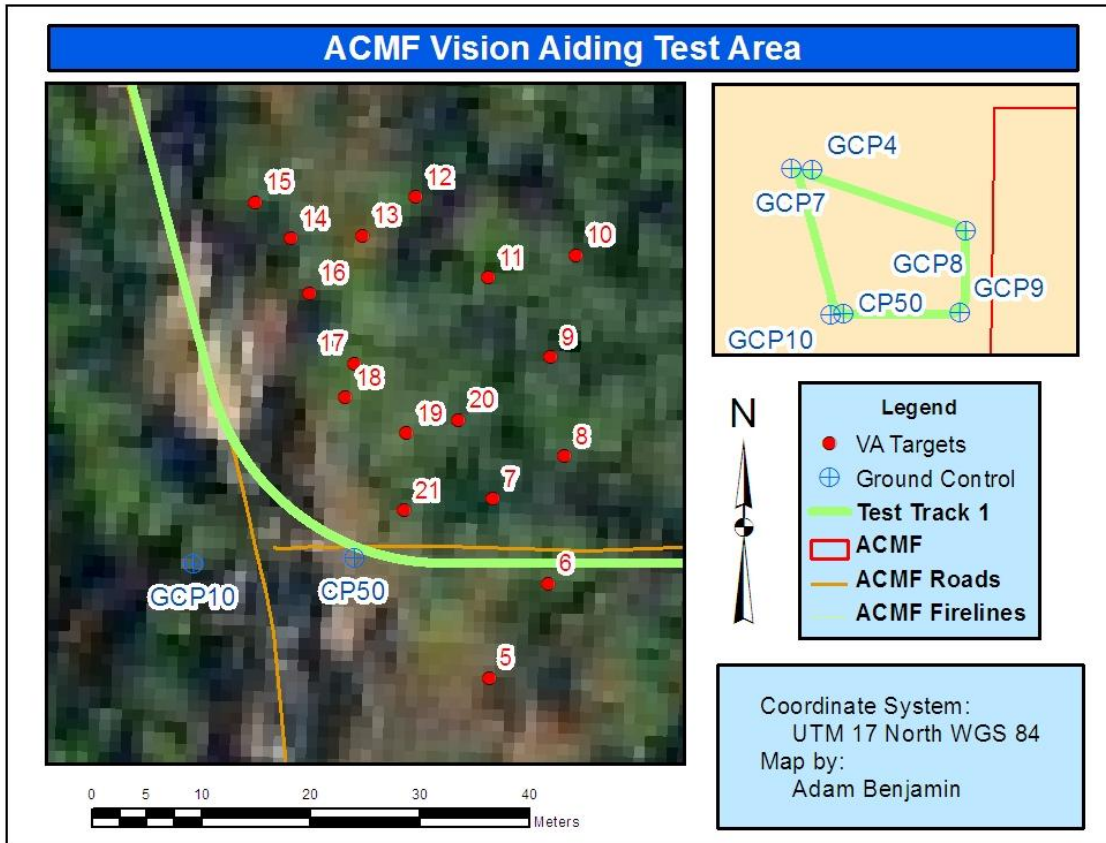


Figure 7-3. ACMF VA test area. The southwestern portion of test track 1 shows the excellent VA test area depth of field. VA target 10 was the most difficult target to locate due to consistent shadows under the dense forest canopy.



Figure 7-4. Typical image of ACMF VA test area. This example of a typical VA image represents that the entire field of targets was never captured in one image. Also, target features in the shadowed background would be difficult to track without the high contrast targets. (image courtesy of author)

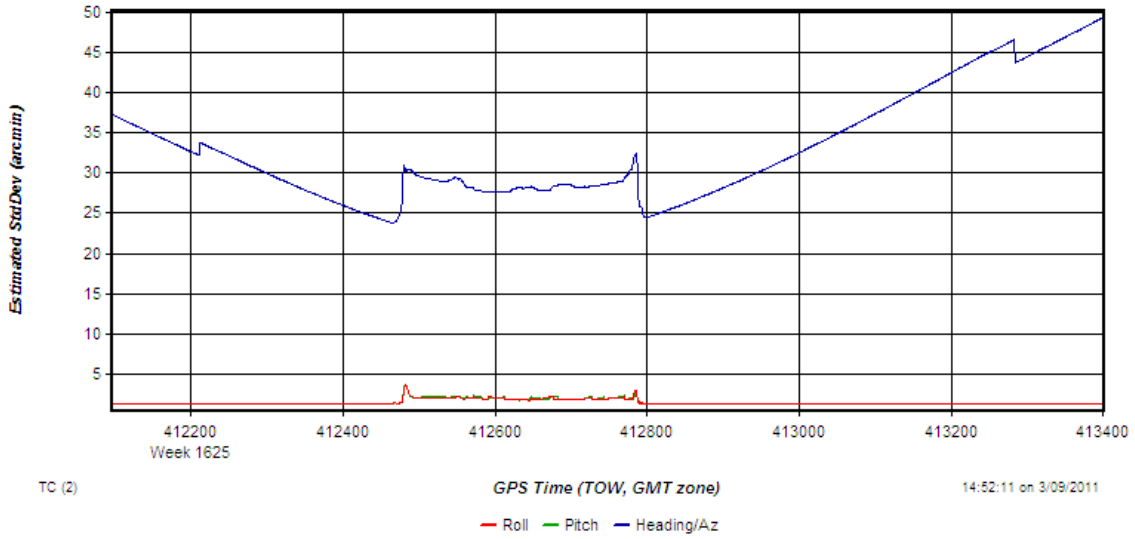


Figure 7-5. Estimated orientation angle precision for trial 1. After smoothing the TC trajectory, heading is the orientation angle which needs the greatest improvement.

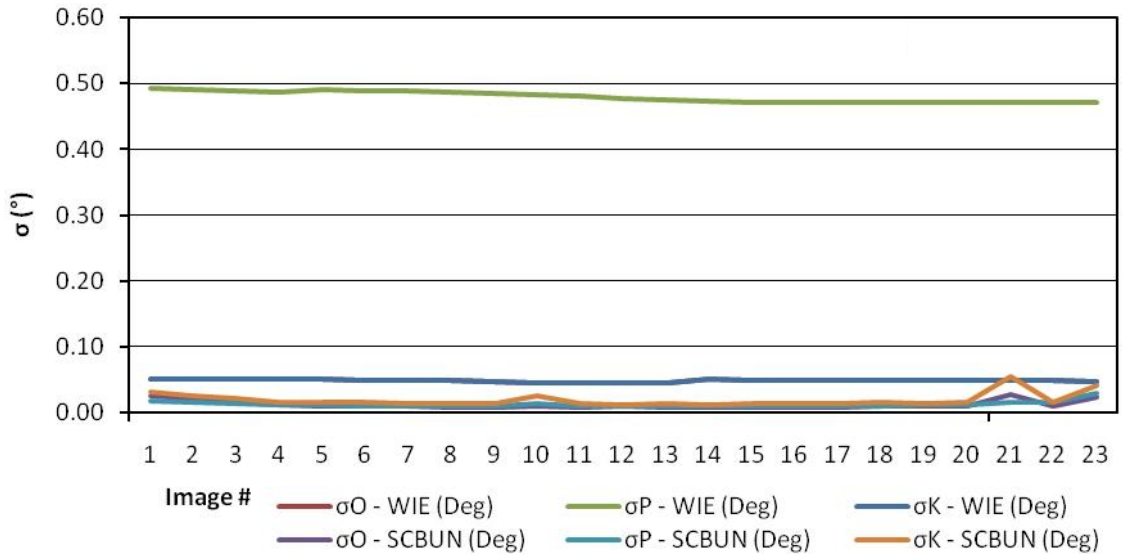


Figure 7-6. Comparison of pre-SCBA & post-SCBA orientation angle precision for trial 1. Heading, which corresponds with the angle phi in the camera coordinate frame, improved by one order of magnitude due to VA implementation.

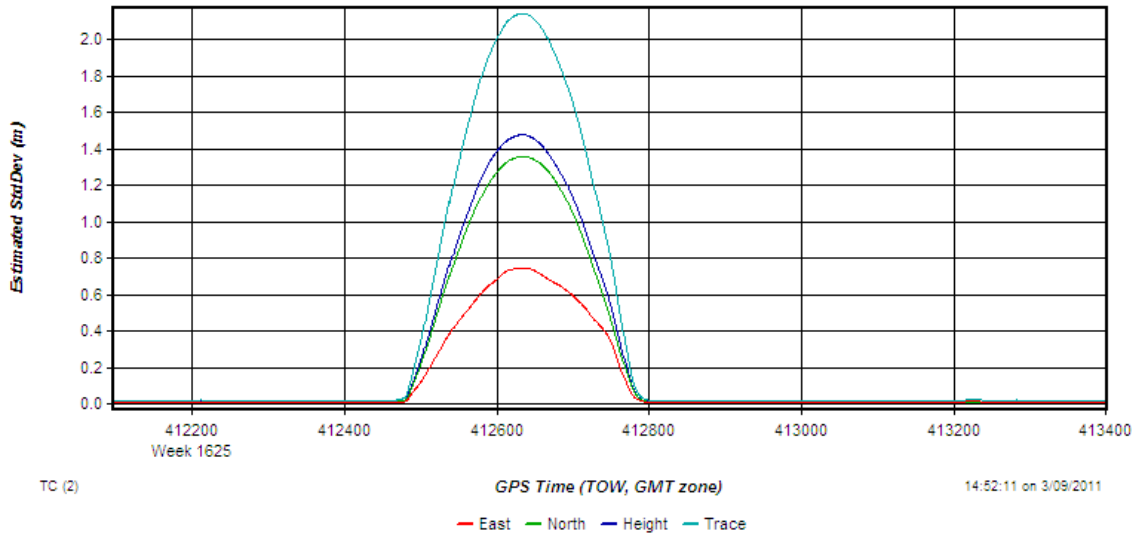


Figure 7-7. Estimated position precision for ACMF VA trial 1. The $\pm 1\text{m}$ positional coordinate standard deviations are not suitable for survey-grade mapping.

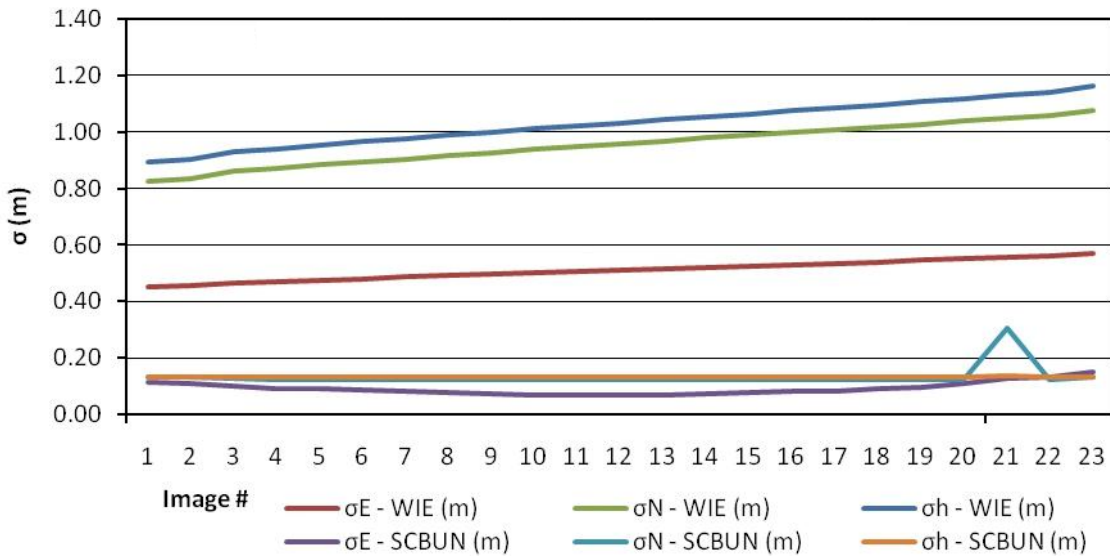


Figure 7-8. Comparison of pre-SCBA & post-SCBA position precision for ACMF VA trial 1. The original $\pm 1\text{m}$ positional coordinate standard deviations were improved drastically by approximately one order of magnitude.

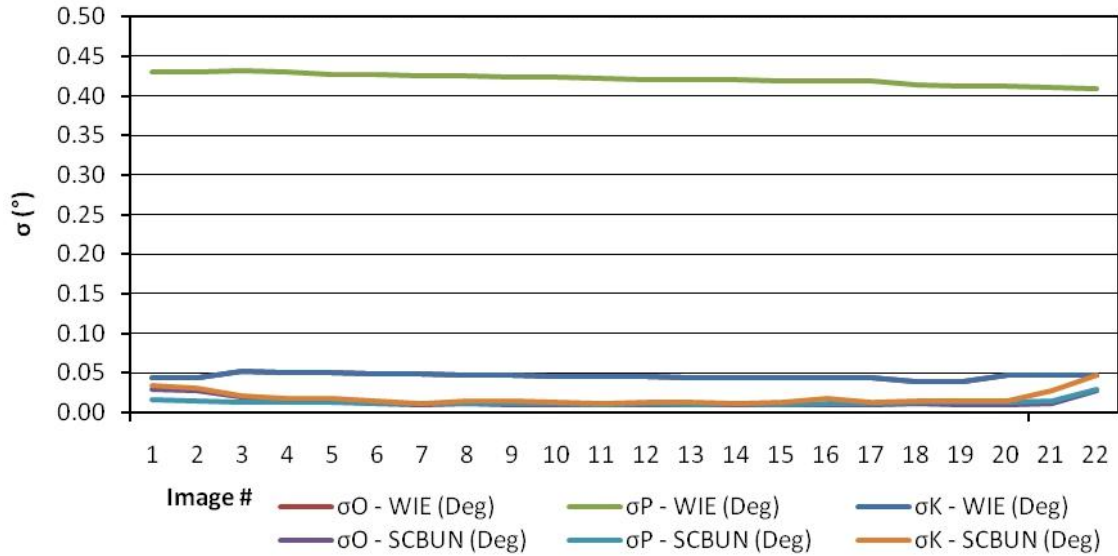


Figure 7-9. Comparison of pre-SCBA & post-SCBA orientation angle precision for trial 2. Again, SCBA successfully resolved the lack of precision for heading with a one order of magnitude precision increase in phi. The increase in EOP standard deviations at either end of the bundle adjustment strip is common for BA. Beyond the beginning and end of a subject area, images are often captured for the adjustment but not used for mapping purposes due to lack of precision at the edges.

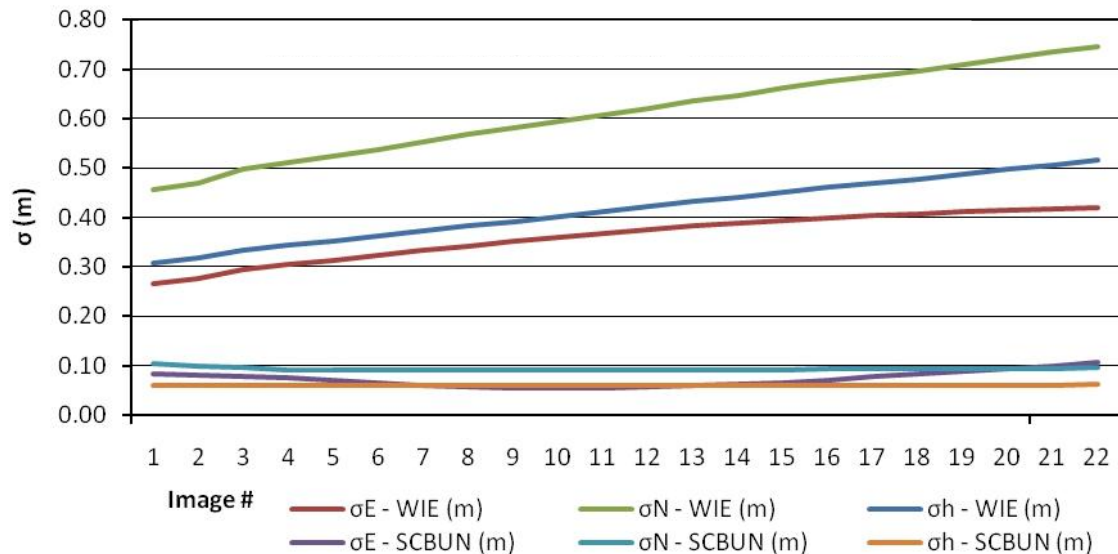


Figure 7-10. Comparison of pre-SCBA & post-SCBA position precision for ACMF VA trial 2. Again, the original $\pm 0.5\text{m}$ positional coordinate standard deviations were improved drastically by approximately one half order of magnitude.

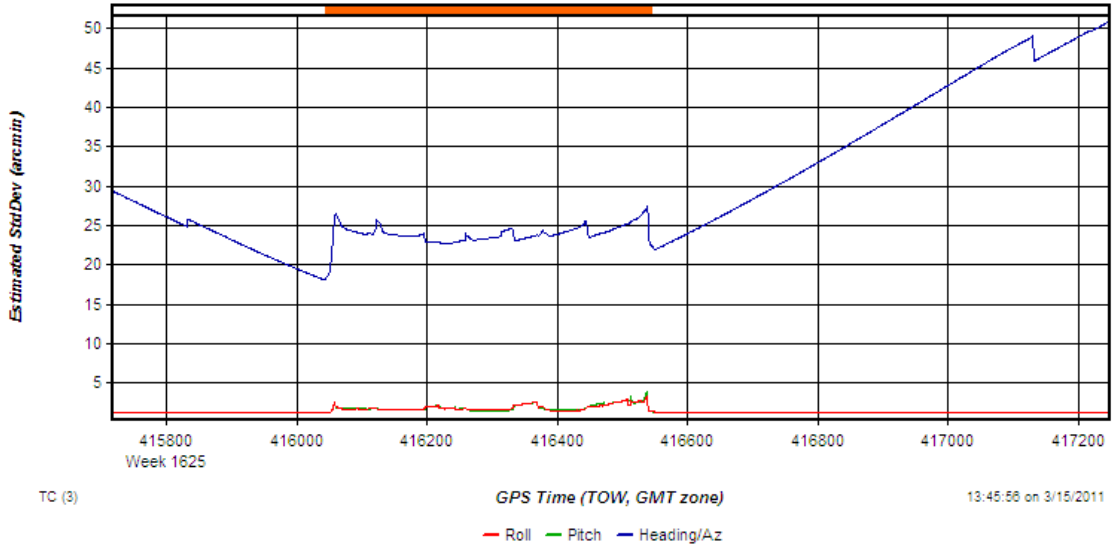


Figure 7-11. Estimated orientation angle precision for ACMF VA trial 3. Heading from the smoothed TC navigation trajectory is still the least precise orientation angle. However, the average heading precision for the kinematic period is less than a similar average for the non-ZUPT trials.

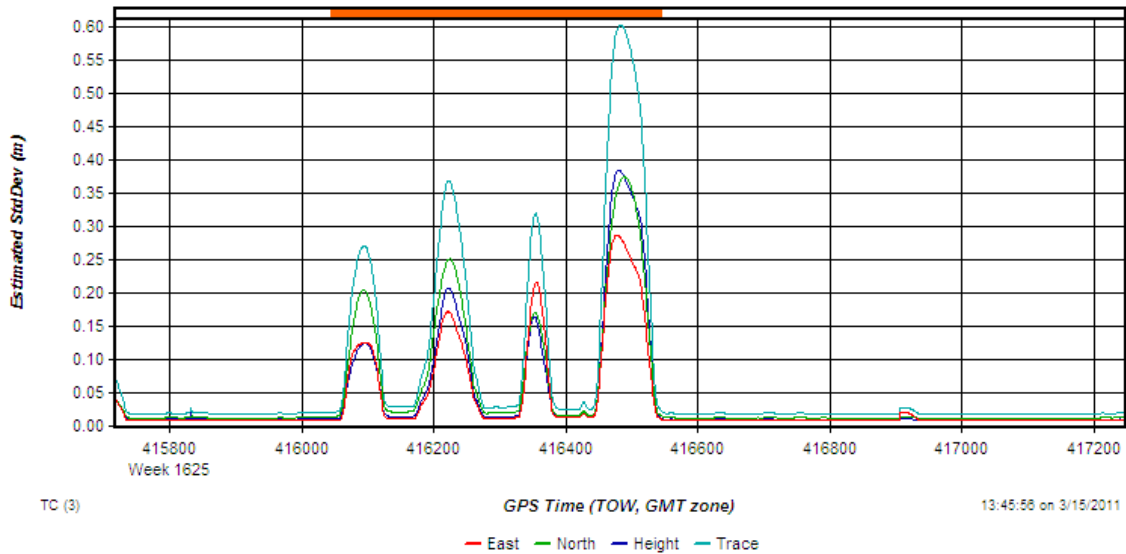


Figure 7-12. Estimated position precision for ACMF VA trial 3. The ZUPTs had the greatest impact on the positional coordinate standard deviations through bounding positional errors. The ZUPT intervals are shown above as troughs.

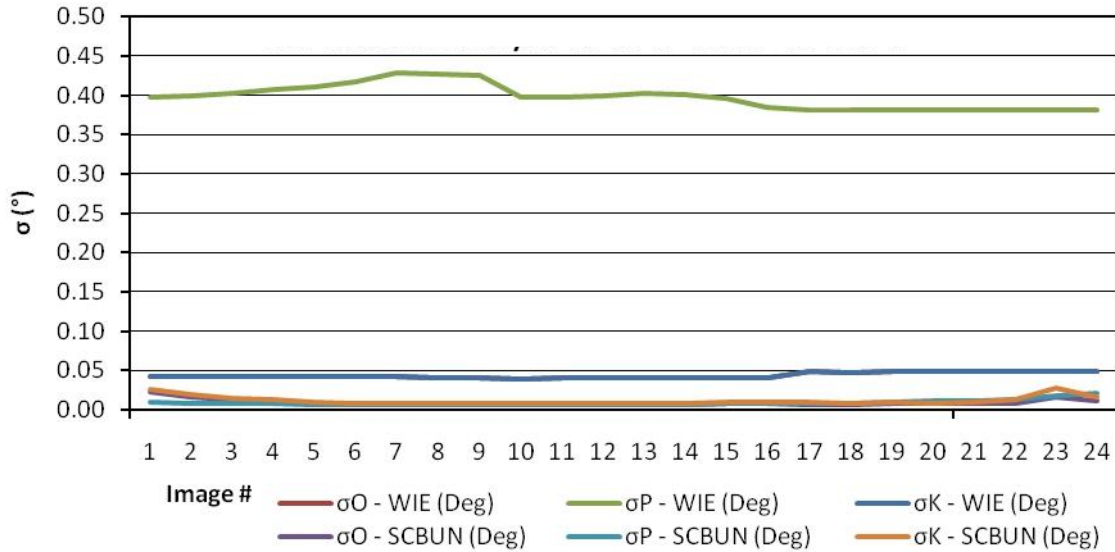


Figure 7-13. Comparison of pre-SCBA & post-SCBA orientation precision for ACMF VA trial 3. The gains in orientation precision, especially heading, are similar to the non-ZUPT trials.

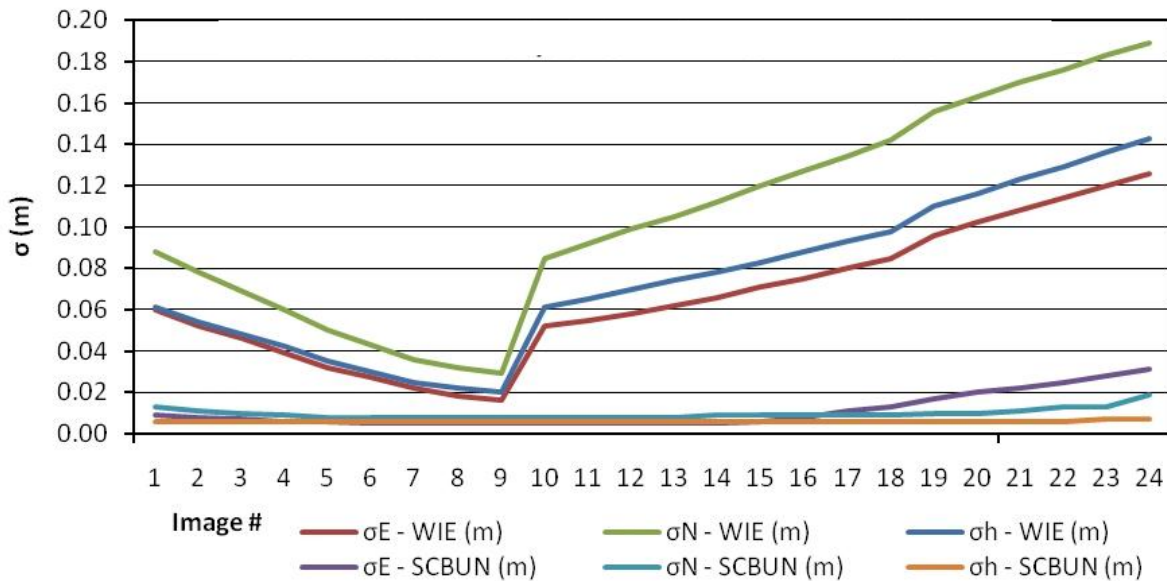


Figure 7-14. Comparison of pre-SCBA & post-SCBA position precision for ACMF VA trial 3. Images 1 through 9 are pre-ZUPT and images 10-24 are post-ZUPT. While the initial cm-level and low dm-level precision was already suitable for some mapping applications, further refinement of the position precision is possible through photogrammetric adjustments for survey-grade mapping.

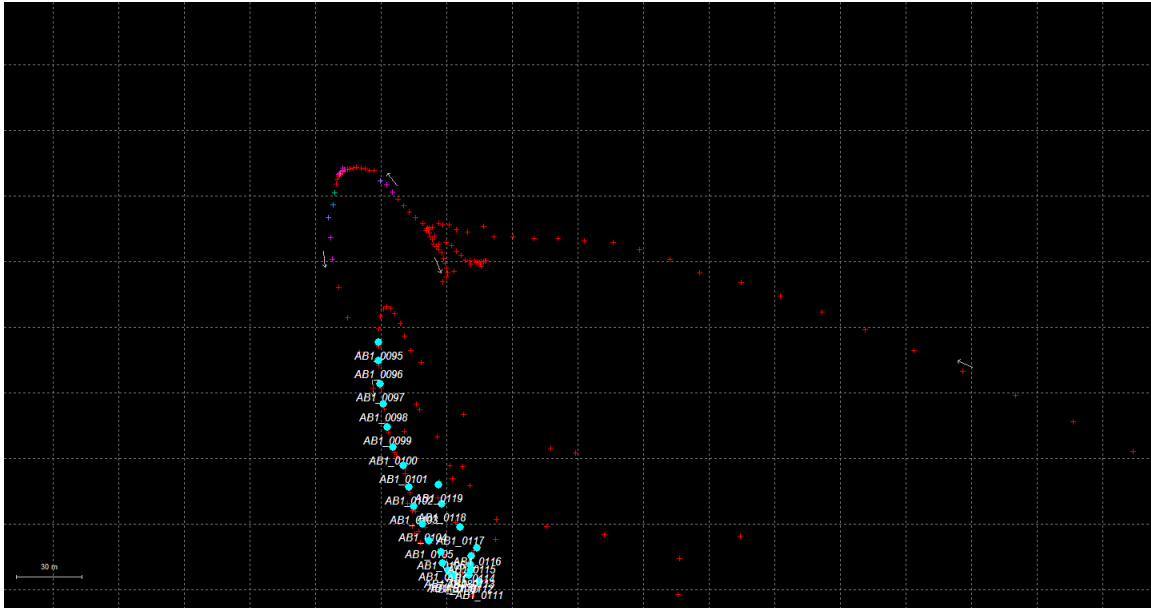


Figure 7-15. Low-accuracy H3 IMU inertial trajectory from ACMF VA trial 1. The trajectory does not resemble the test track 1 loop except at the northwestern corner (the point of static alignment). Each square represents 30m x 30m of horizontal ground distance. Through interpolation of three camera events per square, the trajectory shows the vehicle was traveling 4 times faster than the true $\pm 2.5\text{m/s}$ vehicle speed. Furthermore, the position precision from this trajectory was as high as 200m during kinematic operation under the forest canopy (Figure not shown).

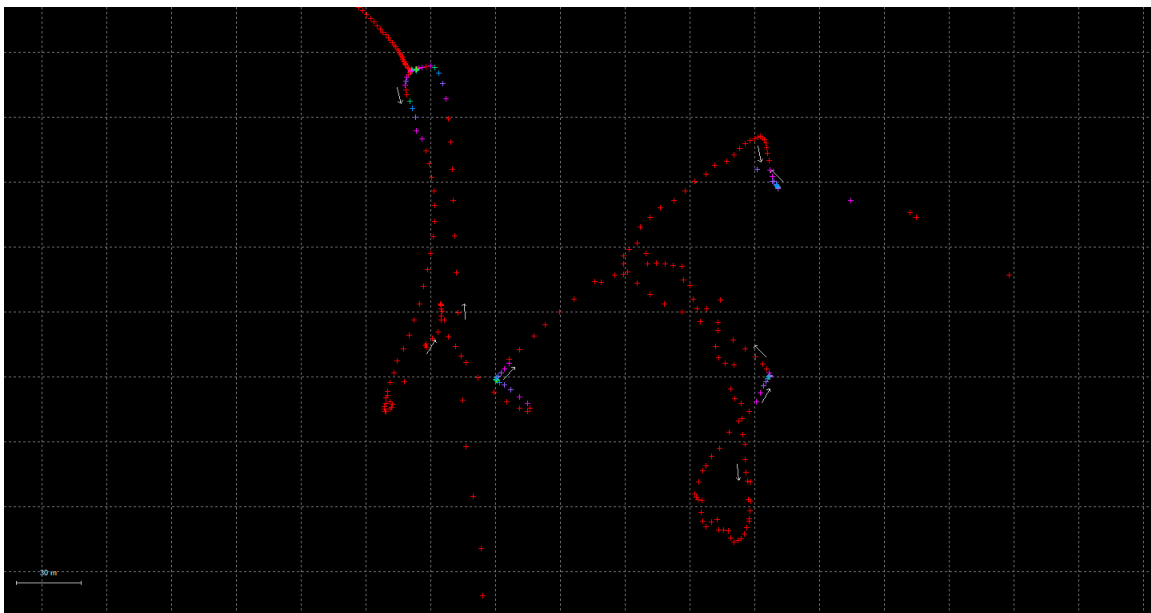


Figure 7-16. Low-accuracy H3 IMU inertial trajectory from ACMF VA trial 3. The four light blue areas represent the increased position quality at the static ZUPT interval locations. The lack of quality GPS positions under the tree canopy made WIE rely on the low accuracy IMU for inertial navigation position updates. As a result, the position precision was quite poor.

CHAPTER 8 SEQUENTIAL VISION-AIDING

8.1 Theoretical Framework

This research analyzes Kalman filtering with an optimal smoother in sequential bundle adjustment as a method for reducing the sequential accumulation of error normally associated with aerial triangulation in order to provide accurate and precise georeferencing parameters. The goal is to apply the sequential bundle adjustment algorithm developed herein to the terrestrial GatorMMS forest application in the future.

8.1.1 Kalman Filtering

The Kalman filter is an algorithm that implements a predictor-corrector estimator to minimize the estimated error covariance of the state (Gelb 1974). The filter achieves that by utilizing knowledge of system and measurement dynamics, assumed statistics noises and measurement errors, and initial condition information (Gelb 1974). Kalman filtering is the most common technique for estimating the state of a linear system and is widely used in many applications such as navigation with INS-GPS systems (Nassar et al. 2007; Webb 2007), satellite orbit prediction (Xiong et al. 2009), and in many other fields.

The objective of the Kalman filter is to obtain the system state estimate \hat{x}_k (a *posteriori* state estimate) as a linear combination of a predicted estimate \hat{x}_k^- (a *priori* estimate) and a weighted difference between an observation z_k and a measurement prediction ($H\hat{x}_k^-$). In equation form,

$$\hat{x}_k = \hat{x}_k^- + K(z_k - H\hat{x}_k^-) \quad (8-1)$$

where K is the Kalman gain that minimizes the *a posteriori* error covariance, $(z_k - H\hat{x}_k^-)$ is the measurement innovation or residual, and H is the coefficient matrix that relates the state estimate \hat{x}_k^- to the observation z_k .

Interested readers are referred to Appendix B or Kalman filtering texts (i.e., Kalman 1960; Rauch et al. 1965; Gelb 1974; Welch and Bishop 2001) for details of the algorithm.

8.1.2 Coplanarity Condition

The coplanarity condition is used as the observation model in the Kalman filter algorithm. If two photographs are relatively oriented with respect to each other, then the object space rays defined by a pair of conjugate image points and their respective exposure stations will intersect at exactly one point (Wolf and Dewitt 2000; Mikhail et al. 2001). The object space position of that point occurs at the intersection. The two object space rays in combination with the position vector connecting the two exposure stations form the three sides of a triangle. This triangle defines the plane satisfied by the condition illustrated in Figure 8-1 modified after Mikhail et al. (2001).

The coplanarity condition is based on the fact that the volume (V) of the parallelepiped (a polyhedron consisting of all parallelogram faces) of three coplanar vectors will be 0 as shown in Equation 8-2.

$$V = |\vec{b} \cdot (\vec{a}_1 \times \vec{a}_2)| = \begin{vmatrix} b_x & b_y & b_z \\ u_1 & v_1 & w_1 \\ u_2 & v_2 & w_2 \end{vmatrix} = 0 \quad (8-2)$$

As illustrated in Figure 8-1, the base vector between the two exposure stations is (\vec{b}) . Vectors, (\vec{a}_1) and (\vec{a}_2) , are the object space rays originating from the exposure

stations through their respective conjugate image points to the common object space point. Each exposure station is represented by its object space coordinates (X_L, Y_L, Z_L) .

In order to further develop the observation model, the coplanarity condition takes the observation equation form in Equation 8-3 (Mikhail et al. 2001).

$$Z_e = [x_1 \quad y_1 \quad z_1] F \begin{bmatrix} x_2 \\ y_2 \\ z_2 \end{bmatrix} = 0 \quad (8-3)$$

where Z_e is the equivalent observation, and C is the fundamental matrix that contains the exterior orientation parameters (EOPs) and the interior orientation parameters (IOPs) of both images in the stereo-model, and expressed as:

$$F = C_1^T M_1 K_b M_2^T C_2 \quad (8-4)$$

where C is the calibration matrix of the interior orientation parameters:

$$C = \begin{bmatrix} 1 & 0 & -x_0 \\ 0 & 1 & -y_0 \\ 0 & 0 & -f \end{bmatrix} \quad (8-5)$$

K_b is the skew-symmetric matrix of the base vector information between the two exposure stations:

$$K_b = \begin{bmatrix} 0 & -b_z & b_y \\ b_z & 0 & -b_x \\ -b_y & b_x & 0 \end{bmatrix} \quad (8-6)$$

and M_i is the rotation matrix of image i in the stereo pair

$$M_i^T = \begin{bmatrix} m_{11} & m_{21} & m_{31} \\ m_{12} & m_{22} & m_{32} \\ m_{13} & m_{23} & m_{33} \end{bmatrix}_i \quad (8-7)$$

The components of these matrices, as well as the details of the coplanarity equations, are discussed in photogrammetry books (i.e., Wolf and Dewitt 2000; Mikhail et al. 2001). Appendix C describes the coplanarity condition in further detail including the linearization of the coplanarity condition necessary for implementing this observation model.

8.2 Methods

8.2.1 Dynamics Model

Kalman filtering requires a dynamics model to transition between epochs. Simplification of the dynamics model was desired to isolate the impact that the observation model had. Thus, certain assumptions were made that affected the time update equations in the Kalman filter algorithm. First, it was assumed that the *a priori* state estimate (\hat{x}_k^-) and its covariance matrix (P_k^-) are equal to the *a posteriori* state estimate from the previous epoch (\hat{x}_{k-1}) and its covariance matrix (P_{k-1}). Thus, the original linear discrete-time controlled process Kalman filter equation mentioned earlier is simplified from:

$$\hat{x}_k^- = \hat{x}_{k-1} \quad (8-8)$$

In a similar fashion,

$$P_k^- = P_{k-1} \quad (8-9)$$

8.2.2 Observation Model

The objective of this research is to test the coplanarity condition as the observation model for a Kalman filtering approach to solving for the georeferencing parameters (EOPs). Given the dynamics model above, the measurement update equation for the Kalman gain (K_k) is written in Equation 8-10 as

$$K_k = P_k^- H^T (H P_k^- H^T + R_e)^{-1} \quad (8-10)$$

where R_e is the equivalent measurement noise covariance matrix formed by the measurement noise covariance matrix R and the Jacobian matrix of the coplanarity equation with respect to the image point observations B .

$$R_e = B R B^T \quad (8-11)$$

Likewise, the observation z_k is equivalent to Z_e from the linearized form of the coplanarity equation. Substituting into the second discrete Kalman filter measurement update equation yields the *a posteriori* state estimate in Equation 8-12:

$$\hat{x}_k = \hat{x}_k^- + K(Z_e - H\hat{x}_k^-). \quad (8-12)$$

By integrating these assumptions with the observation model modifications, the process of Kalman filtering can be investigated via simulation. In order to make the exterior orientation parameter solution more robust than a simple forward filtering process, an optimal smoothing technique is implemented.

8.2.3 Optimal Smoothing

Optimal smoothing does not require an observation model. Thus, reimplementation of the coplanarity condition observation equation is not necessary.

Smoothing is a function of stochastic weighting only. It is a post-mission processing scheme that uses all measurements from the initial epoch to a time N to estimate a system state x_k^s at epoch k such that $0 \leq k \leq N$. Note that the *a priori* and *a posteriori* system state estimates as well as the *a priori* and *a posteriori* covariance estimates from the forward Kalman filtering process are stored for each epoch between 0 and N . These estimates then form the basis of the backward smoothing operation. In theory, backward optimal smoothing accounts for the shortcoming of the forward filtering algorithm by achieving an optimal solution equivalent to the simultaneous batch processing of all the data.

While near real-time processing is desired, the initial implementation of this algorithm is to simplify the model as much as possible without sacrificing optimization. There are three main types of optimal smoothers: fixed interval, fixed point, and fixed lag. This model implements a fixed-interval smoothing algorithm called the Rauch-Tung-Striebel (RTS) backward smoother. The RTS smoother is the least complex fixed-interval optimal backward smoother (Gelb 1974; Nassar et al. 2007).

The backward sweep of the RTS commences at the culmination of the forward Kalman filter sweep. At this point, the initial smoothed system state estimate x_{k+1}^s is equal to the *a posteriori* system state estimate \hat{x}_N . Likewise, the initial smoothed covariance estimate P_{k+1}^s is equal to the *a posteriori* system state estimate P_N . The smoothed system state estimate x_k^s at time k in the RTS algorithm (Rauch et al 1965) is:

$$x_k^s = \hat{x}_k + D_k(x_{k+1}^s - \hat{x}_{k+1}^-) \quad (8-13)$$

where D_k is the smoothing gain matrix (similar to the Kalman gain matrix from the forward filtering process),

$$D_k = P_k I (P_{k+1}^-)^{-1} \quad (8-14)$$

Note that the covariance matrix of the smoothed estimates P_k^s in Equation 8-15 is not necessary for computing the smoothed system state estimate in our case. However, analysis of that covariance matrix was deemed necessary for determining the relative precision of the algorithm:

$$P_k^s = P_k - D_k (P_{k+1}^- - P_{k+1}^s) D_k^T \quad (8-15)$$

8.3 Experimental Results

8.3.1 Simulation Model

In order to test the functionality of this algorithm, a simulation model was created to mimic imagery acquisition over a predetermined flight path. While the end goal is the utilization of this algorithm with thousands of images per flight, the initial simulation model was a strip of 500 photographs. We assume the photographs have been previously calibrated and corrected for all distortions. Over this minimal strip of images, both the forward filter and the backward optimal smoother could be seen converging on a steady-state solution. Thus, enlarging the test strip at this point would only contribute additional redundancy to the steady-state solution.

Standardization of the simulations was necessary for a comparison across trials. To do this, a seeded random number generator was utilized to perturb the original inputs by altering their respective observation standard deviations (precision). A simple

structure was designed to simulate and standardize an image-matching algorithm based upon the desired number of tie points between the overlapping images. Recall that tie points are crucial for the proper implementation of the coplanarity condition as the observation model.

The focal point of this research is to determine how well this Kalman filtering and optimal smoothing algorithm can handle different parameters that affect the accuracy and precision of georeferencing parameters for simulated UAV imagery. Numerous trials were run altering the number of tie points and the initial GPS positional precision. The trials standardized the input standard deviation of the exterior orientation angles to 1° . Most inertial measurement units (IMU) found on a UAV are micro-electromechanical systems (MEMS) capable of obtaining an RMSE of less than 0.5° . Thus, the input precision is an overly pessimistic estimate. The following is a discussion of the initial findings from implementing this filtering and smoothing algorithm to sequential aerial triangulation.

The flying height was set to 200m for the simulations and sixteen conjugate tie point pairs were used to satisfy the coplanarity condition in each stereo pair. The positional precision was evaluated with horizontal precision twice as good as vertical precision. For example, the trial with a horizontal precision of 10m was given an initial vertical precision of 20m. Five separate trials were investigated with these input requirements. This was done to determine the effect input precision of the GPS position had on the output precision of the orientation angles. The following graph shows the convergence of the forward filter to a steady state solution for the precision of the exterior orientation angles; similar results are obtained for the remaining angles.

From Figure 8-2, the filter is increasing the precision of the orientation angles as the sequential orientation proceeds down the strip of photos. Although the precision of the GPS position has improved by a factor of 10 for four of the five trials, the improvement in the orientation precision does not improve by a factor of 10. These findings are typical across the various tie point trials. The implication is that improving GPS positional precision from consumer-grade ($\pm 10 \sigma$) to survey-grade ($\pm 0.1 \text{m } \sigma$ or $\pm 0.01 \text{m } \sigma$) results in substantial gains in orientation precision.

The same set of data (16 tie points with a 200m flying height) was input in the backward smoothing algorithm (Figure 8-3). The orientation precision results indicate that the smoother can further refine the forward filter output. This marked improvement in orientation precision from $\pm 1^\circ \sigma$ to $\pm 0.10^\circ \sigma$ offers encouraging results for the implementation of this algorithm.

In the simulation model, the actual or true values are known. Using data from previous trials, the authors analyzed the algorithm accuracy by comparing the true values with the filtered/smoothed results. The term "residual" will be used to define the difference between the true value and the estimated (filtered/smoothed) value, while the term "error" will be used to define the injected simulation error. The errors in the orientation angles are illustrated in Figure 8-4.

Theoretically, the residuals should be converging to 0° , with oscillations of $\pm 0.2^\circ$ based on algorithm design and the precision results. The gentle oscillations in the RTS smoothing curve over the 500 image sequence about 0° in this simulation offer strong support for this theory (Figure 8-4). The similarities between the weighted average and RTS smoothing are typical across the trials for all angles and tie point combinations.

The root-mean-square error (RMSE) across the different input position precisions is shown in Figure 8-5.

Recall that through the design of the simulation model the original unfiltered RMSE is 1° . The angular accuracy as measured by RMSE improves by approximately 75% from the consumer-grade GPS position precision of $\pm 10\text{m } \sigma$ to the mapping-grade GPS position precision of $\pm 1\text{m } \sigma$ (Figure 8-5). The improvement from mapping-grade to survey-grade precision (less than or equal to $\pm 0.1\text{m } \sigma$) is less substantial. These findings suggest that advanced geodetic-grade GPS receivers may not provide a substantial enough improvement in accuracy to create a positive return on investment. Furthermore, a less expensive mapping-grade GPS unit may be just as suitable for georeferencing parameter accuracy and precision as a top of the line geodetic-grade GPS unit when this algorithm is implemented.

The simulation model analysis makes it apparent that implementation of the sequential orientation algorithm can provide the user with substantial gains in both the precision and accuracy of the EOPs. Thus far, no thorough investigation of the optimal number of conjugate tie point pairs was made. Further simulation trials were run to analyze the impact of increasing/decreasing the number of tie points between the images. Fewer tie point pairs means increased computational efficiency. However, utilization of more tie points leads to improved strength of the geometric stereo model. Furthermore, using the Kalman filter already increases computational efficiency relative to a bundle adjustment. Thus, the expectation is that greater gains in angular orientation precision can be expected with an increase in the number of tie points used. The relationship between an average angular precision and the number of tie points using

an input positional precision of $\pm 0.1\text{m}$ horizontal and $\pm 0.2\text{m}$ vertical over the 500 image strip is illustrated in Figure 8-6. The flying height was maintained at 200m for the simulation.

The results in Figure 8-6 show an increase in the number of tie points has a direct linear relationship with an increase in precision of angular orientation (decrease in σ). Relative to the precision of the original orientation angle ($\pm 1^\circ$), any subsequent gains in precision after the initial trial with four tie points are only nominal improvements due to the computational efficiency of the algorithm. The relationship between accuracy (RMSE) and the number of tie points in each of the five trials is shown in Figure 8-7.

As shown in Figure 8-7, the 50% improvement in orientation accuracy gained by using nine tie points instead of four is considerable. However, all subsequent gains from using more tie points did not result in noteworthy accuracy improvement. These results were typical when comparing the previously used five input positional precisions over the different tie point number trials. When implementing this algorithm, the minimum optimal number of tie points per image pair is nine. Any increase in the number of tie points used will further strengthen the geometry of the stereo model but will lead to only nominal gains in angular precision and accuracy.

8.3.2 UAV Flight Data – Archer Field

Having shown significant gains in precision and accuracy for this sequential orientation algorithm in a controlled simulation environment, the algorithm's effectiveness was tested on actual UAV flight data. The data set used for the test was captured in 2002 using a video camera mounted on a University of Florida Geomatics Program designed UAV over Archer Field. Still aerial photography (Figure 8-8) derived from the video footage was evaluated by this algorithm. The Archer Field site was

chosen because of the numerous ground control points (GCPs) available to the researchers. The navigation data (angular orientation and position of the nodal point of the camera lens) captured during flight was deemed unreliable for use in evaluating accuracy. A simultaneous aerial triangulation bundle adjustment was performed to determine the EOP navigation baseline from which the accuracy of this algorithm implementation could be evaluated.

The flight strip consisted of 61 images with almost 80% overlap. Each image pair had about 25-30 tie point pairs. It is important to note that the tie point geometry is not nearly as strong as the simulation model tie point geometry. Thus, expectations were somewhat lower for this application. In order to show the effect of the forward Kalman filter and backward optimal smoother, the AT-derived EOPs were perturbed in position and attitude. Gaussian noise with a standard deviation of 5° was added to the AT-derived orientation angles. Bundle adjustment results suggest a horizontal and vertical positional precision of approximately $\pm 0.1\text{m}$ for the nodal point of the camera lens and an attitude precision of approximately $\pm 0.1^\circ$. Thus, the true position and attitude was already perturbed. Gaussian noise added via the input positional precision and input orientation precision further perturbed the exterior orientation parameters.

The filtered and smoothed precision results from the Archer UAV imagery exhibit significant gains in orientation precision. The approximately 60% improvement in orientation precision from the Archer imagery for an input position is shown in Figure 8-9. The orientation precision results illustrate that the smoother further refines the forward filter output. This marked improvement in orientation precision from $\pm 5^\circ \sigma$ to $\pm 1.5^\circ \sigma$ offers encouraging results for the continued implementation of this algorithm.

As mentioned previously, the authors performed a simultaneous bundle adjustment to serve as the EOP angular attitude baseline; the errors in the orientation angles are shown in Figure 8-4. Theoretically, the residuals should be converging to 0° with oscillations of $\pm 1.5^\circ$ based on algorithm design and the precision results. The oscillations in the RTS smoothing curve over the 61 image sequence (about 0° in this model) would offer even stronger support with a longer strip of imagery (Figure 8-10). Similar results were found for RTS smoothing across the trials for all angles and input position precisions. The root-mean-square error (RMSE) across the different input position precisions for the Archer UAV imagery is graphically illustrated in Figure 8-11.

Given the RMSE for the original input orientation parameters is $\pm 5^\circ$, the angular accuracy as measured by RMSE significantly improves (Figure 8-10). Approximately 50% gain can be realized from the original navigation positional precision to survey-grade positional precision ($\pm 0.1\text{m } \sigma$). These results suggest that with weaker tie point geometry, advanced geodetic-grade GPS receivers may provide a substantial enough improvement in accuracy to create a positive return on investment if GPS signal processing of mapping-grade receivers cannot produce decimeter level precision. A flight strip with more images may further improve the convergence of the oscillations around 0° for the angular orientation accuracy.

8.4 Summary & Conclusion

A method to process aerial imagery sequentially using an algorithm based on forward Kalman filtering and backward RTS optimal smoothing has been presented. The increases of approximately 90% in angular precision and approximately 80% in orientation accuracy achieved with this algorithm in simulation relative to the original input data are a testament to the gains that can be made utilizing this algorithm for

extrapolating quality georeferencing parameters from sequential aerial triangulation. Furthermore, initial findings using actual UAV flight data show significant improvements in attitude precision of 60% and attitude accuracy of 50%.

When utilizing this algorithm, it is suggested that imagery is acquired prior to reaching the target area. This premature imagery acquisition allows the system to initialize and reach steady state. Likewise, obtaining a few images beyond the target area is advised to avoid end-of-the-strip errors from affecting the beginning of the smoothing algorithm.

Further analysis of the strip model with different UAV data sets will be conducted. The analysis of this algorithm with block sequential aerial triangulation will be a focus for further research both in simulation and with UAV data sets. This block sequential AT is a natural progression because imagery acquisition is usually done in overlapping strips that form blocks of aerial photographs. Likewise, the application of this algorithm to a terrestrial platform is an area of much interest to the future development of GatorMMS VA implementation.

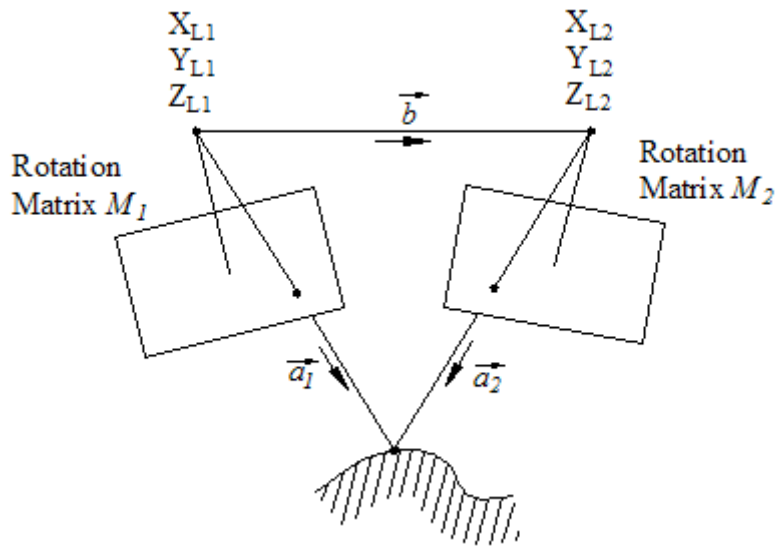


Figure 8-1. Geometry for the coplanarity condition (modified after Mikhail, E.M., J.S. Bethel, and J.C. McGlone. 2001. *Introduction to modern photogrammetry*. New York: Wiley. Available at: <http://www.loc.gov/catdir/toc/wiley021/2001281274.html>.)

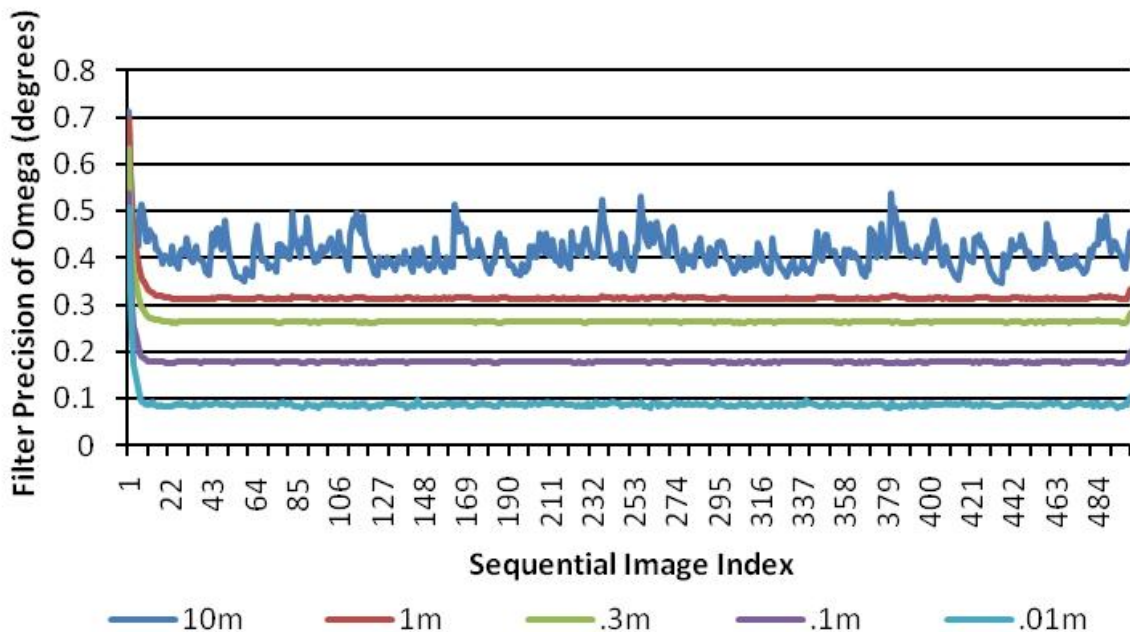


Figure 8-2. Improved orientation precision due to improved position precision with forward Kalman filtering

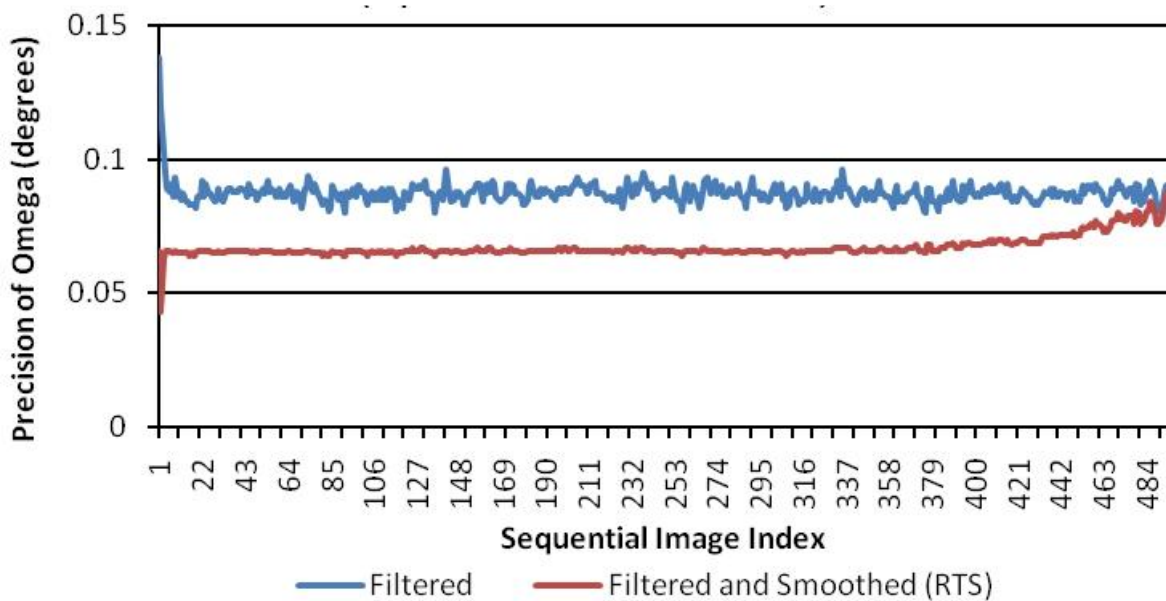
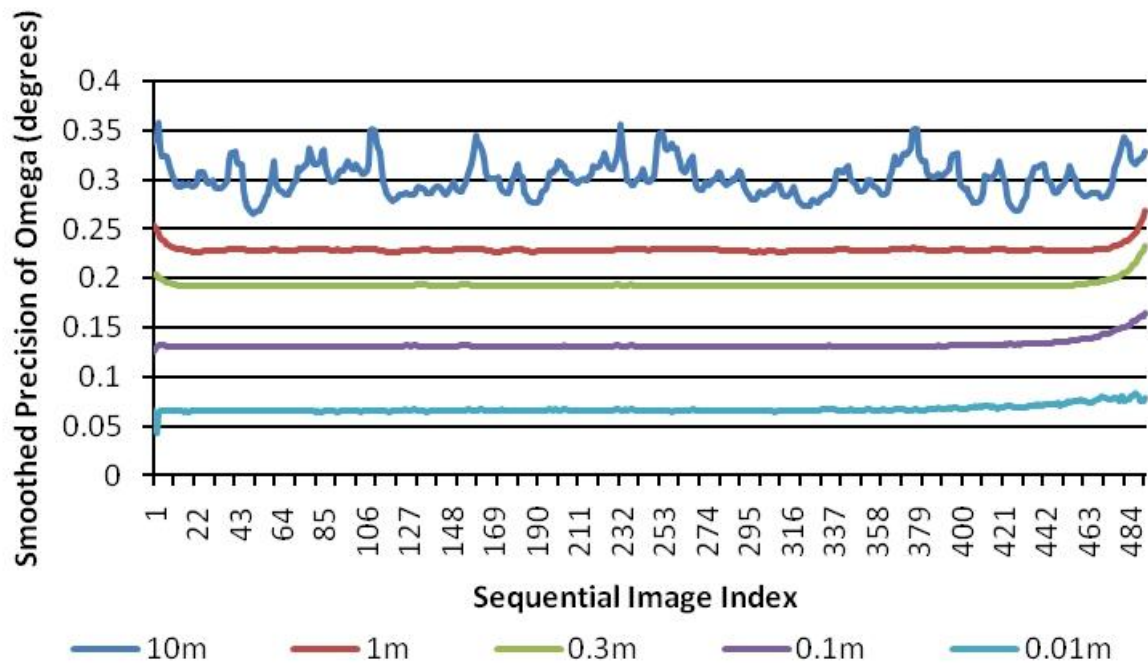


Figure 8-3. Improved orientation precision due to improved position precision with backward optimal smoothing. a: Detail of improved orientation precision due to forward Kalman filtering and backward optimal smoothing

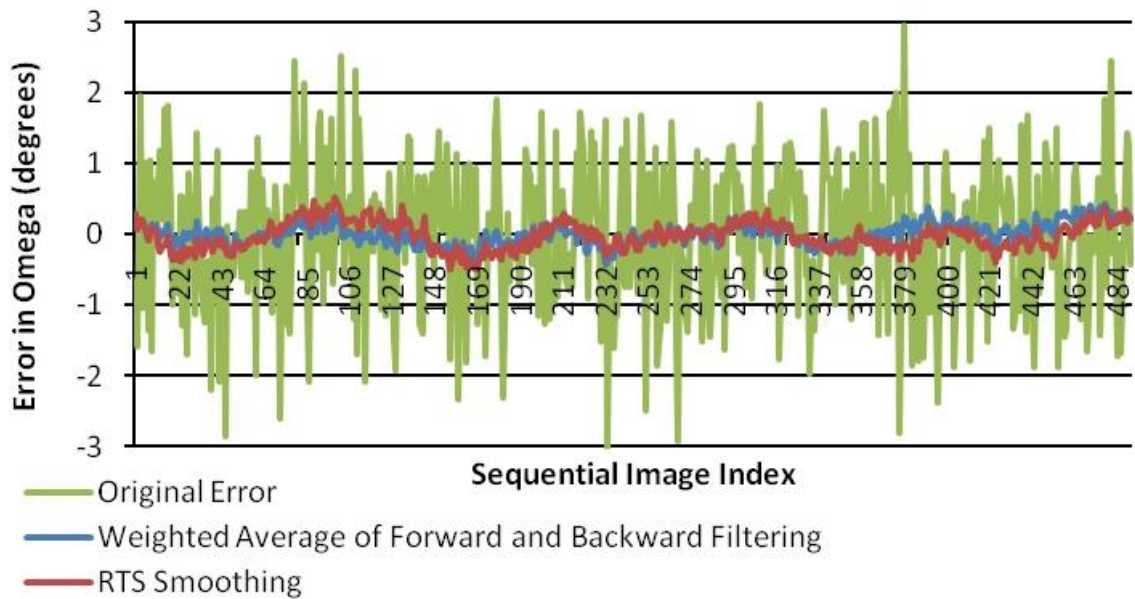


Figure 8-4. Orientation accuracy of backward optimal smoothing over entire image sequence.

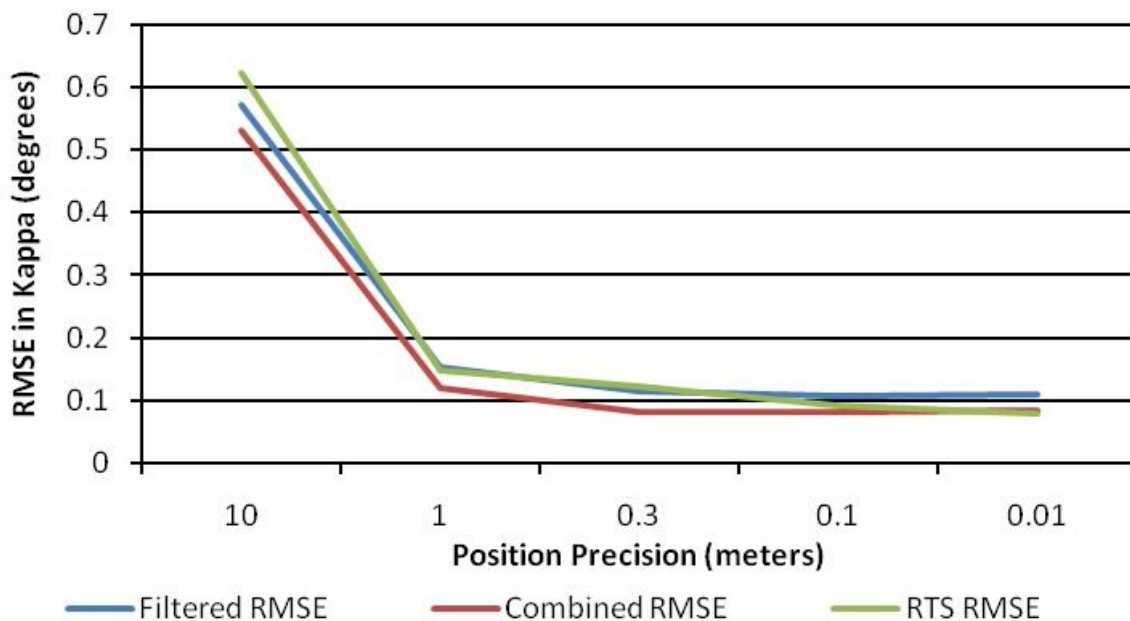


Figure 8-5. RMSE for different position precisions with forward Kalman filtering and backward optimal smoothing.

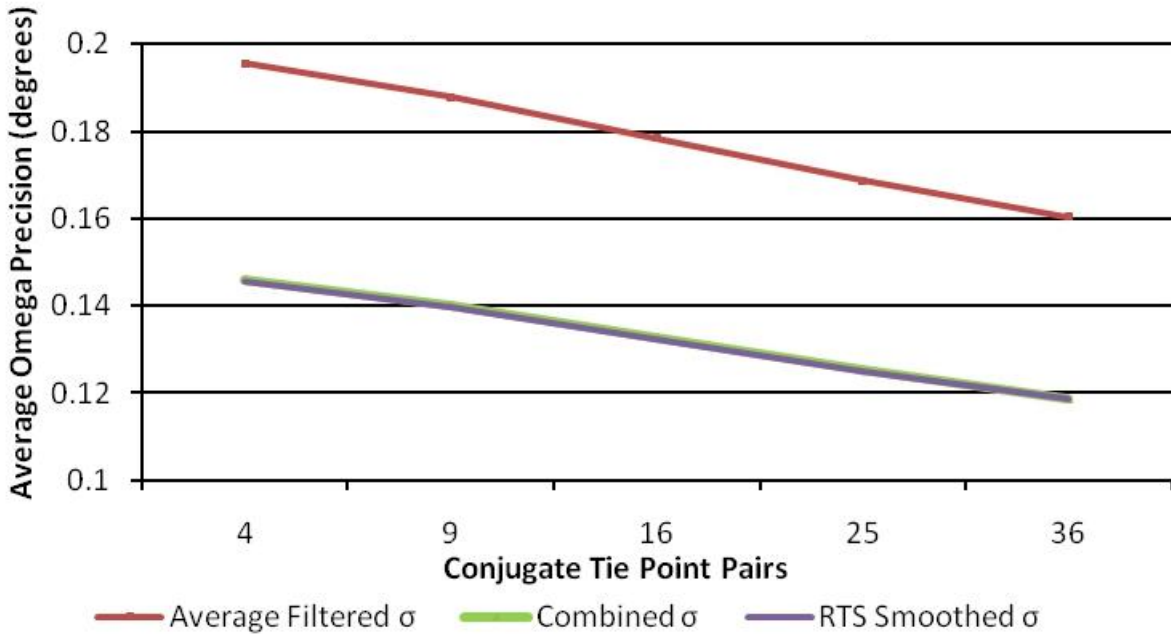


Figure 8-6. The effect of the number of tie points on average angular orientation precision with forward Kalman filtering and backward optimal smoothing.

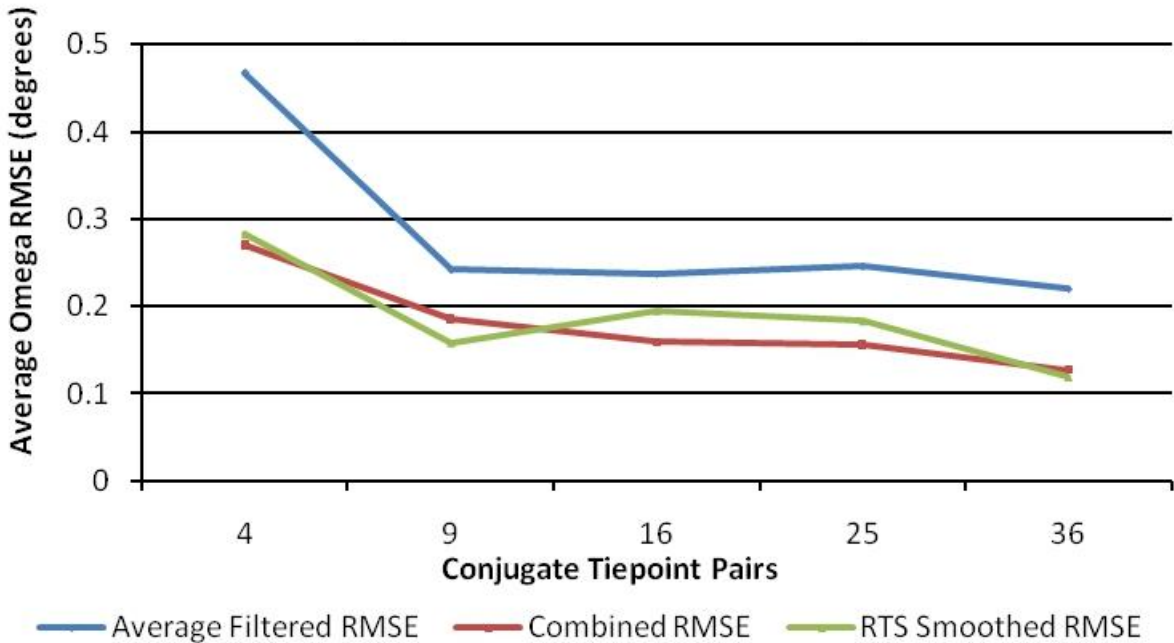


Figure 8-7. The effect of the number of tie points on average angular orientation accuracy with forward Kalman filtering and backward optimal smoothing.



Figure 8-8. UAV aerial image collected over Archer Field. The white circles in the image are the ground control points. (image courtesy of Benjamin Wilkinson)

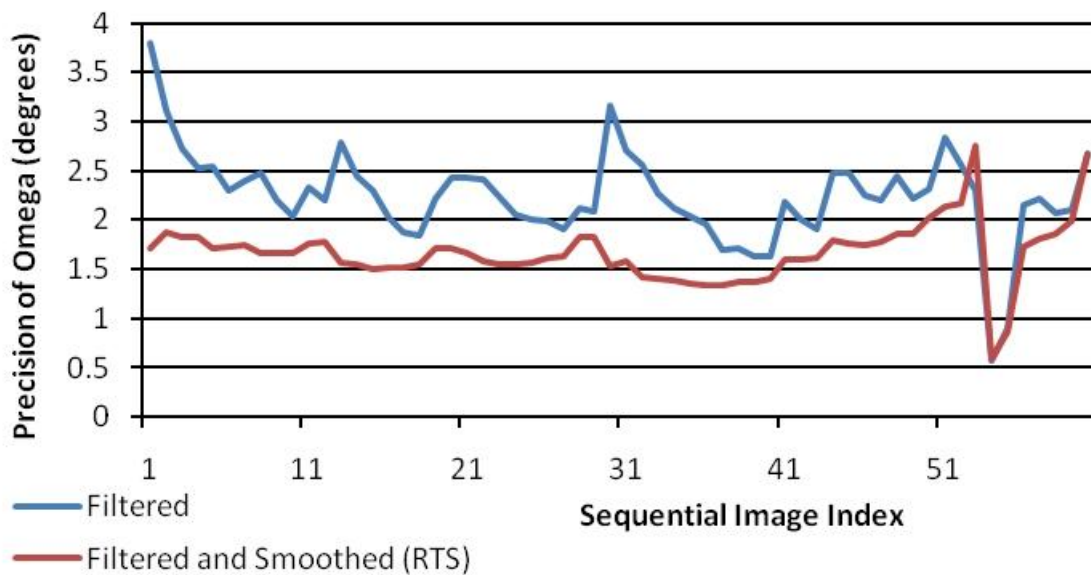


Figure 8-9. Detail of improved orientation precision due to forward Kalman filtering and backward optimal smoothing for Archer UAV data

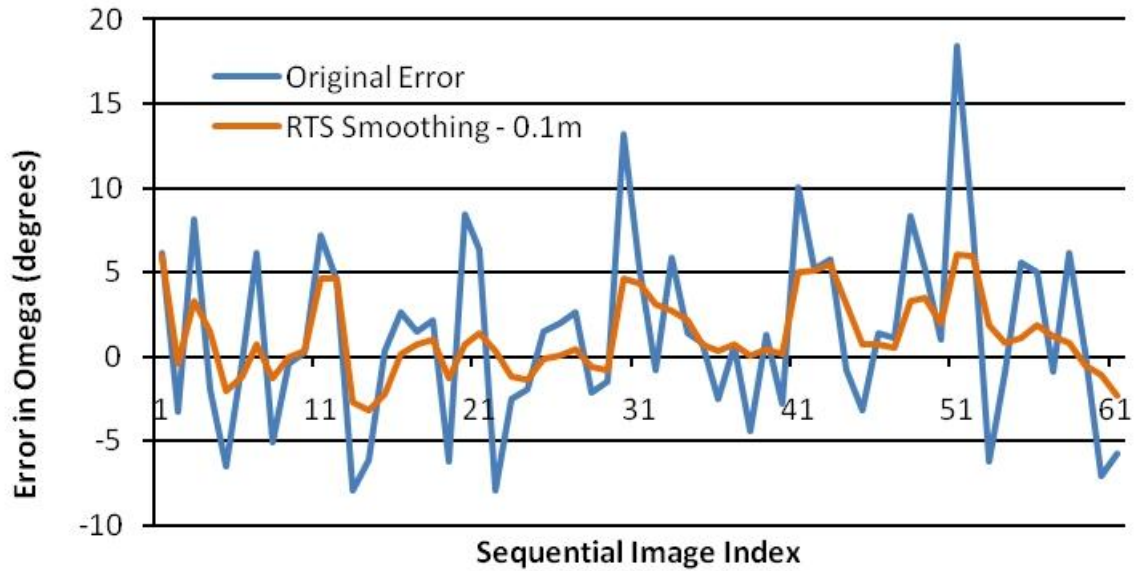


Figure 8-10. Orientation accuracy of backward optimal smoothing over entire image sequence through evaluation of RTS smoothing residuals for Archer UAV data

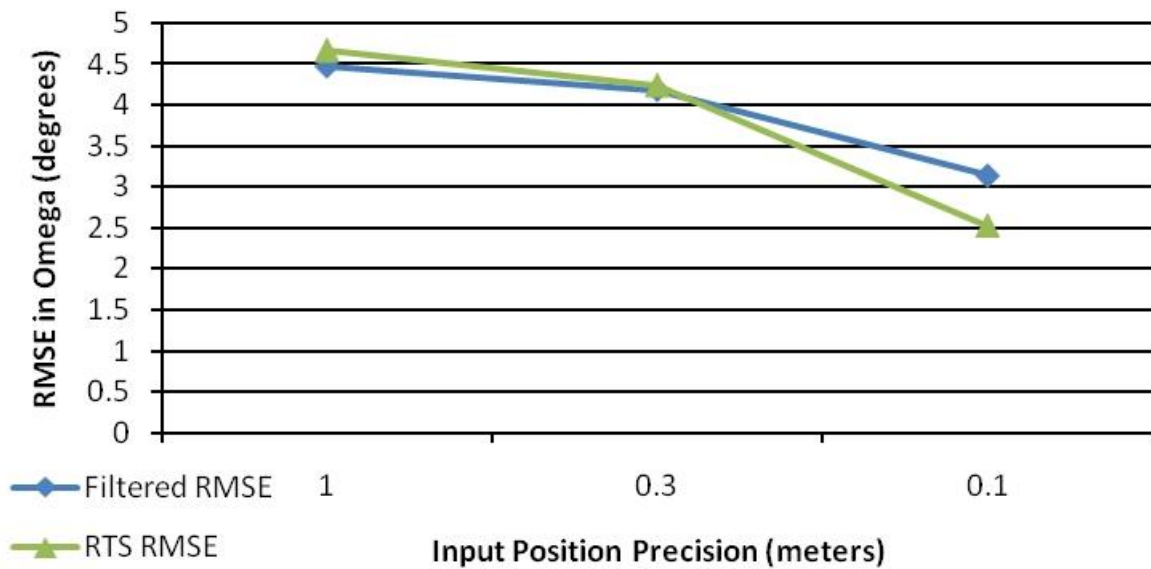


Figure 8-11. RMSE of angular orientation for different position precisions with forward Kalman filtering and backward optimal smoothing for Archer UAV data

CHAPTER 9 CONCLUSION

9.1 Summary & Conclusions

Extensive literature review of mobile mapping systems, vision-aiding, and forest mapping revealed many research studies on each separate topic. However, a lack of literature existed on the integration of these three topics in the use of vision-aiding by a terrestrial MMS for navigation and mapping in a forested environment. The thesis addressed this void through presentation of a method for developing and testing a terrestrial remote sensing mobile mapping system, the GatorMMS, beneath forest canopy.

A thorough discussion of GatorMMS components focused on the two primary GatorMMS subsystems, the georeferencing system and the imaging system, as separate entities. The time, position, and orientation of an event in space (i.e. moment of camera exposure) were determined by the GPS-aided inertial navigation georeferencing system. GPS/INS processing techniques and operational methods for improving the navigation solution beneath forest canopy were investigated in the georeferencing system testing. A digital single lens reflex camera was the principal component of the GatorMMS imaging subsystem. The stability of the DSLR camera interior orientation parameters were analyzed through the use of two separate calibration programs. After calibrating and testing each subsystem separately, the boresight lever arm (BSLA) calibration united these subsystems as one entity, the GatorMMS. The resultant BSLA calibration results were mm-level lever arm precision and milliradian-level boresight angle precision. These calibration precision results,

especially the stable orientation angles, made vision-aiding implementation feasible for the GatorMMS.

To determine where forest canopy conditions necessitated vision-aiding implementation, a GatorMMS canopy density (CDI) analysis operation was undertaken. A vertically oriented camera with a fish eye lens provided a wide angle view of the forest canopy along two test tracks. Even with a lack of canopy variability along the Austin Cary Memorial Forest (ACMF) test tracks, significant correlation existed between the canopy density and a few variables including number of satellites, PDOP, and horizontal/vertical precision for different GPS/INS integration techniques. Interestingly, the relationship between horizontal precision of the navigation solution and the time elapsed from static observation at these test tracks had the most significant correlation.

A high CDI test area along the ACMF test tracks was chosen for the GatorMMS vision-aiding (VA) application. The DLSR camera with a fixed focal length wide angle lens was operated in horizontal orientation for the VA application. Using photogrammetric adjustments to test VA in the forest, all exterior orientation parameter (EOP) precisions were significantly improved through VA implementation. The EOP precision that gained the most from VA, heading, significantly improved by one order of magnitude. Heading is the least precise EOP; thus, improvement of this magnitude is emphasized as a major breakthrough. Improvements in angular precision are essential because angular error propagates over the distance the object is from the sensor.

The thesis research concluded with the development of an orientation algorithm to sequentially handle image, position, and orientation updates. The sequential algorithm development was a product of making the vision-aiding method a near real-time

approach as opposed to the batch post processing methods used in the ACMF VA test area. The direct georeferencing results from the sequential algorithm showed quantitative improvements in angular precision and angular accuracy relative to vision-aiding free navigation.

9.2 Recommendations

The most pressing need for future study is the application of the sequential orientation algorithm to a terrestrial platform. The direct georeferencing algorithm was not tested with loss of GPS position. Thus, implementation in an open area with GPS updates is important before implementing under forest canopy with significant satellite obstructions.

Future research and application of computer vision pass point generation algorithms for feature extraction in forested areas is necessary. This would eliminate the manually intensive methods developed in Chapter 7 covering the ACMF VA implementation.

Fisheye lenses were only used in the canopy density application. Using these lenses for horizontal MMS deployment would lead to an increased field-of-view and greater stereo model overlap between consecutive images. Two main obstacles exist with the use of fisheye lenses for this purpose. Before field implementation, the interior orientation parameters must be accurately calibrated to model the geometry and distortions of the different lens structure. Previous attempts of modeling fisheye projection geometry with conventional pinhole camera calibration software were unsuccessful. Thus, new calibration software must be developed that incorporates the lens geometry outlined in Figure 3-7. In addition, the increased field of view means objects will appear smaller and be imaged in fewer pixels relative to conventional

cameras. Thus, algorithms must be efficient at matching smaller tie points between consecutive images.

After improving the navigation trajectory in GPS outage prone areas, feature mapping from VA stereo models is a natural research progression for forest managers that should be explored. The extracted features would contain the geospatial information forest managers need for input into a forest GIS to make responsible management decisions.

APPENDIX A
OTSU'S IMAGE THRESHOLDING METHOD

The details and derivation of Otsu's image thresholding algorithm provided in Appendix A are from Zheng et al. (2005) and Otsu (1979). Please consult these sources for further background information and additional derivation information.

The following is an application of Otsu's thresholding method to sky versus canopy classification.

$$q_c(T) = \sum_{i=1}^T P(i) \text{ and } q_s(T) = \sum_{i=T+1}^L P(i) \quad (\text{A-1})$$

where i is the gray level, L is the number of gray levels, $P(i)$ is the normalized frequency of i , T is the threshold, $q_c(T)$ is the normalized fraction of pixels classified as canopy, and $q_s(T)$ is the normalized fraction of pixels classified as sky.

The mean grayscale values for the canopy pixels, $\mu_c(T)$, and the sky pixels, $\mu_s(T)$, are:

$$\mu_c(T) = \frac{\sum_{i=1}^T iP(i)}{\sum_{i=1}^T P(i)} = \frac{1}{q_c(T)} \sum_{i=1}^T iP(i) \quad (\text{A-2})$$

$$\mu_s(T) = \frac{\sum_{i=T+1}^L iP(i)}{\sum_{i=T+1}^L P(i)} = \frac{1}{q_s(T)} \sum_{i=T+1}^L iP(i) \quad (\text{A-3})$$

The variance for the canopy pixels, $\sigma_c^2(T)$, is:

$$\sigma_c^2(T) = \frac{\sum_{i=1}^T (i - \mu_c)^2 P(i)}{\sum_{i=1}^T P(i)} = \frac{1}{q_c(T)} \sum_{i=1}^T (i - \mu_c)^2 P(i) \quad (\text{A-4})$$

Likewise, the variance for the sky pixels, $\sigma_s^2(T)$, is:

$$\sigma_s^2(T) = \frac{\sum_{i=T+1}^L (i - \mu_s)^2 P(i)}{\sum_{i=T+1}^L P(i)} = \frac{1}{q_s(T)} \sum_{i=T+1}^L (i - \mu_s)^2 P(i) \quad (\text{A-5})$$

The intra-group variance, $\sigma_{IG}^2(T)$, is:

$$\sigma_{IG}^2(T) = q_c(T)\sigma_c^2(T) + q_s(T)\sigma_s^2(T) \quad (\text{A-6})$$

By testing each grayscale value from 0 at the beginning of the histogram to L at the end of the histogram, the threshold T will be the value that minimizes $\sigma_{IG}^2(T)$.

APPENDIX B KALMAN FILTER DETAILS

The Kalman filter is a set of mathematical equations that implement a predictor-corrector type estimator that is considered optimal because it minimizes the estimated error covariance. Per Gelb (1974), an optimal estimator is a “computational algorithm that processes measurements to deduce a minimum error estimate of the state of a system by utilizing: knowledge of system and measurement dynamics, assumed statistics noises and measurement errors, and initial condition information.” Using a Kalman filter is the most common technique for estimating the state of a linear system.

Modified after Gelb (1974), Figure B-1 is a block diagram depicting the linear flow of the Kalman filter operation. The Kalman filter predicts variables of the next state from the previous state’s variables and current measurements.

The Kalman filter equations as follows are derived and found in numerous texts including Kalman (1960), Gelb (1974), and Welch and Bishop (2001). Expressing this linear discrete-time controlled process diagram in equation form,

$$x_k = Ax_{k-1} + Bu_k + w_{k-1} \quad (\text{B-1})$$

with the measurement equation expressed

$$z_k = Hx_k + v_k \quad (\text{B-2})$$

where w_k is the process noise (system error), v_k is the measurement noise (measurement error), u_k is the optional control input, A is the matrix that relates the state at the previous time step to the current time step, B is the matrix that relates the optional control input to the system state, and H is the matrix that relates the state to the observation.

The system error and the measurement error are assumed to be independent of each other, white, and with normal probability distributions. Put another way, the noise signal can be thought of as being completely uncorrelated from itself except at a precise epoch at which point the signal is completely correlated with itself. This leads individuals to refer to these signals as independent since any sample of the signal at one time is independent (uncorrelated) from a signal sample at any other time.

Again, the objective of the Kalman filter is to obtain the system state estimate \hat{x}_k (*a posteriori* state estimate) as a linear combination of a predicted estimate \hat{x}_k^- (*a priori* estimate) and a weighted difference between an observation z_k and a measurement prediction $H\hat{x}_k^-$. In equation form,

$$\hat{x}_k = \hat{x}_k^- + K(z_k - H\hat{x}_k^-) \quad (\text{B-3})$$

where K is the Kalman gain that minimizes the *a posteriori* error covariance and $(z_k - H\hat{x}_k^-)$ is the measurement innovation or residual.

The residual is a reflection of the difference between the predicted measurement and the observation (actual measurement). A popular form of the Kalman gain matrix equation as derived in (Welch and Bishop 2001) is shown below.

$$K_k = P_k^- H^T (H P_k^- H^T + R)^{-1} \quad (\text{B-4})$$

where P_k^- is the *a priori* error covariance, H^T is the transpose of the matrix which relates the state to the observation, and R is the measurement noise covariance matrix

The final measurement update equation used in the discrete Kalman filter algorithm is the *a posteriori* estimate error covariance equation. This update is used to

formulate the *a priori* estimate error covariance for the next epoch, $(k + 1)$. The covariance measurement equation update is shown below.

$$P_k = (I - K_k H) P_k^- \quad (\text{B-5})$$

where P_k is the *a posteriori* error covariance matrix and I is the identity matrix.

The discrete Kalman filter algorithm is a recursive filter as it constantly predicts and subsequently corrects the predictions. Thus, time update equations must be considered in addition to the previously discussed measurement update equations. The following equation forms the *a priori* state estimate \hat{x}_k^- by substituting the initial estimate \hat{x}_{k-1} , the *a posteriori* state estimate from the previous epoch, into the original linear discrete-time controlled process Kalman filter equation mentioned earlier.

$$\hat{x}_k^- = A \hat{x}_{k-1} + B u_k \quad (\text{B-6})$$

Likewise, it is necessary that the error covariance is projected ahead from the previous epoch. The *a priori* covariance estimate P_k^- is computed by incorporating the initial estimate P_{k-1} , the *a posteriori* covariance estimate from the previous epoch, with the process noise covariance matrix Q .

$$P_k^- = A P_{k-1} A^T + Q \quad (\text{B-7})$$

The three measurement update equations serve as corrections to the two time update equations in a cyclical manner as more measurements are added to the algorithm. As a result, the Kalman filter is being conditioned by all of the previous measurements. By sequentially handling the observation data as it comes in and incorporating this data into the filtering process, the storage requirements are much less

demanding than a batch processing algorithm. To implement the discrete Kalman filter algorithm, an observation model must be developed.

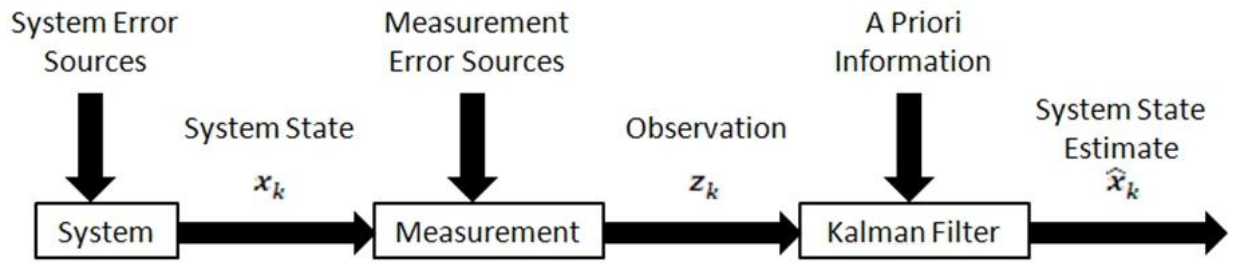


Figure B-1. Kalman filter operation block diagram (modified after Gelb, A. 1974. *Applied Optimal Estimation*. Cambridge, MA: MIT Press.)

APPENDIX C
COPLANARITY CONDITION DETAILS

C.1 Non-linear Coplanarity Condition

The basic coplanarity equations have been adopted from Mikhail et al. (2001).

Where gaps in the derivation existed, further explanation and equation derivation has been provided to offer a more comprehensive overview of the coplanarity condition. As

illustrated in Figure 8-1, the base vector between the two exposure stations is \vec{b} .

Vectors, \vec{a}_1 and \vec{a}_2 , are the object space rays from the exposure stations through their respective conjugate image points to the common object space point. The components of these three vectors are shown in Equation C-1, C-2, and C-3.

$$\vec{b} = \begin{bmatrix} b_x \\ b_y \\ b_z \end{bmatrix} = \begin{bmatrix} X_{L_2} - X_{L_1} \\ Y_{L_2} - Y_{L_1} \\ Z_{L_2} - Z_{L_1} \end{bmatrix} \quad (\text{C-1})$$

$$\vec{a}_1 = \begin{bmatrix} u_1 \\ v_1 \\ w_1 \end{bmatrix} = M_1^T \begin{bmatrix} x - x_0 \\ y - y_0 \\ -f \end{bmatrix}_1 \quad (\text{C-2})$$

$$\vec{a}_2 = \begin{bmatrix} u_2 \\ v_2 \\ w_2 \end{bmatrix} = M_2^T \begin{bmatrix} x - x_0 \\ y - y_0 \\ -f \end{bmatrix}_2 \quad (\text{C-3})$$

where x_0, y_0 are principal point coordinates, x, y are the image coordinates, and f is the focal length of the camera.

$$M_i^T = \begin{bmatrix} m_{11} & m_{21} & m_{31} \\ m_{12} & m_{22} & m_{32} \\ m_{13} & m_{23} & m_{33} \end{bmatrix}_i = \begin{bmatrix} \cos \phi \cos \kappa & -\cos \phi \sin \kappa & \sin \phi \\ \sin \omega \sin \phi \cos \kappa + \cos \omega \sin \kappa & -\sin \omega \sin \phi \sin \kappa + \cos \omega \cos \kappa & -\sin \omega \cos \phi \\ -\cos \omega \sin \phi \cos \kappa + \sin \omega \sin \kappa & \cos \omega \sin \phi \sin \kappa + \sin \omega \cos \kappa & \cos \omega \cos \phi \end{bmatrix}_i \quad (\text{C-4})$$

Through matrix multiplication, expansion of the object space ray components follows:

$$\begin{bmatrix} u \\ v \\ w \end{bmatrix} = \begin{bmatrix} \cos \phi \cos \kappa (x - x_0) - \cos \phi \sin \kappa (y - y_0) - \sin \phi (f) \\ (\sin \omega \sin \phi \cos \kappa + \cos \omega \sin \kappa) (x - x_0) + (-\sin \omega \sin \phi \sin \kappa + \cos \omega \cos \kappa) (y - y_0) + \sin \omega \cos \phi (f) \\ (-\cos \omega \sin \phi \cos \kappa + \sin \omega \sin \kappa) (x - x_0) + (\cos \omega \sin \phi \sin \kappa + \sin \omega \cos \kappa) (y - y_0) - \cos \omega \cos \phi (f) \end{bmatrix} \quad (\text{C-5})$$

Expressing these components in determinant form,

$$F = |\vec{b} \cdot (\vec{a}_1 \times \vec{a}_2)| = \begin{vmatrix} b_x & b_y & b_z \\ u_1 & v_1 & w_1 \\ u_2 & v_2 & w_2 \end{vmatrix} = 0 \quad (\text{C-6})$$

To further develop the observation model, the coplanarity condition can also take the form

$$Z_e = [x_1 \quad y_1 \quad z_1] F \begin{bmatrix} x_2 \\ y_2 \\ z_2 \end{bmatrix} = 0 \quad (\text{C-7})$$

where Z_e is the equivalent observation and F is the fundamental matrix that contains the exterior orientation parameters (EOPs) and the interior orientation parameters (IOPs) of both images in the stereo model.

$$F = C_1^T M_1 K_b M_2^T C_2 \quad (\text{C-8})$$

where C is the calibration matrix that contains the interior orientation parameters as shown in Equation C-9, K_b is the skew-symmetric matrix that contains the base vector information between the two exposure stations, and M_1 is the rotation matrix of image 1 in the stereopair.

$$C = \begin{bmatrix} 1 & 0 & -x_0 \\ 0 & 1 & -y_0 \\ 0 & 0 & -f \end{bmatrix} \quad (\text{C-9})$$

$$K_b = \begin{bmatrix} 0 & -b_z & b_y \\ b_z & 0 & -b_x \\ -b_y & b_x & 0 \end{bmatrix} = \begin{bmatrix} 0 & -(Z_{L_2} - Z_{L_1}) & Y_{L_2} - Y_{L_1} \\ Z_{L_2} - Z_{L_1} & 0 & -(X_{L_2} - X_{L_1}) \\ -(Y_{L_2} - Y_{L_1}) & X_{L_2} - X_{L_1} & 0 \end{bmatrix} \quad (C-10)$$

Further derivation of the skew-symmetric coplanarity model can be found in (Mikhail et al. 2001). The skew-symmetric matrix form of the coplanarity constraint is implemented in (Webb 2007) as the observation model for an extended Kalman filter. Webb uses the observation model for vision-based state estimation. The focus of the dissertation lies more in the use of the coplanarity condition for UAV navigation than for georeferencing aerial imagery.

For implementation of the algorithm developed here, the premise is to obtain an optimal solution for the georeferencing exterior orientation parameters that satisfies the coplanarity equation for a number of tie points between two images. The coplanarity condition is nonlinear as expressed above in either determinant form or skew-symmetric form.

C.2 Linearization of the Coplanarity Condition

This algorithm implements the linearized form of the coplanarity equations for use with Kalman filtering. To linearize the determinant form of the coplanarity equation, partial derivatives of the determinant with respect to exterior orientation parameters and image point measurements are necessary. Recall that the derivative of a determinant of order 3 with respect to a parameter p is equal to the sum of 3 determinants. If R_1 , R_2 , and R_3 are the three rows of a determinant D , then

$$\frac{\partial D}{\partial p} = \begin{vmatrix} \partial R_1 / \partial p \\ R_2 \\ R_3 \end{vmatrix} + \begin{vmatrix} R_1 \\ \partial R_2 / \partial p \\ R_3 \end{vmatrix} + \begin{vmatrix} R_1 \\ R_2 \\ \partial R_3 / \partial p \end{vmatrix} \quad (C-11)$$

The linearized form of the coplanarity equation is written in Equation C-12 as an expression for one pair of conjugate image points, tie points.

$$\begin{array}{ccccccc}
 B & v & + & H & x & - & f = 0 \\
 1 \times 4 & 4 \times 1 & & 1 \times 12 & 12 \times 1 & & 1 \times 1
 \end{array} \tag{C-12}$$

where v is the vector of four observational residuals and x are the corrections to the exterior orientation parameters.

$$B = [\partial F/\partial x_1 \quad \partial F/\partial y_1 \quad \partial F/\partial x_2 \quad \partial F/\partial y_2] \tag{C-13}$$

$$H = \left[\frac{\partial F}{\partial \omega_1} \quad \frac{\partial F}{\partial \phi_1} \quad \frac{\partial F}{\partial \kappa_1} \quad \frac{\partial F}{\partial X_{L1}} \quad \frac{\partial F}{\partial Y_{L1}} \quad \frac{\partial F}{\partial Z_{L1}} \quad \frac{\partial F}{\partial \omega_2} \quad \frac{\partial F}{\partial \phi_2} \quad \frac{\partial F}{\partial \kappa_2} \quad \frac{\partial F}{\partial X_{L2}} \quad \frac{\partial F}{\partial Y_{L2}} \quad \frac{\partial F}{\partial Z_{L2}} \right] \tag{C-14}$$

$$f = -F^0 = - \begin{vmatrix} b_x & b_y & b_z \\ u_1 & v_1 & w_1 \\ u_2 & v_2 & w_2 \end{vmatrix} \tag{C-15}$$

The matrices, H and B , are known as Jacobian matrices. In vector calculus, a Jacobian matrix is the matrix containing the coefficients of the linearized observation equations (Ghilani and Wolf 2006). B is the Jacobian matrix of the coplanarity equation with respect to the image point observations. H is the Jacobian matrix of the coplanarity equation with respect to the exterior orientation parameters. The Jacobian represents the best linear approximation to a differentiable function at a given point. Thus, the Jacobian matrix consisting of all the tie points can be thought of as the effect geometry has on the determination of the exterior orientation parameters.

Due to each image coordinate appearing in only one row, each of the elements of B comprises only one determinant. The partial derivatives with respect to the four image point observations are shown in Equations C-16 through C-19.

$$b_{11} = \frac{\partial F}{\partial x_1} = 0 + \begin{vmatrix} b_x & b_y & b_z \\ \frac{\partial u_1}{\partial x_1} & \frac{\partial v_1}{\partial x_1} & \frac{\partial w_1}{\partial x_1} \\ u_2 & v_2 & w_2 \end{vmatrix} + 0 = \begin{vmatrix} b_x & b_y & b_z \\ (m_{11})_1 & (m_{12})_1 & (m_{13})_1 \\ u_2 & v_2 & w_2 \end{vmatrix}^0 \quad (\text{C-16})$$

$$\text{where } \frac{\partial}{\partial x_1} \begin{bmatrix} u_1 \\ v_1 \\ w_1 \end{bmatrix} = M_1^T \begin{bmatrix} 1 \\ 0 \\ 0 \end{bmatrix} = \begin{bmatrix} m_{11} \\ m_{12} \\ m_{13} \end{bmatrix}_1$$

$$b_{12} = \frac{\partial F}{\partial y_1} = 0 + \begin{vmatrix} b_x & b_y & b_z \\ \frac{\partial u_1}{\partial y_1} & \frac{\partial v_1}{\partial y_1} & \frac{\partial w_1}{\partial y_1} \\ u_2 & v_2 & w_2 \end{vmatrix} + 0 = \begin{vmatrix} b_x & b_y & b_z \\ (m_{21})_1 & (m_{22})_1 & (m_{23})_1 \\ u_2 & v_2 & w_2 \end{vmatrix}^0 \quad (\text{C-17})$$

$$\text{where } \frac{\partial}{\partial y_1} \begin{bmatrix} u_1 \\ v_1 \\ w_1 \end{bmatrix} = M_1^T \begin{bmatrix} 0 \\ 1 \\ 0 \end{bmatrix} = \begin{bmatrix} m_{21} \\ m_{22} \\ m_{23} \end{bmatrix}_1$$

$$b_{13} = \frac{\partial F}{\partial x_2} = 0 + 0 + \begin{vmatrix} b_x & b_y & b_z \\ u_1 & v_1 & w_1 \\ \frac{\partial u_2}{\partial x_2} & \frac{\partial v_2}{\partial x_2} & \frac{\partial w_2}{\partial x_2} \end{vmatrix} = \begin{vmatrix} b_x & b_y & b_z \\ u_1 & v_1 & w_1 \\ (m_{11})_2 & (m_{12})_2 & (m_{13})_2 \end{vmatrix}^0 \quad (\text{C-18})$$

$$\text{where } \frac{\partial}{\partial x_2} \begin{bmatrix} u_2 \\ v_2 \\ w_2 \end{bmatrix} = M_2^T \begin{bmatrix} 1 \\ 0 \\ 0 \end{bmatrix} = \begin{bmatrix} m_{11} \\ m_{12} \\ m_{13} \end{bmatrix}_2$$

$$b_{14} = \frac{\partial F}{\partial y_2} = 0 + 0 + \begin{vmatrix} b_x & b_y & b_z \\ u_1 & v_1 & w_1 \\ \frac{\partial u_2}{\partial y_2} & \frac{\partial v_2}{\partial y_2} & \frac{\partial w_2}{\partial y_2} \end{vmatrix} = \begin{vmatrix} b_x & b_y & b_z \\ u_1 & v_1 & w_1 \\ (m_{21})_2 & (m_{22})_2 & (m_{23})_2 \end{vmatrix}^0 \quad (\text{C-19})$$

$$\text{where } \frac{\partial}{\partial y_2} \begin{bmatrix} u_2 \\ v_2 \\ w_2 \end{bmatrix} = M_2^T \begin{bmatrix} 0 \\ 1 \\ 0 \end{bmatrix} = \begin{bmatrix} m_{21} \\ m_{22} \\ m_{23} \end{bmatrix}_2$$

The partial derivatives of the coplanarity equation with respect to the exterior orientation parameters for the first image can be found below. The partial derivatives for

the second image are derived in a similar manner and are not shown to avoid redundancy.

Recall the Jacobian of H is:

$$H = \begin{bmatrix} \frac{\partial F}{\partial \omega_1} & \frac{\partial F}{\partial \phi_1} & \frac{\partial F}{\partial \kappa_1} & \frac{\partial F}{\partial X_{L_1}} & \frac{\partial F}{\partial Y_{L_1}} & \frac{\partial F}{\partial Z_{L_1}} & \frac{\partial F}{\partial \omega_2} & \frac{\partial F}{\partial \phi_2} & \frac{\partial F}{\partial \kappa_2} & \frac{\partial F}{\partial X_{L_2}} & \frac{\partial F}{\partial Y_{L_2}} & \frac{\partial F}{\partial Z_{L_2}} \end{bmatrix} \quad (\text{C-20})$$

To simplify, let x equal $(x - x_0)$ and y equal $(y - y_0)$.

$$h_{11} = \frac{\partial F}{\partial \omega_1} = 0 + \begin{bmatrix} b_x & b_y & b_z \\ \frac{\partial u_1}{\partial \omega_1} & \frac{\partial v_1}{\partial \omega_1} & \frac{\partial w_1}{\partial \omega_1} \\ u_2 & v_2 & w_2 \end{bmatrix} + 0 = \begin{bmatrix} b_x & b_y & b_z \\ 0 & -w_1 & v_1 \\ u_2 & v_2 & w_2 \end{bmatrix} \quad (\text{C-21})$$

where

$$\begin{aligned} \frac{\partial}{\partial \omega_1} \begin{bmatrix} u_1 \\ v_1 \\ w_1 \end{bmatrix} &= \frac{\partial}{\partial \omega_1} \begin{bmatrix} \cos \phi \cos \kappa(x) - \cos \phi \sin \kappa(y) - \sin \phi(f) \\ (\sin \omega \sin \phi \cos \kappa + \cos \omega \sin \kappa)(x) + (-\sin \omega \sin \phi \sin \kappa + \cos \omega \cos \kappa)(y) + \sin \omega \cos \phi(f) \\ (-\cos \omega \sin \phi \cos \kappa + \sin \omega \sin \kappa)(x) + (\cos \omega \sin \phi \sin \kappa + \sin \omega \cos \kappa)(y) - \cos \omega \cos \phi(f) \end{bmatrix} \\ &= \begin{bmatrix} 0 \\ (\cos \omega \sin \phi \cos \kappa - \sin \omega \sin \kappa)x + (-\cos \omega \sin \phi \sin \kappa - \sin \omega \cos \kappa)y + \cos \omega \cos \phi(f) \\ (\sin \omega \sin \phi \cos \kappa + \cos \omega \sin \kappa)x + (-\sin \omega \sin \phi \sin \kappa + \cos \omega \cos \kappa)y + \sin \omega \cos \phi(f) \end{bmatrix} = \begin{bmatrix} 0 \\ -w_1 \\ v_1 \end{bmatrix} \end{aligned} \quad (\text{C-22})$$

$$h_{12} = \frac{\partial F}{\partial \phi_1} = 0 + \begin{bmatrix} b_x & b_y & b_z \\ \frac{\partial u_1}{\partial \phi_1} & \frac{\partial v_1}{\partial \phi_1} & \frac{\partial w_1}{\partial \phi_1} \\ u_2 & v_2 & w_2 \end{bmatrix} + 0 = \begin{bmatrix} b_x & b_y & b_z \\ c_1 & d_1 & e_1 \\ u_2 & v_2 & w_2 \end{bmatrix} \quad (\text{C-23})$$

where

$$\begin{aligned} \frac{\partial}{\partial \phi_1} \begin{bmatrix} u_1 \\ v_1 \\ w_1 \end{bmatrix} &= \frac{\partial}{\partial \phi_1} \begin{bmatrix} \cos \phi \cos \kappa(x) - \cos \phi \sin \kappa(y) - \sin \phi(f) \\ (\sin \omega \sin \phi \cos \kappa + \cos \omega \sin \kappa)(x) + (-\sin \omega \sin \phi \sin \kappa + \cos \omega \cos \kappa)(y) + \sin \omega \cos \phi \\ (-\cos \omega \sin \phi \cos \kappa + \sin \omega \sin \kappa)(x) + (\cos \omega \sin \phi \sin \kappa + \sin \omega \cos \kappa)(y) - \cos \omega \cos \phi \end{bmatrix} \\ &= \begin{bmatrix} -\sin \phi \cos \kappa(x) + \sin \phi \sin \kappa(y) - \cos \phi(f) \\ (\sin \omega \cos \phi \cos \kappa)(x) + (-\sin \omega \cos \phi \sin \kappa)(y) - \sin \omega \sin \phi(f) \\ (-\cos \omega \cos \phi \cos \kappa)(x) + (\cos \omega \cos \phi \sin \kappa)(y) + \cos \omega \sin \phi(f) \end{bmatrix} = \begin{bmatrix} c_1 \\ d_1 \\ e_1 \end{bmatrix} \end{aligned} \quad (\text{C-24})$$

$$h_{13} = \frac{\partial F}{\partial \kappa_1} = 0 + \left| \begin{array}{ccc} b_x & b_y & b_z \\ \frac{\partial u_1}{\partial \kappa_1} & \frac{\partial v_1}{\partial \kappa_1} & \frac{\partial w_1}{\partial \kappa_1} \\ u_2 & v_2 & w_2 \end{array} \right| + 0 = \left| \begin{array}{ccc} b_x & b_y & b_z \\ o_1 & p_1 & q_1 \\ u_2 & v_2 & w_2 \end{array} \right|_0 \quad (\text{C-25})$$

where

$$\begin{aligned} \frac{\partial}{\partial \kappa_1} \begin{bmatrix} u_1 \\ v_1 \\ w_1 \end{bmatrix} &= \frac{\partial}{\partial \kappa_1} \begin{bmatrix} \cos \phi \cos \kappa(x) - \cos \phi \sin \kappa(y) - \sin \phi(f) \\ (\sin \omega \sin \phi \cos \kappa + \cos \omega \sin \kappa)(x) + (-\sin \omega \sin \phi \sin \kappa + \cos \omega \cos \kappa)(y) + \sin \omega \cos \phi(f) \\ (-\cos \omega \sin \phi \cos \kappa + \sin \omega \sin \kappa)(x) + (\cos \omega \sin \phi \sin \kappa + \sin \omega \cos \kappa)(y) - \cos \omega \cos \phi(f) \end{bmatrix} \\ &= \begin{bmatrix} -\cos \phi \sin \kappa(x) - \cos \phi \cos \kappa(y) \\ (-\sin \omega \sin \phi \sin \kappa + \cos \omega \cos \kappa)(x) + (-\sin \omega \sin \phi \cos \kappa - \cos \omega \sin \kappa)(y) \\ (\cos \omega \sin \phi \sin \kappa + \sin \omega \cos \kappa)(x) + (\cos \omega \sin \phi \cos \kappa - \sin \omega \sin \kappa)(y) \end{bmatrix} = \begin{bmatrix} m_{21}(x) - m_{11}(y) \\ m_{22}(x) - m_{12}(y) \\ m_{23}(x) - m_{13}(y) \end{bmatrix} = \begin{bmatrix} o_1 \\ p_1 \\ q_1 \end{bmatrix} \end{aligned} \quad (\text{C-26})$$

$$h_{14} = \frac{\partial F}{\partial X_{L1}} = \left| \begin{array}{ccc} \frac{\partial b_x}{\partial X_{L1}} & \frac{\partial b_y}{\partial X_{L1}} & \frac{\partial b_z}{\partial X_{L1}} \\ u_1 & v_1 & w_1 \\ u_2 & v_2 & w_2 \end{array} \right| + 0 + 0 = \left| \begin{array}{ccc} -1 & 0 & 0 \\ u_1 & v_1 & w_1 \\ u_2 & v_2 & w_2 \end{array} \right|_0 \quad (\text{C-27})$$

$$h_{15} = \frac{\partial F}{\partial Y_{L1}} = \left| \begin{array}{ccc} \frac{\partial b_x}{\partial Y_{L1}} & \frac{\partial b_y}{\partial Y_{L1}} & \frac{\partial b_z}{\partial Y_{L1}} \\ u_1 & v_1 & w_1 \\ u_2 & v_2 & w_2 \end{array} \right| + 0 + 0 = \left| \begin{array}{ccc} 0 & -1 & 0 \\ u_1 & v_1 & w_1 \\ u_2 & v_2 & w_2 \end{array} \right|_0 \quad (\text{C-28})$$

$$h_{16} = \frac{\partial F}{\partial Z_{L1}} = \left| \begin{array}{ccc} \frac{\partial b_x}{\partial Z_{L1}} & \frac{\partial b_y}{\partial Z_{L1}} & \frac{\partial b_z}{\partial Z_{L1}} \\ u_1 & v_1 & w_1 \\ u_2 & v_2 & w_2 \end{array} \right| + 0 + 0 = \left| \begin{array}{ccc} 0 & 0 & -1 \\ u_1 & v_1 & w_1 \\ u_2 & v_2 & w_2 \end{array} \right|_0 \quad (\text{C-29})$$

Components h_{17} , h_{18} , and h_{19} are derived for the second image in the same manner as h_{11} , h_{12} , and h_{13} respectively were derived for the first image.

$$h_{110} = \frac{\partial F}{\partial X_{L2}} = \left| \begin{array}{ccc} \frac{\partial b_x}{\partial X_{L2}} & \frac{\partial b_y}{\partial X_{L2}} & \frac{\partial b_z}{\partial X_{L2}} \\ u_1 & v_1 & w_1 \\ u_2 & v_2 & w_2 \end{array} \right| + 0 + 0 = \left| \begin{array}{ccc} 1 & 0 & 0 \\ u_1 & v_1 & w_1 \\ u_2 & v_2 & w_2 \end{array} \right|_0 \quad (\text{C-30})$$

$$h_{111} = \frac{\partial F}{\partial Y_{L2}} = \begin{vmatrix} \frac{\partial b_x}{\partial Y_{L2}} & \frac{\partial b_y}{\partial Y_{L2}} & \frac{\partial b_z}{\partial Y_{L2}} \\ u_1 & v_1 & w_1 \\ u_2 & v_2 & w_2 \end{vmatrix} + 0 + 0 = \begin{vmatrix} 0 & 1 & 0 \\ u_1 & v_1 & w_1 \\ u_2 & v_2 & w_2 \end{vmatrix}^0 \quad (\text{C-31})$$

$$h_{112} = \frac{\partial F}{\partial Z_{L2}} = \begin{vmatrix} \frac{\partial b_x}{\partial Z_{L2}} & \frac{\partial b_y}{\partial Z_{L2}} & \frac{\partial b_z}{\partial Z_{L2}} \\ u_1 & v_1 & w_1 \\ u_2 & v_2 & w_2 \end{vmatrix} + 0 + 0 = \begin{vmatrix} 0 & 0 & 1 \\ u_1 & v_1 & w_1 \\ u_2 & v_2 & w_2 \end{vmatrix}^0 \quad (\text{C-32})$$

This comprehensive exploration of the coplanarity condition was done to emphasize the implementation of this atypical observation model. Having created the Jacobian matrices, one must revisit the Kalman filter algorithm to discuss the incorporation of this measurement data into the linear filter.

LIST OF REFERENCES

- Alho, P., A. Kukko, H. Hyyppä, H. Kaartinen, J. Hyyppä, and A. Jaakkola. 2009. Application of boat-based laser scanning for river survey. *Earth Surface Processes and Landforms*. 34(13): 1831-1838.
- Alshawa, M., E. Smigiel, P. Grussenmeyer, and T. Landes. 2007. Integration of a Terrestrial LiDAR on a Mobile Mapping Platform: first experiences. In *5th International Symposium on Mobile Mapping Technology MMT*. Padua, Italy.
- Barber, D., J. Mills, and S. Smith-Voysey. 2008. Geometric validation of a ground-based mobile laser scanning system. *ISPRS Journal of Photogrammetry and Remote Sensing*. 63(1): 128–141.
- Bayoud, F.A. 2006. *Development of a robotic mobile mapping system by vision-aided inertial navigation: a geomatics approach*. PhD Thesis. Lausanne, Switzerland: École polytechnique fédérale de Lausanne. Available at: http://biblion.epfl.ch/EPFL/theses/2005/3440/EPFL_TH3440.pdf.
- Benjamin, A., A. Mohamed, and B. Wilkinson. 2010. Sequential Bundle Adjustment Using Kalman Filtering and Optimal Smoothing. *Surveying and Land Information Science*. 70(3): 161-169.
- Deckert, C. and P.V. Bolstad. 1996. Forest canopy, terrain, and distance effects on global positioning system point accuracy. *Photogrammetric Engineering and Remote Sensing*. 62(3): 317–321.
- Di, K.C., F.L. Xu, J. Wang, S. Agarwal, E. Brodyagina, R.X. Li, and L. Matthies. 2008. Photogrammetric processing of rover imagery of the 2003 Mars Exploration Rover mission. *ISPRS Journal of Photogrammetry and Remote Sensing*. 63(2): 181-201.
- DiGruttolo, N. 2010. *Marrying topography and tides; a high resolution tidal datum and intertidal zone elevation model for improved determination of short term sea level rise impacts in Florida bays*. Thesis (M.S.). Gainesville, FL: University of Florida. Available at: http://etd.fcla.edu/UF/UFE0042603/digruttolo_n.pdf.
- Edmundson, K.L. and C.S. Fraser. 1998. A practical evaluation of sequential estimation for vision metrology. *ISPRS Journal of Photogrammetry and Remote Sensing*. 53(5): 272-285.
- Ellum, C.M. and N. El-Sheimy. 2002. The Calibration of Image-Based Mobile Mapping Systems. In *Proceedings of the 2nd Symposium on Geodesy for Geotechnical and Structural Engineering*. Berlin, Germany: The International Association of Geodesy (IAG).
- Frazer, G.W., R. A. Fournier, J. A. Trofymow, and R. J. Hall. 2001. A comparison of digital and film fisheye photography for analysis of forest canopy structure and gap light transmission. *Agricultural and Forest Meteorology*. 109(4): 249–263.

- Gandaseca, S., T. Yoshimura, and H. Hasegawa. 2001. Evaluating the Positioning Performance of GPS Surveying Under Different Forest Conditions in Japan. In *Proceedings of the First International Precision Forestry Cooperative Symposium*. Precision Forestry. Seattle, WA: Institute of Forest Resources - University of Washington.
- Gelb, A. 1974. *Applied Optimal Estimation*. Cambridge, MA: MIT Press.
- Gillet, J., B. Scherzinger, and E. Lithopoulos. 2001. Tightly Coupled Inertial/GPS System for Precision Forestry Surveys Under Canopy: Test Results. In *Proceedings of the First International Precision Forestry Cooperative Symposium*. Precision Forestry. Seattle, WA: Institute of Forest Resources - University of Washington.
- Glennie, C. 2009. Kinematic Terrestrial Light-Detection and Ranging System for Scanning. *Transportation Research Record*. (2105): 135-141.
- Gräfe, G. 2007. Quality management in kinematic laser scanning applications. *International Archives of Photogrammetry and Remote Sensing*. XXXVI (5/C55). Available at: http://www.cirgeo.unipd.it/cirgeo/convegni/mmt2007/proceedings/papers/graefe_gunnar.pdf.
- Haala, N., M. Peter, J. Kremer, and G. Hunter. 2008. Mobile LiDAR mapping for 3D point cloud collection in urban areas: a performance test. *International Archives of Photogrammetry and Remote Sensing*. 37(B5): 1119-1124.
- Haala, N., D. Stallmann, and M. Cramer, 1998. Calibration of Directly Measured Position and Attitude by Aerotriangulation of Three Line Airborne Imagery. *International Archives of Photogrammetry and Remote Sensing*. 32(Part 3/1): 23-30.
- Hassan, T., C. Ellum, and N. El-Sheimy. 2006. Bridging Land-based Mobile Mapping Using Photogrammetric Adjustments. In *Proceedings of the ISPRS Commission I Symposium*. From Sensors to Imagery. Marne-la-Vallee, France: ISPRS: 128-139. Available at: <http://www.isprs.org/proceedings/XXXVI/part1/Papers/T10-44.pdf>.
- Holden, N. M., AA Martin, P. M. O. Owende, and S. M. Ward. 2001. A method for relating GPS performance to forest canopy. *International Journal of Forest Engineering*. 12(2): 51–56.
- Hu, L., Z. Gong, J. Li, and J. Zhu. 2009. Estimation of canopy gap size and gap shape using a hemispherical photograph. *Trees*. 23(5): 1101-1108.
- Inertial Explorer™. 2008. *Inertial Explorer™ Help Manual*. Waypoint® Products Group - Novatel®.

- Jennings, S., N. Brown, and D. Sheil. 1999. Assessing forest canopies and understory illumination: canopy closure, canopy cover and other measures. *Forestry*. 72(1): 59 -74.
- Kalman, R.E. 1960. A New Approach to Linear Filtering and Prediction Problems. *Transactions of the ASME - Journal of Basic Engineering*. 82D: 35-45.
- Kennedy, S., J. Hamilton, and H. Martell. 2006. Architecture and system performance of SPAN™–Novatel®'s GPS/INS solution. In *Proceedings of IEEE/ION PLANS 2006*. San Diego, CA. Available at: http://webone.novatel.ca/assets/Documents/Papers/SPAN_PLANS2006.pdf.
- Kersten, T.P. and E.P. Baltsavias. 1994. Sequential Estimation of Sensor Orientation for Stereo Images Sequences. *International Archives of Photogrammetry and Remote Sensing*. 30(5): 206-213.
- Kukko, A., C. O Andrei, V. M Salminen, H. Kaartinen, Y Chen, P. Rönholm, H Hyyppä, J Hyyppä, R. Chen, and H. Haggrén, others. 2007. Road Environment Mapping System of the Finnish Geodetic Institute–FGI Roamer. In *Laser Scanning 2007 and SilviLaser 2007*. 3/W52. ISPRS Workshop 2007. Espoo, Finland: ISPRS, 241–247. Available at: http://www.isprs.org/proceedings/XXXVI/3-W52/final_papers/Kukko_2007b.pdf.
- Li, R.X. 1997. Mobile mapping: An emerging technology for spatial data acquisition. *Photogrammetric Engineering and Remote Sensing*. 63(9): 1085-1092.
- Lowe, D.G. 1999. Object recognition from local scale-invariant features. In *Seventh IEEE International Conference on Computer Vision*. Corfu, Greece, 1150-1157.
- Mikhail, E.M., J.S. Bethel, and J.C. McGlone. 2001. *Introduction to modern photogrammetry*. New York: Wiley. Available at: <http://www.loc.gov/catdir/toc/wiley021/2001281274.html>.
- Mohamed, A.H. 2010. SUR 6535 GPS/INS Integration – Course Notes. University of Florida: Gainesville, Florida.
- Mohamed, A. 2007. Scanning the Waters: How LiDAR is helping to survey the nation's shoreline. *Point of Beginning*. (November).
- Morales, Y., T. Tsubouchi, and S. Yuta. 2010. Vehicle Localization in Outdoor Mountainous Forested Paths and Extension of Two-Dimensional Road Centerline Maps to Three-Dimensional Maps. *Advanced Robotics*. 24(4): 489–513.
- Muller, R.N. and D.S. Maehr. 2000. Are Universities Leaders in the Stewardship of Conservation Lands? *BioScience*. 50(8): 707–712.

- Nassar, S., X. J. Niu, and N. El-Sheimy. 2007. Land-vehicle INS/GPS accurate positioning during GPS signal blockage periods. *Journal of Surveying Engineering-ASCE*. 133(3): 134-143.
- Nobis, M. and U. Hunziker. 2005. Automatic thresholding for hemispherical canopy-photographs based on edge detection. *Agricultural and Forest Meteorology*. 128(3-4): 243–250.
- NovAtel Inc. 2006. GNSS/INS and DMI Processing of SPAN™ data with Inertial Explorer™ 7.61. Available at: http://webone.novatel.ca/assets/Documents/Waypoint/Reports/IE_DMI_ResultsV2.pdf.
- Otsu, N. 1979. A threshold selection method from gray-level histograms. *IEEE Transactions on Systems, Man, and Cybernetics*. 9(1): 62-66.
- Perry, J. 2009. *A synthesized directly georeferenced remote sensing technique for small unmanned aerial vehicles*. M.S. Gainesville, FL: University of Florida. Available at: http://etd.fcla.edu/UF/UFE0025070/perry_j.pdf.
- Petrie, G. 2010. An Introduction to the Technology Mobile Mapping Systems. *GEOInformatics*. 32-43.
- Piedallu, C. and J. Gégout. 2005. Effects of forest environment and survey protocol on GPS accuracy. *Photogrammetric Engineering and Remote Sensing*. 71(9): 1071-1078.
- Powell, T. L, G. Starr, K. L Clark, TA Martin, and H. L Gholz. 2005. Ecosystem and understory water and energy exchange for a mature, naturally regenerated pine flatwoods forest in north Florida. *Canadian Journal of Forest Research*. 35(7): 1568–1580.
- Rauch, H. E., F. Tung, and C. T. Striebel. 1965. Maximum likelihood estimates of dynamic systems. *AIAA Journal*. 3(8): 1445-1450.
- Reutebuch, S. E, W. W. Carson, and K. M. Ahmed. 2003. A Test of the Applanix™ POS™ LS Inertial Positioning System for the Collection of Terrestrial Coordinates Under a Heavy Forest Canopy. In *Proceedings of the Second International Precision Forestry Symposium*. Seattle, WA, 21-27. Available at: http://www.cfr.washington.edu/research.pfc/publications/Reutebuch_Applanix_per6_9_03.pdf.
- Rossmann, I. J, D.I.P. Krahwinkler, and D.I.C. Schlette. 2009. Navigation of Mobile Robots in Natural Environments: Using Sensor Fusion in Forestry. In *7th International Conference on Computing, Communications and Control Technologies (CCCT), July 10th-13th*. Orlando, Florida.

- Samadzadegan, F., M. Hahn, and S. Saeedi. 2007. Position Estimation of Aerial Vehicle Based on a Vision Aided Navigation System. In *Visualization and Exploration of Geospatial Data*. 4/W45. 2007 ISPRS Joint Workshop. Stuttgart, Germany: ISPRS. Available at: http://www.geovisualisierung.net/isprs2007/docs/41_Samadzadegan.pdf.
- Schneider, D., E. Schwalbe, and H. G Maas. 2009. Validation of geometric models for fisheye lenses. *ISPRS Journal of Photogrammetry and Remote Sensing*. 64 (3): 259–266.
- Schwarz, K. P, and N. El-Sheimy. 2004. Mobile Mapping Systems – State of the Art and Future Trends. *International Archives of Photogrammetry, Remote Sensing and Spatial Information Sciences*. 35(B5): 759-768.
- Schwarz, K.P. & Wei, M., 2000. INS/GPS Integration for Geodetic Applications – Lecture Notes. Dept of Geomatics Engineering: University of Calgary.
- Sigrist, P., M. Coppin, and P. Hermy. 1999. Impact of forest canopy on quality and accuracy of GPS measurements. *International Journal of Remote Sensing*. 20(18): 3595-3610.
- Škaloud, J. 1999. *Optimizing georeferencing of airborne survey systems by INS/DGPS*. PhD Thesis. Calgary, Alberta, CAN: University of Calgary. Available at: http://www.ucalgary.ca/engo_webdocs/KPS/99.20126.JSkaloud.pdf.
- Smith, W. Brad, P. Miles, J. S. Vissage, and S. A. Pugh. Forest Resources of the United States, 2002. Available at: <http://www.ncrs.fs.fed.us/>.
- Talaya, J., R. Alamus, E. Bosch, A. Serra, W. Kornus, and A. Baron. 2004. Integration of a terrestrial laser scanner with GPS/IMU orientation sensors. In *Proceedings of the Congress of the International Society for Photogrammetry and Remote Sensing (ISPRS)*. XX ISPRS Congress, Commission 5. Istanbul, Turkey.
- Tao, C.V. 2000. Semi-Automated Object Measurement Using Multiple-Image Matching from Mobile Mapping Image Sequences. *Photogrammetric Engineering and Remote Sensing*. 66(12): 1477–1485.
- Taylor, C.N. 2009. Enabling Navigation of MAVs through Inertial, Vision, and Air Pressure Sensor Fusion. *Multisensor Fusion and Integration for Intelligent Systems*. 143–158.
- Tommaselli, A.M.G. and C.L. Tozzi. 1996. A recursive approach to space resection using straight lines. *Photogrammetric Engineering and Remote Sensing*. 62(1): 57-66.
- Wackrow, R., J.H. Chandler, and P. Bryan. 2007. Geometric consistency and stability of consumer-grade digital cameras for accurate spatial measurement. *The Photogrammetric Record*. 22(118): 121–134.

- Wang, X. and T.A. Clarke. 2001. Separate adjustment in close-range photogrammetry. *ISPRS Journal of Photogrammetry and Remote Sensing*. 55(5-6): 289-298.
- Webb, T.P. 2007. *Vision-based state estimation for uninhabited aerial vehicles using the coplanarity constraint*. PhD Dissertation. Gainesville, FL: University of Florida. Available at: <http://purl.fcla.edu/fcla/etd/UFE0019262>.
- Welch, G. and G. Bishop. 2001. An Introduction to the Kalman Filter. In *SIGGRAPH 2001*. Chapel Hill, NC: University of North Carolina at Chapel Hill, 45. Available at: http://www.cs.unc.edu/~tracker/media/pdf/SIGGRAPH2001_CoursePack_08.pdf.
- Wilkinson, B.E., B.A. Dewitt, A.C. Watts, A.H. Mohamed, and M.A. Burgess. 2009. A New Approach for Pass-point Generation from Aerial Video Imagery. *Photogrammetric Engineering and Remote Sensing*. 75(12): 1415–1423.
- Wolf, P.R. and B.A. Dewitt. 2000. *Elements of Photogrammetry: with Applications in GIS*. Boston: McGraw-Hill.
- Wright, W.C. 2008. *Quantifying global position system signal attenuation as a function of three-dimensional forest canopy structure*. Thesis (M.S.). Gainesville, FL: University of Florida. Available at: http://etd.fcla.edu/UF/UFE0021906/wright_w.pdf.
- Xiaopeng, W., K. Gaofeng, and H. Xiaobin. 2008. Forest fire fighting command and decision making system study based on 3s technology - take Jiaohe city in Jilin province as an example. In *Spatial Data Integration for Emergency Services*. ISPRS Congress Beijing 2008. Beijing, China: ISPRS, 1113-1116. Available at: http://www.isprs.org/proceedings/XXXVII/congress/4_pdf/194.pdf.
- Xiong, K., L. D. Liu, and H. Y. Zhang. 2009. Modified unscented Kalman filtering and its application in autonomous satellite navigation. *Aerospace Science and Technology*. 13(4-5): 238-246.
- Zengin, H. and A. Yesil. 2006. Comparing the performances of real-time kinematic GPS and a handheld GPS receiver under forest cover. *Turkish Journal of Agriculture and Forestry*. 30: 101–110.
- Zheng, J., Y. Wang, and N.L. Nihan. 2005. Quantitative evaluation of GPS performance under forest canopies. In *Networking, Sensing and Control, 2005. Proceedings. 2005 IEEE*. 777–782.

BIOGRAPHICAL SKETCH

Adam R. Benjamin was born in South Kingstown, Rhode Island to his parents, Robert and Muriel Benjamin, in April 1982. Adam has a young son, Kai Benjamin, with his wife, Erica Sweitzer. He has one younger brother, Zachary Benjamin.

Adam was raised in the small coastal town of Narragansett, RI. While growing up, he was active in many outdoor activities including basketball, golf, soccer, baseball, hiking, camping, and the beach. He attended The Prout School in Wakefield, RI where he obtained an International Baccalaureate Diploma in 2000. Upon graduation, he enrolled in Elon College (now Elon University) as an Honors Fellow. Adam graduated cum laude in May 2004 with a BS degree in Mathematics and extensive studies in Economics.

Adam successfully pursued real estate licensure in Rhode Island and Florida. He worked in the real estate and mortgage industry until 2006. Adam then switched careers by working at a small surveying and engineering firm in Charlestown, RI. He enjoyed the mix of applied mathematics and science in an outdoor environment. In August 2008, he successfully completed the Professional Land Surveying Certificate Program at Wentworth Institute of Technology in Boston, MA.

Desiring more advanced education in surveying and mapping, Adam enrolled as a graduate assistant in the geomatics department in the School of Forestry and Resource Conservation at the University of Florida in August 2009. He received his master's degree from the University of Florida in the summer of 2011.

Adam's academic interests include photogrammetry, LiDAR, mobile mapping systems, hydrographic surveying, and coastal mapping. He is currently employed by the University of Florida as a Geomatics Specialist and Program Assistant in the Fort

Lauderdale Research and Education Center. In this position, Adam teaches geomatics courses, advises students, collaborates on geomatics research projects, and continues his educational pursuit of a doctoral degree in geomatics.